Experimental Investigation of the Shock-Induced Distortion of a Spherical Gas Inhomogeneity

Devesh Ranjan

December 2007

UWFDM-1337

Ph.D. thesis.

FUSION TECHNOLOGY INSTITUTE

UNIVERSITY OF WISCONSIN

MADISON WISCONSIN

Experimental Investigation of the Shock-Induced Distortion of a Spherical Gas Inhomogeneity

Devesh Ranjan

Fusion Technology Institute
University of Wisconsin
1500 Engineering Drive
Madison, WI 53706

http://fti.neep.wisc.edu

December 2007

UWFDM-1337

Ph.D. thesis.

Experimental Investigation of the Shock-Induced Distortion of a Spherical Gas Inhomogeneity

By

Devesh Ranjan

A dissertation submitted in partial fulfillment of the requirements for the degree of

Doctor of Philosophy

(Mechanical Engineering)

at the

UNIVERSITY OF WISCONSIN – MADISON

2007

Abstract

In a high load capability vertical shock tube, a series of experiments have been carried out to characterize the interaction of a planar shock wave with discrete gas inhomogeneities. Eleven scenarios have been considered covering the Atwood ($A = (\rho_2 - \rho_1)/(\rho_2 + \rho_1)$) and Mach ($M$) number ranges $-0.8 < A < 0.7$ and $1.3 < M < 3.5$, where the test gas volume is contained inside a large spherical soap bubble. The shock wave strength, leading to a post-shock compressible regime, allows the study of instability development in an intermediary regime between low Mach number shock tube experiments and high Mach number laser-driven experiments that has not been investigated previously. Flow visualizations are obtained using planar laser diagnostics. The imaging technique used here takes advantage of the atomization of the liquid bubble film by the incident shock wave, and up to five shocked bubble images are captured per run, enhancing the investigation of the evolution of the instability during a single experiment. Quantitative analysis of the experimental data include the vortex velocity, and subsequent circulation calculations, along with a new set of relevant geometrical length scales. As the planar shock passes over the bubble, intense vortical and nonlinear acoustic phenomena are observed, including vortex ring formation, mixing, and growth of turbulence-like features. At late-times, experimental images show the presence of secondary features in the flow field at high Mach numbers, some of which were predicted previously but, until now, not confirmed experimentally. In the case of a low Atwood number, the late time flow field is dominated by coherent vortical structures while, in the case of a high Atwood number, the shocked bubble is effectively reduced to a small core of compressed fluid, which trails behind a plume-like structure indicative of a well-developed mixing region. Dimensionless analysis of trends in the bubble length scales and other features shows that no universal timescale exists, but for each feature, a unique velocity scale is appropriate as a basis for timescaling arguments.

Acknowledgements

First and foremost, I would like to thank my advisor, Professor Riccardo Bonazza, for his continuous support, invaluable guidance, and great supervision throughout the course of my PhD work. I am truly grateful to him for making time for discussions with me in his extremely busy schedule, and teaching me the fundamentals of the hydrodynamic instabilities. He is a fantastic teacher who exhibits lots of patience and understanding in his interactions with students. I have learned invaluable lessons from his insight not only in my professional work but also in my personal life.

I have been part of a wonderful research group. I would like to thank Dr. Mark Anderson for his continual encouragement and many helpful discussions with me. His suggestions, encouragement, advice, and cooperation were of immense help to me. The completion of this thesis is vastly due to his guidance and help during several critical junctures. I would also like to express my gratitude to Dr. Jason Oakley, who patiently read this dissertation in great detail and suggested many changes that dramatically improved this document. He was always glad to answer my many questions on data analysis, and on some occasions, his hints saved me from a dead end. I consider myself lucky to have had them as my mentors. A special mention of thanks for Mr. Paul Brooks for the countless times I received help from him and his crew on technical difficulties over the years. I must give special thanks to Dr. Jeff Greenough for his generous advice and help throughout the course of this work.

I also benefited immensely from close interaction and collaboration with Dr. John Niederhaus. The *Raptor* simulations which appear in this study were performed entirely by Dr. Niederhaus. I am thankful to him for thoughtful discussions, and his input during the writing of various research reports and publication drafts. His suggestions and comments were always useful and never failed to improve this work. I would also like to thank Brad Motl for his unconditional support in performing these experiments. He is as much part of this project as I am. It has been a great pleasure to work with him. Thanks also go to each of my dissertation committee members for their useful comments, suggestions and help, to Professor Rolf Reitz for numerous conversations regarding film breakup, to Professor Jaal Ghandhi for conversations regarding flow visualization, to Jeremy White for help with Matlab programming, to Nicholas Haehn for proof reading the several drafts of this dissertation, to Brad Motl for insights on LabView programming, to Achuth Munnannur for drop breakup references, and to Guillaume Mignot for all the translation work.

I have enjoyed living in Madison for the last four years. I would like to thank Sam Bhaiya, Sujata Bhabhi, Achuth, Adiga, Amanda, April, Ranjith, Siva, Neerav, Navtej, Magesh, Sundar, Jay, Jeremy, Nick, and Chris for having put up with my antics and providing me with much needed breaks. I would also like to thank the members of the "Friday Ping-Pong" group, and hope Professor Bonazza keeps this group alive in the future.

Finally, I would like to thank my family for their immense support and affection. I'm greatly indebted to them and cannot in any measure repay all that they have done for me. I dedicate this thesis work to my parents.

This work was supported by the U.S. Department of Energy Grant No. DE-FG52-06NA26196.

Contents

List of Figures

List of Tables

Notation and Symbols

Abbreviations

SBI	Shock-bubble Interaction
SAIF	Shock Accelerated Inhomogeneous Flows
ISM	Interstellar Medium
WiSTL	Wisconsin Shock Tube Laboratory
FAV	Fast-acting Valve
RMI	Richtmyer-Meshkov Instability
ICF	Inertial Confinement Fusion
DT	Deuterium-Tritium
PVR	Primary Vortex Ring
SVR	Secondary Vortex Ring
TVR	Tertiary Vortex Ring
SJ	Secondary Jet
FSF	Fast-Slow-Fast
SFS	Slow-Fast-Slow

Latin symbols

A	Pre-shock Atwood number across the interface
A'	Post-shock Atwood number across the interface
c_1'	Sound speed in the shocked ambient gas, in lab frame
c_1	Sound speed in the ambient gas, in lab frame
D	Initial bubble diameter
D_v	Major diameter of the vortex ring
d_v	Minor diameter of the vortex ring
I	Impulse per unit volume transmitted by the shock to the gas bubble
M	Mach number of incident shock wave
t	Time after initial shock impact
$\mathbf{u}$	Velocity vector
u_1'	Flow speed of shocked ambient gas, in lab frame
V_b	Translational velocity of shocked bubble
V_v	Translational velocity of the vortex ring
W_i	Propagation speed of incident shock wave
W_t	Propagation speed of shock wave transmitted into bubble

$\delta\mathcal{R}$	Acoustic impedance mismatch
Re	Reynolds number
p	Atwood number exponent in timescaling
Re_ν	Physical Reynolds number based on circulation and viscosity
t'	Characteristic time, $\tau = D/2W_t$

Greek symbols

α	Rate of axial elongation
γ	Ratio of specific heats
Γ	Velocity circulation
Γ^+	Positive circulation in the vortex ring
Γ^-	Negative circulation in the vortex ring
Γ_0	Net circulation in the flow field
η_0	Initial perturbation amplitude
ρ_1	Initial density of unshocked ambient gas
ρ_2	Initial density of unshocked bubble gas
ρ_1'	Density of shocked ambient gas

σ	Ratio of shocked bubble gas relative to ambient gas
τ	Non-dimensional time scale
$\boldsymbol{\omega}$	Vorticity vector
χ	Initial density ratio of bubble gas relative to ambient gas

Subscripts

1	Ambient fluid
2	Bubble fluid
i	Incident shock wave
r	Reflected shock wave
t	Transmitted shock wave

Diacritical marks

$'$	Singly shocked fluid
$''$	Twice shocked fluid
$'''$	Three-times shocked fluid

Chapter 1

Introduction

1.1 Shock-Bubble Interaction

The evolving flow field generated by the interaction of a shock wave with a density inhomogeneity involves the strong coupling of several types of fluid dynamic phenomena, including, shock wave refraction and reflection, vorticity production and transport, and turbulence. This interaction results in a complex pattern of shock waves (focusing and scattering), while simultaneously resulting in the formation of characteristic vortices, and often, enhancing the mixing of the ambient gas with the gas inhomogeneity. This is a problem of fundamental interest, which can be used as a "building block" to develop understanding of more complicated problems involving shock propagation through random media characterized by inhomogeneities in density, temperature, or other thermodynamic variables. The shock-bubble interaction (SBI) is a fundamental configuration for studying shock accelerated inhomogeneous flows (SAIF), *i.e.*, an extension of the Richtmyer-Meshkov instability (RMI). Here, the problem of shock-accelerated inhomogeneous flows is considered in a particularly simple configuration: the interaction of a planar shock wave with a single spherical gas bubble in an otherwise uniform gas medium.

The phenomenon of SBI takes place in a wide variety of energy- and spatially- scaled applications. It can be applied to study the fragmentation of gallstones or kidney stones by shock waves [14, 16, 19] as well as to study the interaction of supernova remnants with interstellar clouds [25, 32]. It also finds application in atmospheric sonic boom propagation [12], "high-energy-density" systems such as inertial confinement fusion devices [39], supersonic combustion [40, 72], and shock mitigation in foams and bubbly liquids [4, 9, 13]. Further, in the interaction of a shock wave with a single bubble, analogies may be drawn to the well-known development of Richtmyer-Meshkov instabilities of perturbations on impulsively accelerated fluid interfaces.

1.1.1 Astrophysical systems

The dynamics of interstellar medium (ISM) in spiral galaxies is significantly affected by the strong shock waves generated by supernovae explosion, stellar winds, expanding HII regions, and spiral density waves [32]. It is universally accepted that the generated shock waves significantly alter the morphology of the cloud (a region of higher density) and lead to turbulent exchange of material and energy between interstellar gases of different temperatures and densities. The bright eastern knot of the Puppis A supernova remnant is responsible for distorting a shock front due to a cloud-shock interaction as seen in images from the Chandra X-ray telescope [25]. The issues of mass stripping from the cloud, transfer of energy and momenta to the shocked cloud, and instabilities created by shocks at the cloud boundary can be analyzed with laser laboratory experimental results from SBI studies [32, 22].

1.1.2 Inertial confinement fusion

The emergence of inertial confinement fusion (ICF) as a potential power source in the late 1960's provided a significant impetus for investigating shock-accelerated inhomogeneous flows. In ICF, a tiny amount of fusion fuel [39] is compressed to a high density and heated to a very high temperature, in order to initiate a very rapid and efficient thermonuclear burn. In laser- heavy-ion- or Z-pinch-driven ICF targets, compression is accompanied by fluid instability growth and understanding this instability is fundamental for achieving ignition and yield from the target. The surface of the deuterium-tritium (DT) target becomes unstable due to Rayleigh-Taylor and Richtmyer-Meshkov growth where vorticity is generated baroclinically at the interface, resulting in interface deformation and allowing the materials to mix after the shock wave has passed. The turbulent mixing between the DT fuel and the ablator surface, along with the asymmetry associated with the compression, can severely degrade the fusion yield.

1.1.3 Supersonic combustion

The Richtmyer-Meshkov instability plays a positive role in the field of supersonic combustion. In the case of a scramjet engine, the RMI-induced turbulent mixing improves the combustion process by enhancing the mixing of the air and the fuel in the short burn time available [40, 72]. In his classic experiment, Markstein [42] showed how combustion wave enhancement followed the acceleration of an initially curved flame surface by a shock wave. Curved flame fronts, when accelerated by a shock wave, undergo heavy distortions such as shape reversal and spike formations, and the volumetric rate of burning is amplified after the shock interacts with the flame.

1.1.4 Shock mitigation

The physics associated with SAIF are also encountered in shock-mitigation and energy exchange mechanisms where bubbly liquids and aqueous foam barriers are used to redistribute the impulse of the shock waves [4, 9, 13]. The dissipation is attributed to interphase heat transfer and small-scale internal processes within the foam. Aqueous foams exhibit high acoustic impedance and low sound speed, so that shock waves/blast waves are subject to refraction and partial transmission at foam/air interfaces and are delayed within the foam [4]. Shock mitigation is of great concern in the case of protection mechanisms for ICF chamber walls.

1.2 Scope, Approach, and Organization

To elucidate the physics of shock-accelerated inhomogeneous flows, the present study is undertaken, where simplified experiments are being conducted in a high structural capacity vertical shock tube. The test gas is contained inside a large spherical soap bubble. Soap bubbles represent the simplest form of gas enclosure with their naturally spherical shape- ideal for a three-dimensional problem. The soap membrane is thin and tenuous which keeps the film nonuniformities to a minimum. In this configuration, the effects of surface tension, phase changes, ionization, chemical reactions, and interactions between multiple inhomogeneities are removed, and the mechanisms of shock-induced acceleration, vorticity production, and mixing can be studied independently. The post-shock evolution of the bubble is captured using planar laser diagnostics.

The objectives and anticipated outcomes of this thesis are fourfold. The first goal is to generate a large database of experimental results diagnosing the SBI, which will lead to several qualitative and quantitative parameters, that can be used to understand the underlying physics, and for code validation efforts. The SBI is an ideal problem for code validation as the flow field exhibits several types of fluid dynamic phenomena, including shock wave refraction and reflection, vorticity production and transport, and turbulence. Recently, the existing numerical database has been extended by the three-dimensional numerical study performed by John Niederhaus [47]. This provides the opportunity to utilize these three-dimensional simulation in concert with the experiments to understand the evolving vorticity dynamics and subsequent turbulent mixing.

The second goal is to develop scaling laws from the acquired experimental data. Several features observed in the shock-bubble interactions are correlated across the parameter space, in order to evaluate the different scaling laws. These features include the axial and lateral extents of the bubble, translational velocities of the bubble and associated vortex rings, volume, and the circulation which is deduced from the ring's velocity defect.

The third goal is to understand the evolution of the hydrodynamic instability in the post-shock compressible limit. It is believed that, at Mach numbers where the particle velocity behind the incident shock wave becomes supersonic, there are compressibility effects that may alter the rate of distortion of the inhomogeneity. The shock wave strength, leading to a post-shock compressible regime, allows the study of instability development in an intermediary regime between low Mach number shock tube experiments [21, 35, 36] and very high Mach number laser-driven experiments [31, 60] that has not been investigated previously. Qualitative and quantitative comparisons are made with the laser-driven very- high- Mach-number experiments.

Recently, the computational study conducted by Niederhaus *et al.* [48] showed particularly distinct effects from the SBI for air-R12 at $M = 2.5$ and 5.0. In those two scenarios, at high-M and high-A conditions, the SBI leads to the development of a region of intense mixing. The fourth goal of this study is to conduct experiments in the parameter space $M > 2.5$ and $A > 0.6$ in order to study the distortion of the bubble by the shock wave. This regime is important, as the computational studies have shown that shock focusing can drastically alter the flow field.

The scope of this dissertation is limited to the spherical-bubble scenario. It is anticipated that the completion of this project will lead to a better understanding of the flow field in a regime which has not been studied previously. The results may provide validation to various numerical claims made in the past. It will also provide a detailed analysis of the effect of the accumulation of soap film (excessive mass) near the bottom of the bubble on the flow field at late-time, which is important in the field of astrophysics where inhomogeneities are rarely uniform.

The organization of this dissertation is as follows. Chapter 2 discusses the physics of the shock-bubble interaction, and the previous related experimental, theoretical and numerical work appearing in the literature. Chapter 3 presents a detailed description of the Wisconsin Shock Tube, the experimental setup, the related instrumentation for data acquisition, and flow visualization technique. Chapter 4 presents a detailed qualitative description of the flow features observed in the experiments. Chapter 5 provides a detailed analysis of quantitative measurements obtained from the experimental data. Finally, conclusions and future work are presented in Chapter 6.

Chapter 2

Literature Review

The presence of non-linear acoustic effects (shock refraction, diffraction, and reflection) along with interface instability, including non-linear growth and transition to turbulence, combine to make the Richtmyer-Meshkov instability a most challenging problem in fluid dynamics. Several approaches to study RMI exist: astronomical observations (ISM), laboratory experiments, analytical theory, and numerical simulation. Over the last four decades a rich database of literature has been developed in the study of the RMI. The complexity of the problem strongly slows down the progress in the analytical approach, especially for the case of shock-bubble interaction. Although the focus of this work is on spherical geometry, it is imperative to begin by discussing the work related to planar geometry.

2.1 Richtmyer's Theory

Richtmyer [59] considered the problem of the instability of a two-dimensional, single wavelength, sinusoidal interface between two semi-infinite, compressible fluids, when accelerated by a shock wave passing from the light fluid to the heavy fluid as shown in Fig. 1. In developing his impulsive model, he assumed that, for weak shocks, the perturbation velocities are not comparable to the speed of sound. He proposed that, by the time the transmitted and reflected shock wave have traveled a long distance from the interface, comparable to the wavelength of the perturbation, the subsequent motion of the interface may be considered incompressible.

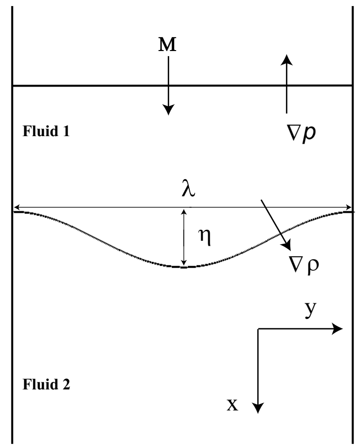

Figure 1: Basic configuration for the Richtmyer-Meshkov instability in rectangular geometry. Two fluids, 1 and 2, initially at rest and having different properties (such as density ρ and ratio of specific heat γ, for example), are separated by an interface that has an initial perturbation (wavelength λ and amplitude η); a normal shock wave, traveling from top to bottom from Fluid 1 into Fluid 2 is about to accelerate the interface [6].

In 1950, Taylor [66] studied the problem of the instability between two immiscible incompressible liquids of different densities under the gravitational acceleration g. According to the linear theory developed by Taylor, the differential equation governing the amplitude growth is

$$\frac{d^2\eta(t)}{dt^2} = kgA\eta(t), \tag{2.1}$$

where η is the amplitude of the small single-mode sinusoidal perturbation on a discontinuous interface between incompressible fluids; k is the wavenumber of the perturbation defined as $2\pi/\lambda$, λ being the wavelength of the perturbation; A is the Atwood number of the interface defined as $A \equiv (\rho_2 - \rho_1)/(\rho_2 + \rho_1)$. Assuming the subsequent motion at the interface is within the incompressible regime, Richtmyer modified Taylor's analysis to describe the evolution of the shock accelerated interface. In particular he replaced the constant acceleration term in Taylor's analysis with an impulsive one $g = [u]\delta_D(t)$, in Eq. 2.1, where $\delta_D(t)$ is the Dirac delta function and $[u]$ is the jump in the interface velocity induced by the refraction of the incident shock. Substituting the values of g in Eq. 2.1 yields

$$\frac{d^2\eta(t)}{dt^2} = k[u]\delta_D(t)A\eta(t). \tag{2.2}$$

Integrating Eq. 2.2 once with respect to time, Richtmyer obtained the impulsive growth rate relation

$$\frac{d\eta(t)}{dt} = k[u]A\eta_0, \tag{2.3}$$

where η_0 is the initial amplitude. Equation 2.3 is valid as long as the perturbation amplitude is small enough to remain in the linear regime ($\eta k << 1$).

Richtmyer also solved the linearized equation for the RMI problem numerically for the light/heavy configuration ($A > 0$) and strong incident shock waves. He found that the growth rate of the perturbations agreed with the impulsive model Eq. 2.3, within 5%-10%, if the post-shock values of the initial amplitude and Atwood number are used in the impulsive model instead of the pre-shock values. The corrected Richtmyer's impulsive model is thus given as

$$\frac{d\eta(t)}{dt} = k[u]A'\eta_0', \tag{2.4}$$

where η_0' and A' are the post-shock perturbation amplitude and Atwood number respectively. The impulsive model neglects viscosity and surface tension since its validity is restricted to early time behavior and gas-gas interfaces.

2.2 Single Mode Two Dimensional Interface

One of the greatest challenges in performing RMI experiments is the preparation of the initial interface. Meshkov [44] was the first experimentalist to study a shock-accelerated gas-gas interface, and the experiments were inspired by the theoretical work done by Richtmyer [59] in 1960. Meshkov used a thin nitrocellulose membrane to separate the test gases, a technique that has been commonly used in many subsequent experiments. The interface was given an initial sinusoidal shape and it was shown to be unstable regardless of whether the shock passed from a heavy gas to a light gas or from a light gas to a heavy gas. The amplitude of the disturbance increased linearly with time in the first approximation in agreement with Richtmyer's theory. However, there are several well-documented problems with using membranes: first, the strength of the membrane and the supporting wires used to impose the perturbation can weaken the transmitted shock wave; second, post-shock fragments of the film and wires affect the fluid flow; and third, the same fragments hinder diagnostic and imaging techniques.

Innovative preparation methods have been used to eliminate the membrane and create a continuous interface. Brouillette and Sturtevant [7] and Bonazza and Sturtevant [5] used a thin, flat, sliding plate in a vertical shock tube to separate two gases in a light-over-heavy configuration. The physics of plate retraction provided the initial perturbation between the vertically stratified gases. The initial conditions in this case are non-linear and multiple valued due to vortex shedding off of the plate. This technique generates a relatively thick, diffuse interface, which significantly reduces the growth rate. Oakley [49] and Puranik *et al.* [54] used a sinusoidally formed plate to separate the two gases (initially arranged in the gravitationally unstable configuration) and allow the Rayleigh-Taylor instability to create the initial perturbation. In a cross-sectional view perpendicular to the direction of plate retraction, the initial condition was quasi two-dimensional; however, due to disturbances in the direction of the plate retraction, the interface had three-dimensional characteristics.

Jacobs *et al.* [28] used a contoured jet or gas curtain entering from one wall of the test section and exiting from another side to create two continuous interfaces. In this method, the biggest challenge is to maintain the stability of the jet. It has been documented that upstreamdownstream asymmetry between perturbation amplitudes of the initial conditions could produce either upstream mushrooms or downstream mushrooms, depending on whether the initial upstream or downstream perturbations were greater, respectively. This interface creation technique is currently in extensive use at Los Alamos National Laboratory [53].

Another membrane-free scheme has been implemented by Jones and Jacobs [29] who used a downward flow of light gas and upward flow of heavy gas that meet at a desired interface location to create a relatively thin continuous flat interface. A stagnation plane at the interface location is created by this technique which reduces the diffusion thickness because of the gas-outflow slots in the side-walls of the shock tube. The vertical shock tube was then oscillated in the lateral direction to create the initial perturbation. At the University of Wisconsin-Madison, Motl *et al.* [45] have implemented the technique of membraneless interface formation by Jones and Jacobs [29] in the high capability vertical shock tube. An oscillating rectangular piston system (see Fig. 2) has been added to the shock tube to create the initial perturbation once the flat interface is formed. This new technique allowed them to study the growth of instability for higher Mach numbers.

There have been several review papers summarizing the state of the field. Zabusky [73]

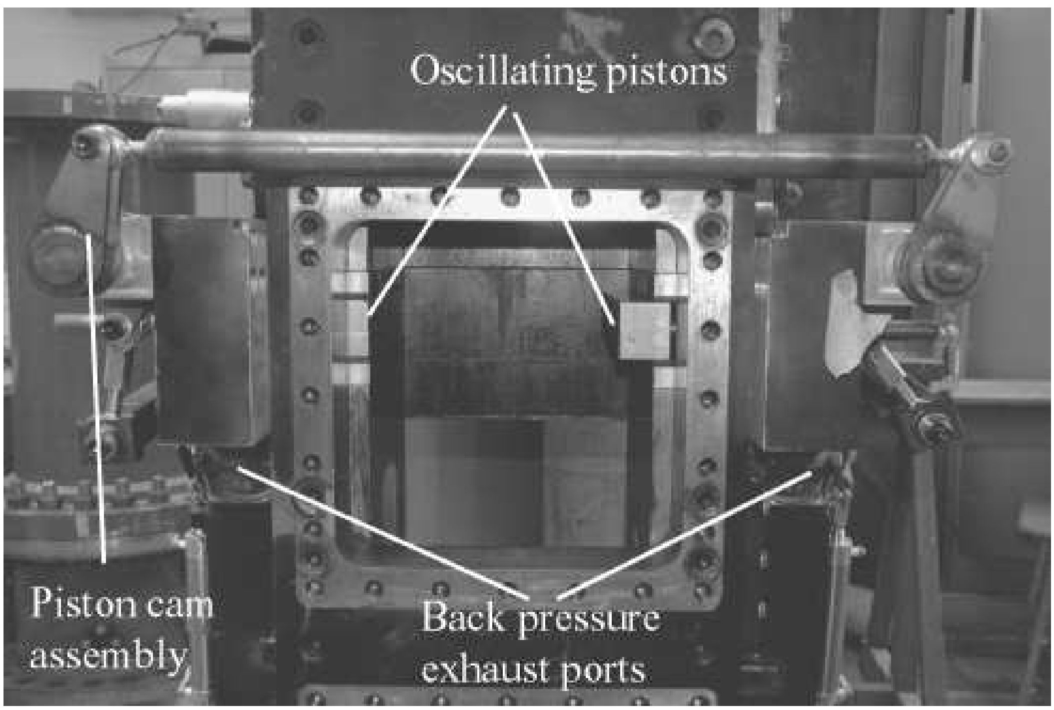

Figure 2: The University of Wisconsin oscillating piston setup.

in 1999, reviewed the vortex models and numerical simulation studying the RMI, in the classical configuration. Brouillette [6] in 2002, summarized the state of the field in his review paper which focussed on the basic physical processes underlying the onset and development of the RMI in a simple configuration.

2.3 Cylindrical and Spherical Interfaces

Experimental investigations of the interaction of shock waves with curved interfaces have been inspired by the pioneering works performed by Markstein [42, 41] and Rudinger [61], who studied the interaction of a shock wave with a flame front having a roughly spherical shape. The primary focus of the study was to quantify the effect of the shock on the volumetric rate of burning. The interaction of pressure waves with density gradients is a fundamental source of long-lived vorticity in fluids and is particularly important in combustion, since the release of the chemical energy produces both pressure and density disturbances in the fluid. These disturbances then interact, producing significant vorticity in the flow field.

In his classic experiment, Markstein [42] showed how combustion enhancement followed the acceleration of an initially curved flame surface by a shock wave. Curved flame fronts, when accelerated by a shock wave, undergo heavy distortions such as inflection and spike formation. The volumetric rate of burning is amplified after the shock interacts with the flame. Markstein also studied the interaction of a shock wave with an initially roughly spherical flame and Fig. 3 shows schlieren images from one of Markstein's experiments. A weak shock passes through a roughly spherical flame approximately 15-cm from the bottom of the combustion chamber, which contains a stoichiometric mixture of n-butane and air. In Fig. 3(a), the shock wave appears to be less than 1-cm from the flame boundary (the flame actually appears more oblong than spherical). In Fig. 3(b), one can clearly see the compression of the flame front and an upward moving curved rarefaction wave. The central spike of unburned gases traverses the lower portion of the flame front (see Fig. 3(c)) leading to the formation of a vortex ring. This enhanced flow, due to the vortex ring, leads to the formation of a very fine-grained turbulent burning zone.

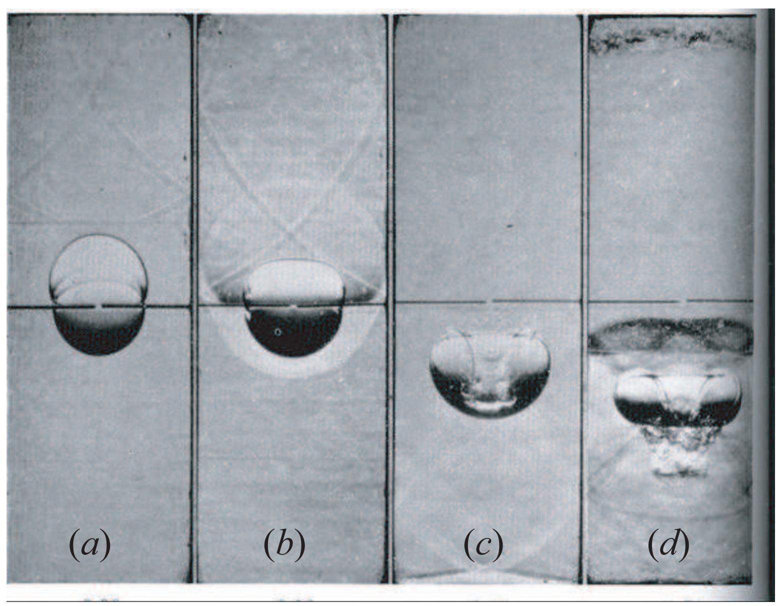

Figure 3: Interaction of a shock wave and a flame of initially roughly spherical shape. Pressure ratio of incident shock wave 1.3; stoichiometric butane-air mixture ignited at the center of the combustion chamber, 8.70 ms before origin of time scale [61]. Time relative to initial shock wave impact: (a) 0.00 ms; (b) 0.10 ms; (c) 0.40 ms; (d) 0.70 ms.

To analyze the fluid dynamic aspects of vorticity generation, the problem may be more fundamentally studied in a non-reactive medium. If the flame is not a continuous surface but contains discrete pockets of burned or unburned gas surrounded by gases of different density, such as may exist around evaporating fuel droplets, another mechanism to increase the volumetric burning rate may come into play. The response of such isolated regions of different density to impulsive acceleration was studied in 1960 by Rudinger and Somers [62] without the complications of the combustion process.

Rudinger and Somers [62] studied the more fundamental problem of the interaction of a plane shock wave with light-or heavy-gas spherical or cylindrical inhomogeneities, produced using either a spark discharge or small jets of H_2, He, or SF_6. They showed that, after acceleration by a shock wave, the small regions in a flow where the density was different than that of the surrounding gas, moved faster or slower than the latter, depending on whether their density was lower or higher than that of the main flow. The interaction of a shock wave with a cylindrical or spherical gas inhomogeneity has become more commonly known as the shock-bubble interaction. Inspired by the seminal work of Rudinger and Somers [62], the last two decades have provided a rich database of literature for the study of the shock-bubble interaction.

2.4 Physics of the Shock-Bubble Interaction

The propagation of a shock wave through a spherical or cylindrical bubble of a different density than the surrounding medium involves the phenomena of shock wave reflection, refraction, diffraction, and in the case of a heavy bubble, focusing. These effects were first highlighted by Markstein [42] and Rudinger [61] for shock-flame interaction and later experimentally documented by Haas and Sturtevant [21].

The shocked interface system consists of five different regions as shown in Fig. 4: region 1 is unshocked ambient gas, region 2 is unshocked bubble gas, region $1'$ is shocked ambient gas, region $2'$ is shocked bubble gas after passage of the transmitted shock, and

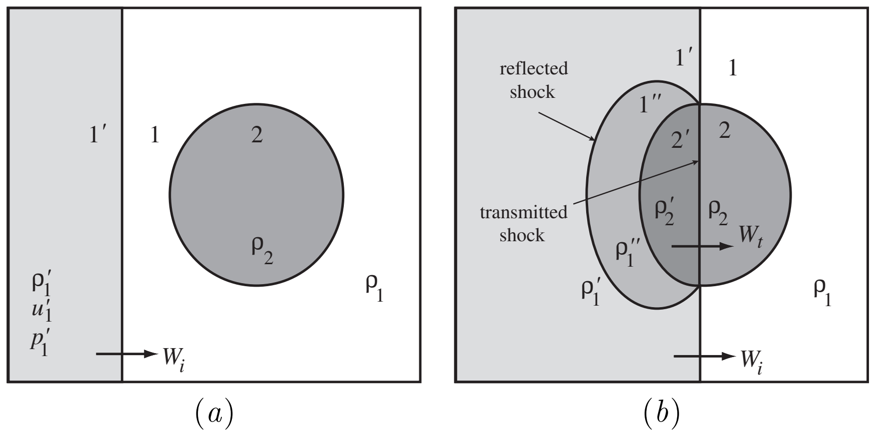

Figure 4: Schematic diagram of shocked interface system in case of shock bubble interaction: (a) pre-shock; (b) post-shock.

region $1''$ is shocked ambient gas after passage of both the initial shock and the reflected shock or rarefaction wave. Flow variables are identified using a subscript 1 for the surrounding fluid or 2 for the bubble fluid to indicate the fluid being described, and primes are used to denote the number of shock or rarefaction waves that have passed over the fluid. Hence, p_1 and p_2 represent the pre-shock pressures of the ambient and bubble fluids, respectively, and p_1' and p_2' represent the pressures after the passage of first shock.

2.4.1 Shock compression and acceleration

The passage of a shock over a bubble leads to compression of the bubble and a sudden jump in fundamental thermodynamic quantities such as pressure, temperature, and density. The bubble pressure, temperature, and density, as well as its translational velocity, must all increase, according to the Rankine-Hugoniot conditions, as the transmitted shock wave passes through the bubble. Considering the flow across the shock wave is adiabatic ($i.e$, no heat addition or removal at the boundary), the sudden jump in fundamental quantities can be derived from the conservation of mass, momentum, and energy equation. In the shock wave reference frame, the normal shock relations are stated as:

$$\rho W = \rho' \left(W - u'\right), \qquad (Continuity) \tag{2.5}$$

$$p + \rho W^2 = p' + \rho' \left(W - u'\right)^2, \qquad (Momentum) \tag{2.6}$$

$$h + \frac{W^2}{2} = h' + \frac{\left(W - u'\right)^2}{2}, \qquad (Energy) \tag{2.7}$$

where W indicates shock wave velocity, u' denotes velocity of the fluid behind the shock wave, and h (h') defines enthalpy of the fluid ahead (behind) of the shock wave. For a calorically perfect gas with a known specific heat ratio γ, we can add the thermodynamic relations

$$p = \rho R T \tag{2.8}$$

$$h = \frac{\gamma R T}{(\gamma - 1)}, \tag{2.9}$$

where R is the specific gas constant. Equations (2.5) through (2.9) constitute five equations with five unknowns. Hence, they can be solved algebraically to obtain the shocked state variables.

2.4.2 Nonlinear-acoustic effects

The second aspect of shock-bubble interaction deals with "nonlinear-acoustic effects", which refer to the refraction, reflection, and diffraction of the incident shock wave by the bubble. The bubble alters the shape and propagation pattern of the shock wave by nonlinear-acoustic mechanisms associated with the interface curvature and acoustic impedance mismatch at the interface. Due to the acoustic impedance mismatch at the bubble boundary, the bubble acts like a diverging or converging lens. The acoustic impedance, $\mathcal{R} = \rho c$, is defined as the product of the density of the gas and the sound speed (c) in that medium. The acoustic impedance is a thermodynamic property, and is peculiar to the propagation medium. The acoustic impedance is a measure of the stiffness of a material, in the sense that it is a proportionality constant between impressed velocity and applied pressure (the usual elastic moduli however correspond to ρc^2) [69]. The change in acoustic impedance between two media is known as the "impedance mismatch," $\delta\mathcal{R} = \mathcal{R}_2 - \mathcal{R}_1$. Neglecting the curvature of the bubble interface, shock passage over the bubble surface can be analyzed easily using a one-dimensional approach.

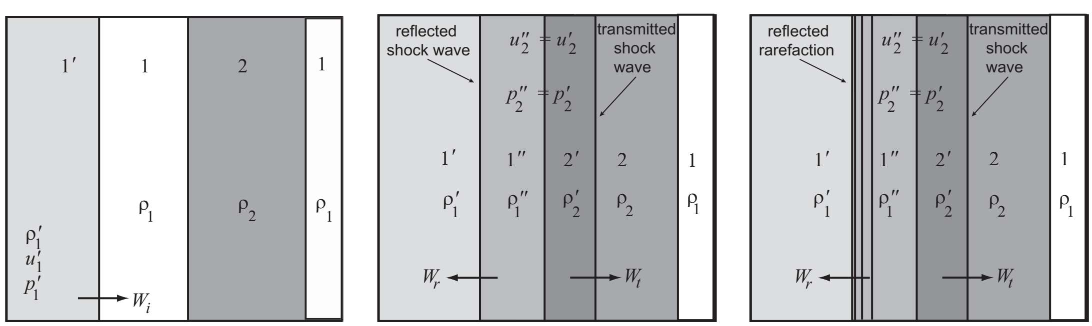

(a) (b) (c)

Figure 5: Schematic diagram of one-dimensional shock wave transmission and reflection in a gas slab: (a) pre-shock; (b) post-shock, $\mathcal{R}_2 > \mathcal{R}_1$; (c) post-shock, $\mathcal{R}_2 < \mathcal{R}_1$.

Figure 5 shows shock wave transmission and reflection in a gas slab labeled as fluid 2. Two different post-shock scenarios are analyzed based on the sign of the impedance mismatch term ($\delta\mathcal{R}$) at the interface. If $\delta\mathcal{R} > 0$, the shock wave decreases in speed after transmission, and in order to maintain the mechanical equilibrium at the interface, the initial gas must contract. Therefore, in this scenario the reflected wave is a shock wave as shown in Fig. 5(b). Conversely, if $\delta\mathcal{R} < 0$, the shock wave increases in speed after transmission, and in order to maintain the mechanical equilibrium at the interface, the initial gas must expand. Thus, in this scenario the reflected wave is a rarefaction wave as shown in Fig. 5(c). The transmitted wave is always a shock wave being independent of the impedance of the medium and shape of the interface. Figure 6 shows the wave diagram for both cases.

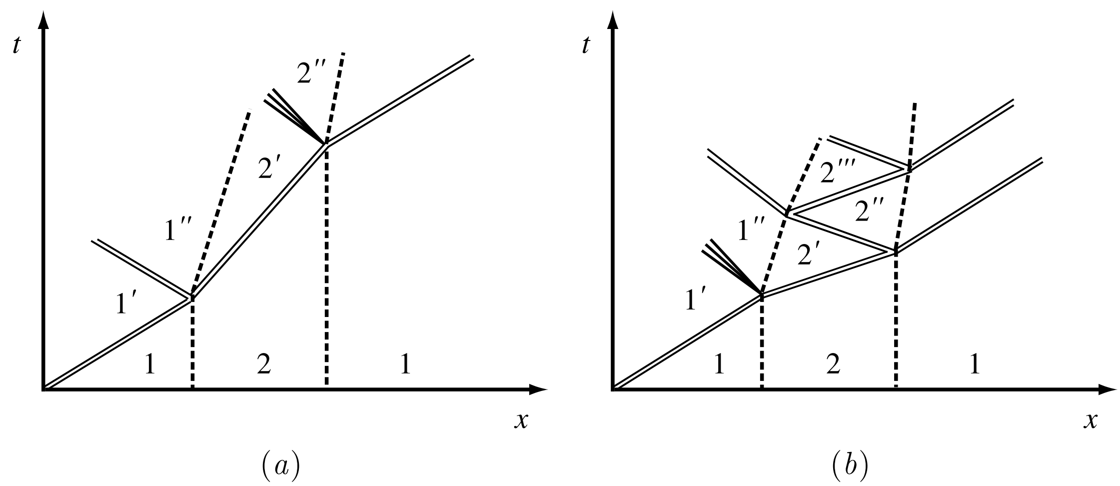

Figure 6: Wave diagram of one-dimensional shock transmission and reflection in a gas slab: (a) $\mathcal{R}_2 > \mathcal{R}_1$; ($b$) $\mathcal{R}_2 < \mathcal{R}_1$. Solid double lines indicate shock waves, dashed lines indicate fluid interfaces, and triple diverging solid lines indicate rarefaction waves [47].

Shock propagation through the bubble can be considered as an extension of the gas slab problem. Lets consider the case where medium 2 in the gas slab scenario is replaced by a cylindrical or spherical bubble. Figure 7 highlights the effect of the bubble interface curvature, on the shock refraction pattern for two different impedance mismatch scenarios. Figure 7(a) shows the shock refraction pattern for $\delta\mathcal{R} > 0$. This situation is commonly referred as “convergent geometry”. The transmitted shock wave

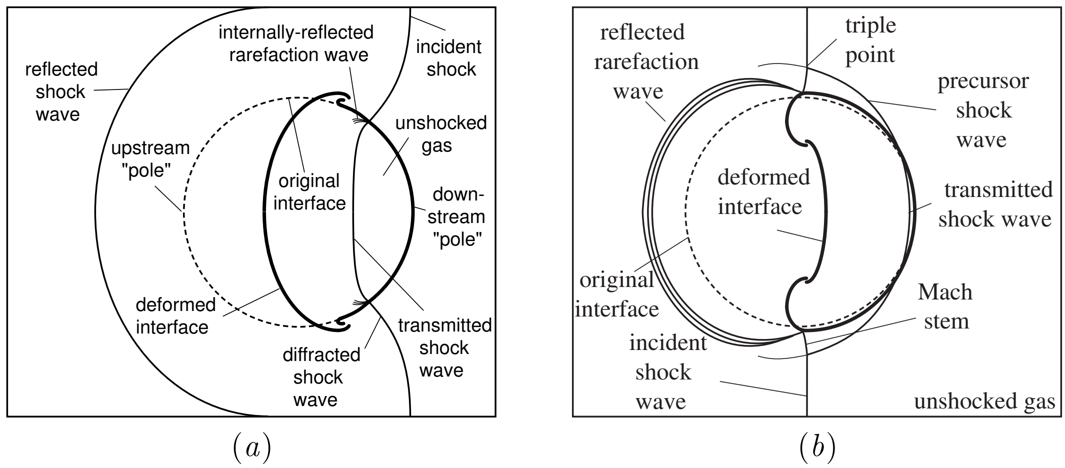

Figure 7: Schematic representation of shock-bubble interaction flowfield and shock refraction patterns in (a) convergent $(\delta\mathcal{R} > 0)$ scenario, and (b) divergent $(\delta\mathcal{R} < 0)$ scenario, shortly after initial shock wave transit. Incident shock wave propagation is left-to-right [47].

is concave in shape, and runs behind the unrefracted incident shock, and the reflected wave is a shock. Figure 7(b) highlights the shock refraction pattern for the "divergent geometry" where $\delta\mathcal{R} < 0$ at the interface, and the reflected wave is a rarefaction. In this situation, at low angles of incidence, regular refraction occurs where the transmitted wave and incident wave intersect the interface at the same point. At higher angles, various aspects of irregular refraction are observed [23, 24]. A transmitted shock wave quickly transits the bubble, and a Mach stem, precursor shock, and triple point form just outside the interface. Such features are absent in the case of the divergent geometry. In the case of convergent geometry, for high density contrast, irregular refraction of the shock wave leads to shock focusing. As depicted in figure 8, a portion of the shock wave front sweeping around the bubble periphery is diffracted, meaning it is turned toward the axis so that the surface of discontinuity remains nearly normal to the interface [21, 48].

The diffracted shock wave then meets at the downstream pole. Figure 8 shows the different stages of shock refraction in the case of convergent geometry, leading to the shock focusing at the downstream end of the bubble. The diffracted shock wave collision, along with the focusing of the transmitted shock wave, produces an intense pressure jump and initiates additional baroclinic vorticity deposition. Secondary shock waves are generated due to shock focusing, which can lead to dramatic changes in the observed flow field at late times. This effect can be compared to a reshock phenomenon, familiar from Richtmyer-Meshkov flows in shock tubes.

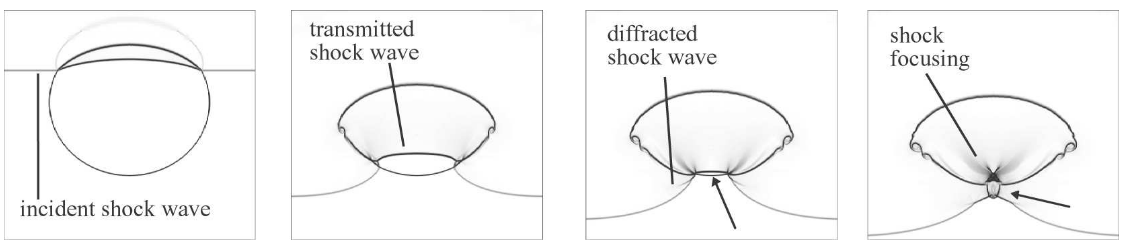

Figure 8: Representative, schematic view of shock focusing in the case of convergent geometry. The arrow in the diagram indicates the location of the shock focusing. Incident shock wave propagation is top-to-bottom.

2.4.3 Vorticity production and transport

The third and probably most important aspect of shock-bubble interaction is the vorticity deposition due to the misalignment of the pressure and the density gradients. Vorticity is defined as

$$\boldsymbol{\omega} \equiv \nabla \times \mathbf{U}. \tag{2.10}$$

If one takes the curl of the momentum equation for a compressible Navier-Stokes fluid, then one obtains the vorticity transport equation given as:

$$\frac{D\boldsymbol{\omega}}{Dt} = (\boldsymbol{\omega}\cdot\nabla)\,\mathbf{U} - \boldsymbol{\omega}\,(\nabla\cdot\mathbf{U}) + \frac{1}{\rho^2}\,(\nabla\rho\times\nabla p) + \nu\nabla^2\boldsymbol{\omega}. \tag{2.11}$$

The first term on the right $(\boldsymbol{\omega}\cdot\nabla)\,\mathbf{U}$ is the vortex stretching term, which is essential for discussion of three-dimensional turbulence and mixing. This term represents the stretching, as well as, the turning and tilting of the vortex lines by gradients in the velocity field. Vortex stretching also reflects the principle of conservation of angular momentum. Stretching decreases the moment of inertia of fluid elements that comprise a vortex line, resulting in an increase of their angular speed. The vortex stretching and tilting term is absent in two-dimensional flows, in which $\boldsymbol{\omega}$ is perpendicular to the flow.

The second term on the right $\boldsymbol{\omega}\,(\nabla\cdot\mathbf{U})$ represents the vortex dilatation term, which is important only in the case of highly compressible fluids. The last term on the right $\nu\nabla^2\boldsymbol{\omega}$ represents the rate of change of $\boldsymbol{\omega}$ due to molecular diffusion of vorticity, in the same way that $\nu\nabla^2\mathbf{U}$ represents the acceleration due to the diffusion of velocity. Dissipative effects can be neglected in our discussion here because of the low physical viscosities of the fluids considered in this dissertation. The third term on the right $(\nabla\rho\times\nabla p)\,/\rho^2$ is a baroclinic term, which represents the rate of generation of vorticity due to baroclinicity in the flow. It shows that the misalignment of the local pressure and density gradients leads to the generation of vorticity in the flow field.

In the case of a shock-bubble interaction, initially $\boldsymbol{\omega}= 0$ everywhere. Therefore, the vortex stretching and dilatation term in Eq. 2.11 drop out. In the absence of dissipative effects, Eq. 2.11 reduces to

$$\frac{D\boldsymbol{\omega}}{Dt} = \frac{1}{\rho^2}\,(\nabla\rho\times\nabla p)\,, \tag{2.12}$$

suggesting that baroclinicity is the only source for vorticity production in the flowfield at time zero. The vorticity distribution at the early stage of the shock-bubble interaction is shown in Fig. 9.

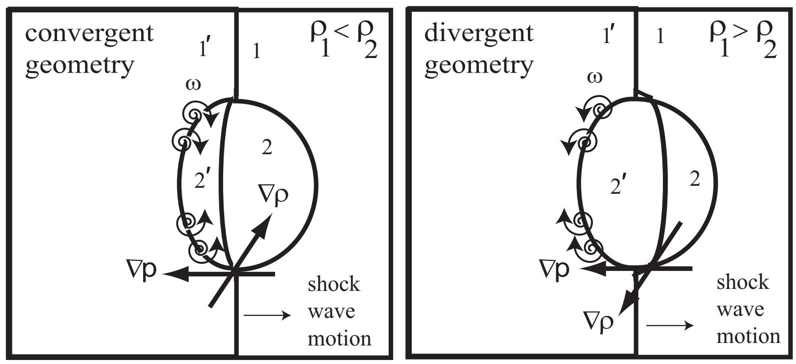

Figure 9: Schematic representation of baroclinic vorticity distribution in the early phase of shock-bubble interaction.

Vorticity is deposited locally on the fluid interface during the shock wave propagation across the bubble. The magnitude of the vorticity deposited locally is determined by the non-collinearity of $\nabla\rho$ and ∇p. The maximum misalignment is at the diametral plane, and the maximum vorticity is deposited at this location. This leads to the formation of a primary vortex ring near the diametral plane. The rotation of the primary vortex ring is driven by the orientation of the density gradient at the bubble interface. Figure 9 shows the direction of rotation in the case of convergent and divergent geometry of the bubble, and the primary vortex ring is the dominant feature of the flow.

The features observed in the flow field are similar to those found in the Richtmyer-Meshkov instability. Although the shock refraction pattern is dictated by the impedance mismatch at the interface, this phenomenon only exists during the early phase of the flow. After several shock-passage times (D/W), the features observed in the flow field are dominated by the vortical motion. Therefore, the Atwood number will be used in this dissertation to indicate the effect of density contrast at the bubble interface rather than the impedance mismatch. For the gas pairs considered here, $A > 0$ refers to convergent geometry ($\delta\mathcal{R} > 0$), and $A < 0$ refers to divergent geometry ($\delta\mathcal{R} < 0$). It is well known that in some unusual conditions, it is possible to have convergent refraction ($\delta\mathcal{R} > 0$), even if $A < 0$, and *vice versa*. This is possible if the effect from the specific heat ratios offsets the changes in density, and such cases do not appear in this study.

The three underlying physical processes outlined above are nonlinearly coupled together. Their simultaneous action in shock-bubble interaction leads to the development, in many cases, of highly complex regions of strong, disordered rotational motion and mixing. This has been a challenge to experimentalists, theorists, and computer modelers alike. Over the last four decades a rich database of literature has developed studying shock-bubble interaction, outlined below in Sec. 2.5- 2.7.

2.5 Shock Tube Experiments

In 1987, Haas and Sturtevant [21] reported on experiments conducted in a horizontal shock tube studying the interaction of a light or heavy gas bubble subjected to a planar shock wave. The spherical shapes were produced using soap bubbles filled with either a light or a heavy gas, while the cylindrical inhomogeneities were encapsulated in thin nitrocellulose membranes. The wavefront geometry and the deformation of the gas volume were visualized by shadowgraph photography. Wave configurations predicted by geometrical acoustics, including the effects of refraction, reflection, and diffraction, were compared to the observed flow field. It was shown that, in the case of a cylindrical or spherical volume filled with a heavy (low-sound-speed) gas, the wave which passes through the interior focuses just on the downstream pole of the cylinder. On the other hand, the wave which passes through a light (high-sound-speed) volume strongly diverges. The distortion of the helium cylinder in an air environment at large times showed that the interaction of a shock wave with a gas lighter than its surrounding develops into a pair of vortices which move faster than the ambient fluid. In the case of a helium sphere at late times it was observed that the primary vortex ring splits off from the main structure and propagates along the axis of symmetry. No vortex ring could clearly be resolved in the images (see Fig. 10) obtained from the heavy bubble, however its existence was inferred from the velocity measurements.

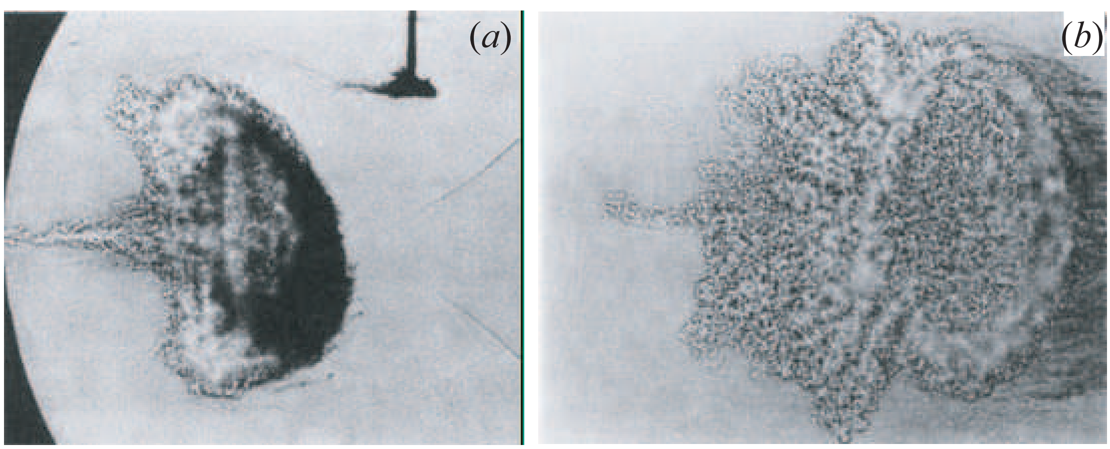

Figure 10: Shadow-photographs from Haas and Sturtevant [21] experiments of a R22 sphere (3.5 cm high, 2.5 cm wide) after interaction with a M=1.25 shock wave moving from right to left; (a) $t = 507$ μs, (b) $t = 1.56$ ms.

In the early 1990's, Jacobs [27, 28] implemented a new technique, in which a laminar jet was used to produce the gas cylinder, eliminating the need for a membrane to encapsulate the heavy or light gas [21]. The shortcomings of shadowgraphy were eliminated in the experiments by utilizing planar laser induced fluorescence (PLIF). In these experiments SF_6 or helium was seeded with a small amount of biacetyl and then made to fluoresce with a laser sheet. The technique was utilized for obtaining excellent visualizations of the flow and quantitative characterization of mixing.

In 2003, Tomkins *et al.* [70] reported on the evolution and interaction of two shock-accelerated, heavy-gas (SF_6) cylinders as an extension to the single-cylinder problem. Planar laser imaging was utilized for flow visualization. An intensified camera, aligned normal to the laser sheet was used to capture the light scattered from the bubble gas (seeded with a small amount of glycol/water fog droplets) during the evolution phase, and velocity measurements were performed using digital particle image velocimetry. The visualization revealed that the flow morphology is highly sensitive to the initial separation between the cylinders. Later in 2005, the two-cylinder system was extended to a three or more cylinders configuration by Kumar *et al* [33], with one of five different configurations of heavy-gas (SF_6) cylinders surrounded by air being impulsively accelerated to produce one or more pairs of interacting vortex columns. The flow was visualized using planar laser-induced fluorescence in the plane normal to the axes of the cylinders, and it was found that the number, configuration, and orientation, of gaseous cylinders affects the shock-induced mixing in terms of the generation of interfacial area.

More recently Layes *et al.* [35, 36] have reported experiments studying the interaction of a planar shock wave with a spherical gas inhomogeneity (soap bubble). These experiments were conducted in a horizontal shock tube with the bubble supported by a holder and subjected to a $M < 1.3$ shock wave in air. Different gas bubbles (helium, nitrogen, and krypton), were introduced in air at atmospheric pressure. The bubble distortion was visualized via a multiple exposure shadowgraph diagnostic as shown in Fig. 11. A primary vortex ring was observed in the case of the helium bubble. No particular deformation was observed in the case of the nitrogen bubble, except the weak compression of the bubble and, due to the presence of the bubble holder, some perturbations were generated on the bottom part of the bubble. For the krypton bubble scenario, one can clearly visualize the shock focusing on the downstream pole of the bubble. The deformation pattern was significantly different than that observed in the case of the helium bubble. It was shown that the gaseous mixing length is linear in time after the compression phase of the bubble.

2.6 Theory and simulation

Rudinger and Somers [62] developed a simplified theoretical model for the interaction of a shock wave with a bubble which leads to the calculation of the initial bubble velocity V_b and final vortex velocity V_v. The model assumes that the bubble is initially accelerated by the shock to a velocity V_b, different from the shocked ambient gas velocity u_1'. For the early phase they treated the bubble as if it were a solid particle. The calculation assumes an impulsive, essentially incompressible acceleration. The impulse per unit volume I transmitted by the shock to the gas bubble is precisely that which the ambient gas would have experienced,

$$I = \rho_1' u_1' = \rho_2' V_b + k\rho_1' \left(V_b - u_1'\right), \tag{2.13}$$

where ρ_2' is the post shock bubble gas density while ρ_1' denotes post shock ambient gas density. The term $\rho_1' k(V_b - u_1')$ represents the impulse transmitted to the ambient gas around the bubble due to the bubble motion and k is the inertial coefficient or apparent additional mass fraction. For a spherical bubble, k=0.5, and for an infinitely long cylinder moving at right angles to its axis, k=1.0 [34]. From Eq. 2.13 the bubble

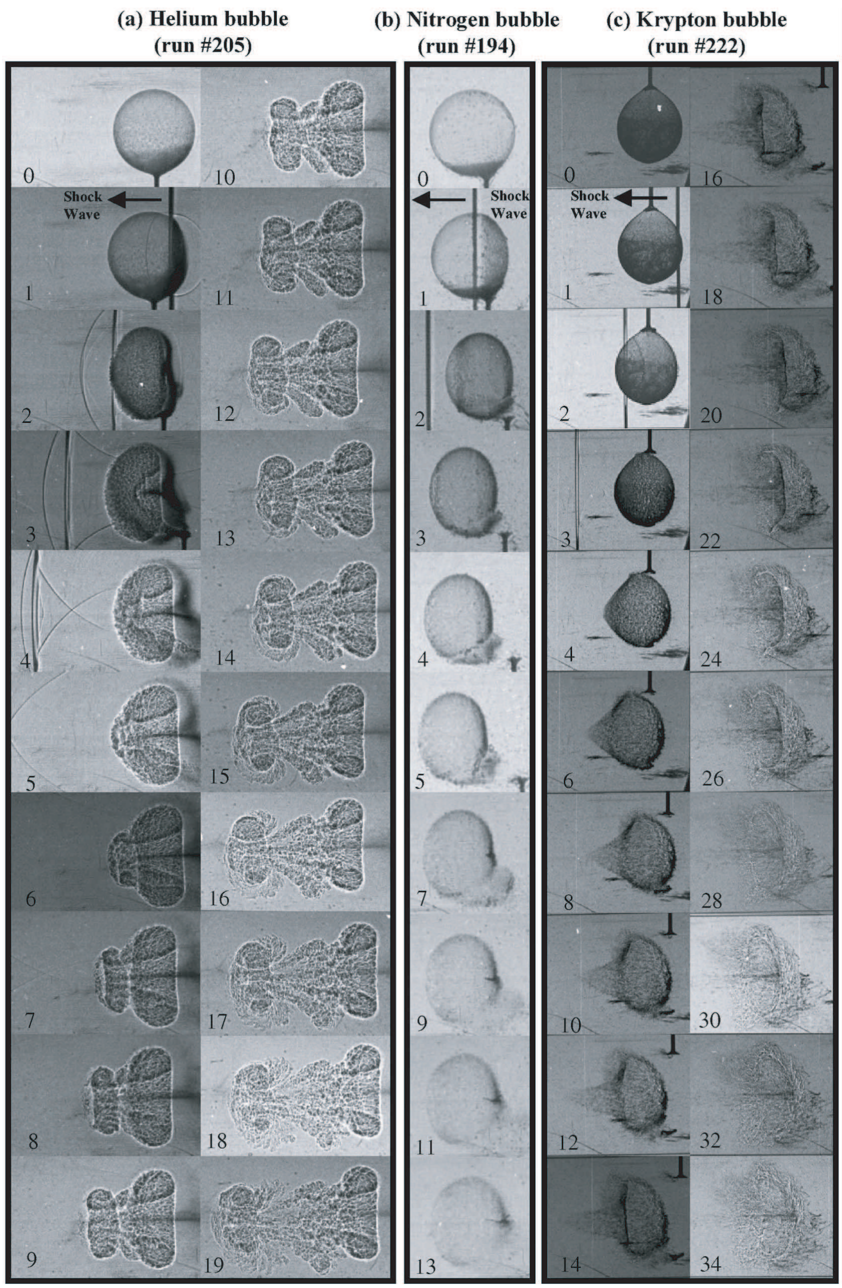

Figure 11: Shadowgraph frames of the interaction between a shock wave moving in air and a gaseous bubble for (a) helium bubble, (b) nitrogen bubble, and (c) krypton bubble [35]. The incident shock wave is moving from right to left and two consecutive images are separated by 70μs.

velocity immediately after the passage of the shock wave is given by

$$V_b = \left(\frac{1+k}{\sigma+k}\right) u_1', \tag{2.14}$$

where $\sigma = \rho_2'/\rho_1'$ is the post-shock density ratio. The second step of the analysis deals with the transformation of the gas bubble into a vortex, where the energy absorbed by the vortex is provided by the kinetic energy of the initial motion, which leads to the decrease of the relative velocity

$$V_v - u_1' = \beta\left(V_b - u_1'\right). \tag{2.15}$$

Using a calculation by Taylor [67] for the generation of a vortex ring by the impulsive acceleration of a disk, they arrive at the vortex velocity given as

$$V_v = \left(1 + \beta\frac{1-\sigma}{\sigma+k}\right) u_1', \tag{2.16}$$

where β=0.436 [67] for the vortex ring (spherical bubble scenario) and β=0.203 [62] for the infinitely long vortex pair (cylindrical bubble scenario).

The first detailed numerical investigation of the shock-bubble interaction in two dimensions was performed by Picone and Boris in 1988 [51], who modeled the experiments conducted by Haas and Sturtevant [21] for both cylinders and spheres. The results were in reasonable agreement with the experiments. They captured the development of the vortical features which were observed in the experimental work of Haas and Sturtevant [21]. They also presented a model for the calculation of the late-time bubble velocity, and the magnitude of the vortex strength, or circulation, Γ. The velocity model was intended to capture the motion of the entire volume of shocked bubble fluid, but it will be shown later in this dissertation that it provides a good agreement with the bubble vortex velocity. The circulation Γ is a scalar quantity having considerable importance in the description of the vortical flows. The circulation Γ is defined around a simple closed curve C as a line integral of the velocity given as:

$$\Gamma = \oint_C \mathbf{U} \cdot d\mathbf{s}. \tag{2.17}$$

It follows from Stokes's theorem that the circulation around a reducible curve is equal to the flux of vorticity through an open surface A bounded by the curve [63], that is,

$$\Gamma = \int_A \boldsymbol{\omega} \cdot d\mathbf{S}. \tag{2.18}$$

The circulation model provided by Picone and Boris is based on the initial properties of the shocked gas, unshocked ambient gas, and the bubble. They utilized Eq. 2.18 to obtain the circulation in one half of the bubble, with the only source term for the vorticity being the baroclinic term. The circulation model by Picone and Boris may be written as

$$\Gamma_{\mathrm{PB}} \approx 2u_1' \left(1 - \frac{u_1'}{2W_i}\right) \left(\frac{D}{2}\right) \ln\left(\frac{\rho_1}{\rho_2}\right), \tag{2.19}$$

and the vortex velocity by

$$V_v \approx u_1' + \frac{\Gamma_{\mathrm{PB}}}{2\pi D_v}, \tag{2.20}$$

where D_v is the major diameter of the vortex ring, and D is the initial diameter of the bubble.

Yang, Kubota and Zukoski (henceforward, YKZ) in 1994 [72], investigated the shock-cylinder interaction numerically and worked along the same path as Picone and Boris to calculate the circulation. The circulation predicted by the YKZ model is

$$\Gamma_{\mathrm{YKZ}} \approx \frac{2D}{W_i} \frac{p_1' - p_1}{\rho_1'} \left(\frac{\rho_2 - \rho_1}{\rho_2 + \rho_1}\right). \tag{2.21}$$

In 1996, Quirk and Karny [55] reported a detailed numerical study of the shock-bubble interaction utilizing a sophisticated adaptive mesh refined algorithm, with a nonconservative shock capturing scheme. The adaptive mesh refinement technique enabled them to produce high resolution results at low cost, and the simulations successfully resolved the shock refraction pattern and vortical features observed by Haas and Sturtevant. Several additional numerical studies have been carried out in the past, which were also motivated by the experimental work of Haas and Sturtevant [21]. In 1989, Cowperthwaite [10] produced two-dimensional simulations of the distortion and motion of an initially spherical mass of Freon 12 gas suspended in a lighter gas (air or helium) surrounding. The simulations were carried out to late-times and the velocity of the center of mass of the bubble was calculated as a function of time. A simple model, based on the concepts of drag, added mass, and entrainment, was shown to give a good agreement with the bubble velocity observed in the simulation.

In 1994, Samtaney and Zabusky produced an in-depth analysis of the baroclinic vorticity deposition on a planar interface using shock polar analysis. This was extended to the spherical case using a "near-normality" condition, which in our notation is written as

$$\Gamma_{\mathrm{SZ}} = \left(1 + \frac{\pi}{2}\right)\left(\frac{2}{1+\gamma}\right)\left(1 - \chi^{-\frac{1}{2}}\right)\left(1 + M^{-1} + 2M^{-2}\right)(M-1)\,(D/2)\,c_1, \tag{2.22}$$

where χ defines the density ratio across the interface. The model shows that for large χ, circulation is independent of the density ratio, and for high Mach number flows, it shows that circulation has a linear behavior in M. This model has been shown to be effective for the convergent geometry shock-bubble interaction. Zabusky and Zeng [74] in 1998 reported on numerical investigations of the interaction of planar shocks with a Freon 12 axisymmetric spherical bubble in air. In this paper, they extended the early axisymmetric simulations by Picone and Boris to high Mach numbers up to $M = 5$ and observed the formation of a secondary vortex ring at the apex of the bubble for shock strengths M= 2.5 and 5.0. The formation of the secondary vortex ring was attributed to secondary shocks which can arise in the higher shock strength scenario. Levy *et al.* [38] used an interface-tracking two-dimensional ALE hydrodynamic code to simulate the shock-bubble interaction and was motivated by the experimental work performed by their group. They extended the circulation model of Samtaney and Zabusky to the scaling of the velocity field and showed that the velocity of the bubble is independent of the bubble radius, and also, that the scaling of the velocity failed for $M > 2$.

The experiments of Layes *et al.* [35] have been simulated numerically by Giordano and Burtschell [17], and Layes and LeMétayer (2007) [37] and both displayed good agreement with the experiments. The numerical schlieren image of a krypton bubble accelerated by a M=1.7 shock showed a small secondary vortex ring at the apex of the bubble [17]. Giordano and Burtshell also presented an analytical approach to evaluate the final volume of the inhomogeneity after the shock interaction. Numerically, extensive work has been done to study the shock-cylinder interaction. The experiments of Haas and Sturtevant [21] have also been simulated recently by Marquina and Mulet [43], using very high spatial resolution, showing the growth of distinctive turbulent features in the flow field at late-times. Greenough *et al.* [20] implemented a high- order Godunov method in an adaptive mesh refinement environment to study this problem, and successfully resolved many of the fine scale details of the complex, highly vortical flow field observed in Jacobs's experiments. Zoldi [75] has also proposed a numerical study of her own experiments, and showed that, at late-times, waviness appears along the interface with a characteristic length scale much smaller than that associated with the primary vortex structure. Bagabir and Drikakis [3] have studied the influence of incident shock strength on the cylindrical behavior with the same geometrical characteristics as Haas and Sturtevant's experiments.

More recently, a parameter study for shock-bubble interactions has been carried out by John Niederhaus [47] using a series of three-dimensional multifluid Eulerian simulations. This work included a detailed analysis of various integral features of the shock-bubble interaction, and it was shown that, although this problem shows a very complex flow field, features like mean density, and bubble velocity can be scaled over a wide range of M for a fixed A using quantities calculated from one-dimensional gasdynamics. Notable differences from the typical shock-bubble interaction morphology have been reported recently by Niederhaus *et al.* [48] for scenarios with $M > 2$ and $A > 0.5$. In these scenarios the flow field mostly contains a diffuse turbulent plume at late time rather than coherent vortex structures.

2.7 Laser-Driven Experiments

Several shock-driven experiments for a spherical inhomogeneity have been carried out successfully at high Mach number ($M \sim 10$) using both the Omega laser at the Laboratory of Laser Energetics [60, 22] and the NOVA laser at LLNL [30, 31]. Klein *et al.* [30] utilized the NOVA laser to generate a strong shock wave ($M = 10$) which traveled within a miniature beryllium shock tube, 750 μm in diameter, filled with a low-density plastic. Embedded in the plastic was a copper sphere 100 μm in diameter. Its morphology and evolution, as well as the shock trajectory, were diagnosed via side-on radiography. Beryllium was used for the shock tube wall material since it is essentially transparent to the X-rays that are used to diagnose the target evolution. The experiments showed the initial distortion of the copper sphere into a vortex ring structure. Klein *et al.* [31] compared the experimental results [30] to detailed two- and three-dimensional radiation hydrodynamic simulations which showed the initial distortion of the bubble into a vortex ring and later the breakup of the vortex ring due to the azimuthal bending mode instability.

Robey *et al.* [60] conducted a similar set of experiments on the Omega laser. They simultaneously performed side-on and face-on radiography to construct the three-dimensional topology of the interaction. This enabled them to visualize both the initial distortion of the copper sphere into a double vortex ring structure and the onset of the azimuthal instability. The paper also included a detailed numerical study of the described experiments using a three-dimensional Eulerian adaptive mesh refinement code, which is also the same code later used by John Niederhaus [47] to perform a parametric study for the shock-bubble problem. The numerical study showed that two-dimensional codes are completely inadequate in resolving the observed azimuthal mode structures. The numerical study showed a good agreement with the observed distortion of the copper sphere. The breakup of the vortex ring due to the onset of bending-mode instabilities was also captured in the simulations.

In 2007, Hansen *et al.* [22] took the Omega experiments a step further by replacing the area radiography technique used by Robey *et al.* [60] with a point-projection radiography technique, and this vastly increased the number of photons that illuminated the shock tube, resulting in a better signal to noise ratio. The images obtained with this technique allowed them to estimate the cloud mass as a function of time. In these experiments they also replaced the copper sphere used previously by other experimenters with an aluminium sphere, to study the faster hydrodynamic evolution, for the lighter material so distortion could be studied for a longer time. Hansen *et al.* showed that the cloud mass as a function of time followed a model of turbulent-mass stripping, strongly suggesting that turbulence play an important role in the development at late times. They also showed that the cloud distortion compared quite well quantitatively with the shock tube experiments reported by Ranjan *et al.* [56] (the work described in Ranjan *et al.* [56] was performed as a part of this dissertation) for the scaled lengthwise growth of the bubble.

To summarize, the experimental, computational, and theoretical research effort studying the RMI has been mainly directed towards determining the interface growth rate. There has been relatively little experimental effort devoted to the shock interaction with a spherical interface, and the regime between the low Mach number shock tube experiments and the high Mach number laser-driven experiments has not been investigated yet. This regime is of great importance in order to understand the compressibility effects in the shock accelerated flows where a transition can occur when the particle velocity behind the shock has become supersonic. The present study is an effort to bridge this gap. Experimental results along with the use of numerical simulation and theoretical models will be utilized to understand this phenomenon over a wide range of conditions. The experimental data can be used for code validation and development of new theoretical models.

Chapter 3

Experimental Apparatus

The shocked-bubble flow field is visualized experimentally using a large shock tube with a uniquely designed test section in the Wisconsin Shock Tube Laboratory (WiSTL) at the University of Wisconsin-Madison. This facility is used for various experimental programs that are applicable to fusion energy research and astrophysics with the majority of experiments related to the Richtmyer-Meshkov instability [2, 45, 49, 54]. This facility has also been used to perform experiments on the shock loading of a solid cylinder and a cylinder bank to model the cooling tubes in an inertial fusion energy reactor. Recently, this facility has also been used to perform shock mitigation studies, for example, shock wave interactions with water layers and foams. This chapter deals, in detail, with various aspects of the experimental setup including the shock tube facility, injector system, bubble formation, and flow visualization.

3.1 Wisconsin Shock Tube

The centerpiece of the WiSTL facility is a 9.2 m, vertical, closed duct of 0.254×0.254 m square internal cross section, shown in Fig. 12, designed with an impulsive load capability of 25 MPa to accommodate static and dynamic loads associated with strong shocks. The shock tube has a modular construction, which allows for the rearranging of the shock tube for different experimental configurations. The large internal cross-section allows

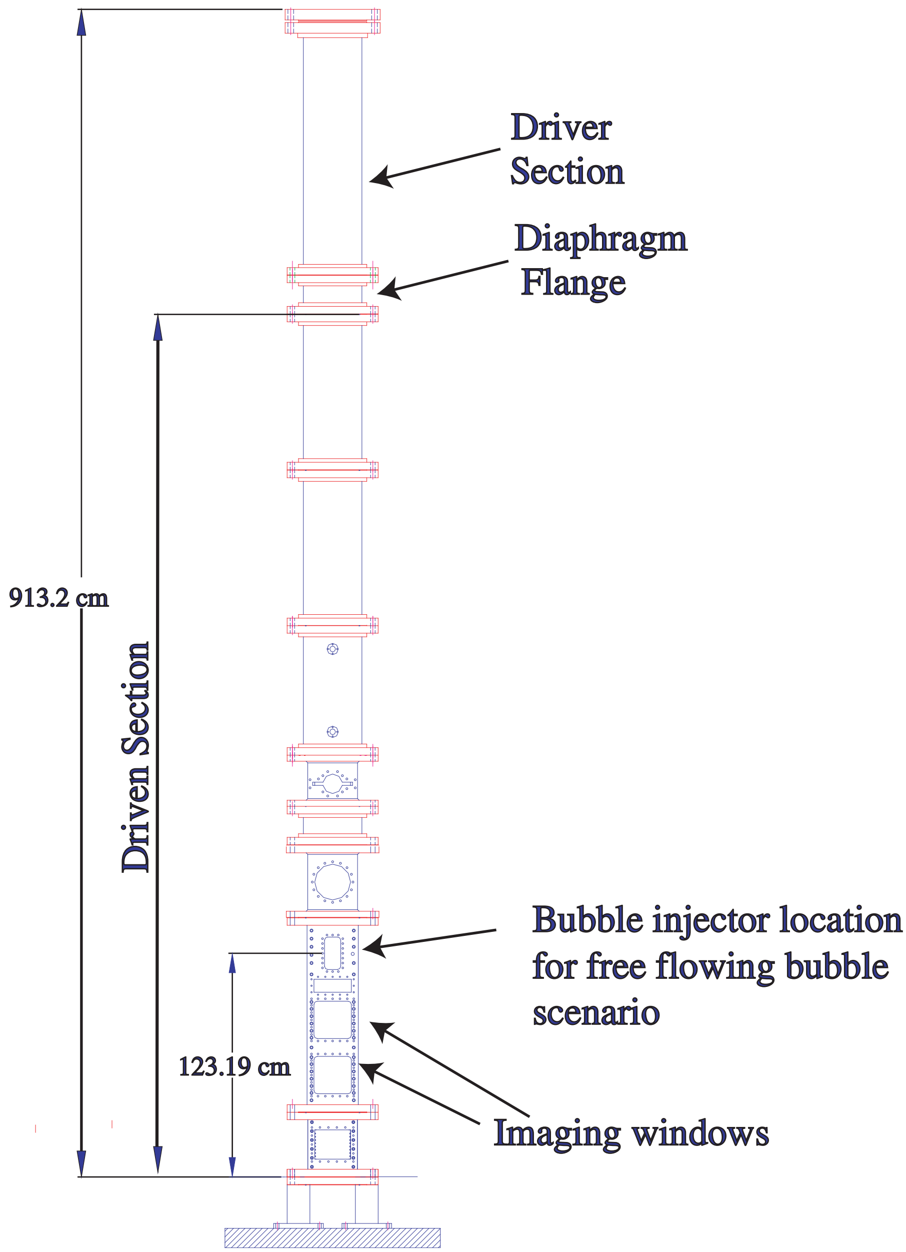

Figure 12: Schematic representation of Wisconsin shock tube.

for minimizations of boundary layer effects. A downward-moving shock wave is released by discharging two boost tanks, through a fast-opening valve, into the driver section, pressurized to about 95% of the diaphragm rupture pressure which allows control of shock release time to within ± 20 ms. Piezoelectric pressure transducers are flush-mounted along the inside and end walls of the shock tube to measure the dynamic pressure inside the tube at a sampling frequency of 1 MHz. One of these pressure transducers is also used to trigger the data acquisition system which records the pressure data and for triggering the laser pulses for imaging of the shocked-bubble flow field. Details of the imaging system will be discussed later in this chapter. A detailed description of the WiSTL facility has been reported by Anderson *et al.* [2], and for convenience, a very brief description is included here.

3.1.1 Driver section

The driver section is 2.08 m long, made from 0.472 m internal diameter chrome-plated carbon steel pipe with a wall thickness of 0.019 m. Two boost tanks (shown in Fig. 13) are connected via fast-acting pneumatic valves (FAV) to the driver section . At the top end, the driver section is closed by a 0.083-m thick flange with provisions for three gas inlet/outlet ports, a pressure gauge, and a thermocouple gauge as shown in Fig. 14. In order to change the diaphragm, the driver section is lifted using an overhead crane.

3.1.2 Diaphragm section

The diaphragm section is located directly below the driver section and holds the diaphragm and the cutting device. A shock wave is created in the driven section by placing a metal diaphragm between the driver and diaphragm sections, bolting the sections

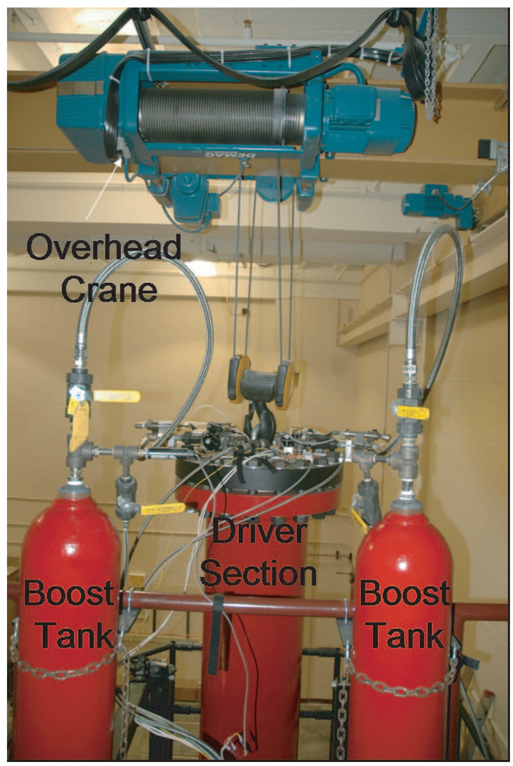

Figure 13: Photograph of the driver section of the shock tube.

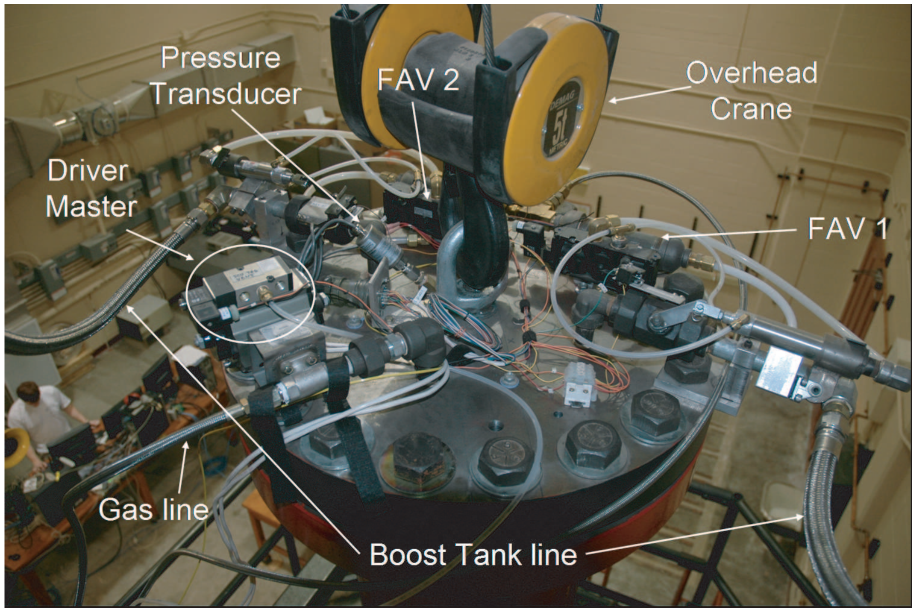

Figure 14: Photograph of the top-cap of the driver section.

together, and then pressurizing the driver until the diaphragm ruptures. The section is 0.35 m long and has an inner diameter of 0.42 m. A sharp knife-edged cruciform blade (see Fig. 15) is located right below the diaphragm, and is used to ensure consistent rupture of the diaphragm. Due to higher pressure on the driver side, the diaphragm bulges against the blades, and ruptures in the form of four petals which remain attached to the outer circumference as shown in Fig. 16.

3.1.3 Driven section

The driven section is 6.41 m long and consists of all the various modular shock tube sections that are located below the diaphragm section. The driven sections of the shock tube have an internally square cross-section formed using four 0.0095 m thick stainless steel plates, which are welded together. The volume between the steel plate and the

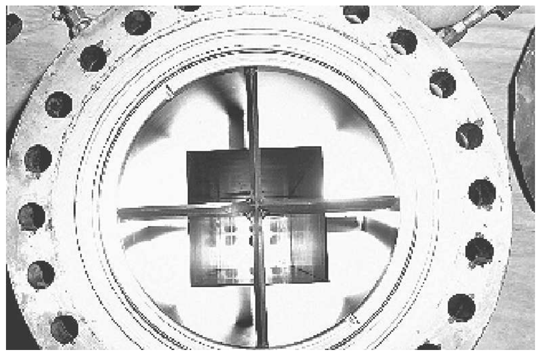

Figure 15: Knife-edged cruciform blade in the diaphragm section.

Figure 16: A thick steel (16 gauge) diaphragm ruptured when the driver pressure reaches 2.75 MPa absolute.

inside of the tube wall is filled with concrete to provide structural support to the steel plates. A schematic view of the cross-section of the shock tube driven section is shown in Fig. 17. The driven section segments are also equipped with access ports at various

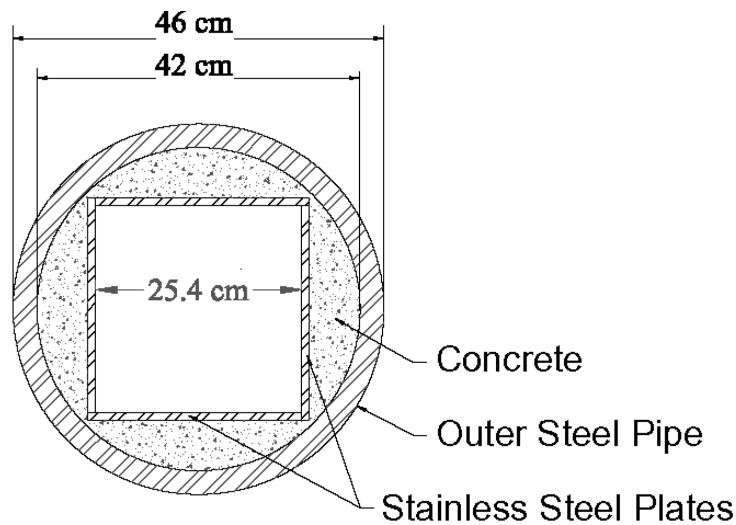

Figure 17: Schematic view of the cross-section of the shock tube driven sections.

locations where pressure transducers can be mounted to measure the speed of the shock wave. The sealing between segments is provided by an O-ring placed in a groove on the top part of each flange. There are twenty-four bolts connecting the flanges of different sections. The interface section (where the bubble is created) and the test section (where the post shock images are acquired) are combined on the same modular piece of the shock tube as shown in Fig. 18. The key features of this section are four overlapping large window ports, and seven variably sized ports on the section faces that are perpendicular to the large window ports. The large window ports are used for the imaging windows, while the side ports can be used for housing the injector system as well as for a shadowgraph photography system.

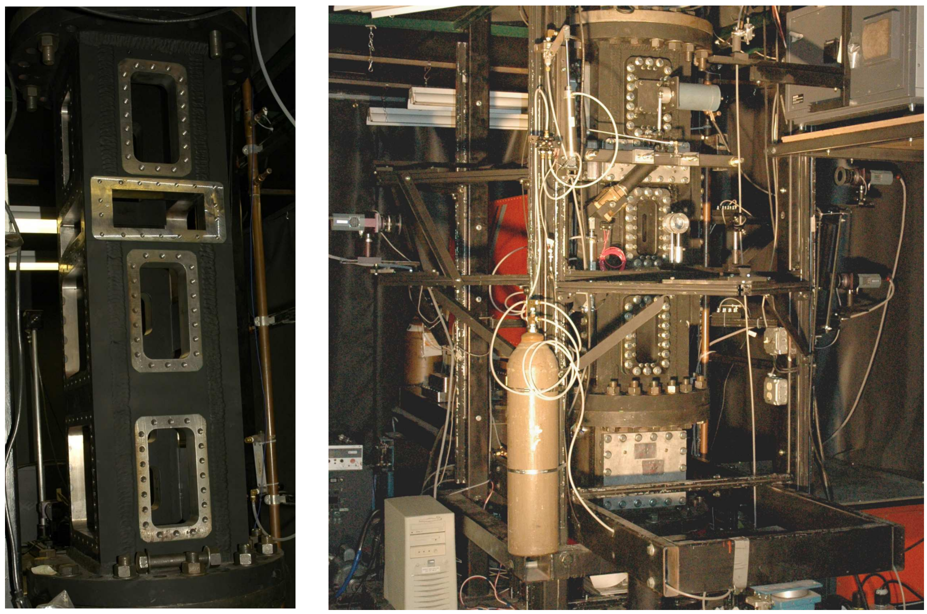

(a) (b)

Figure 18: Photographs of the interface/test section: (a) open ports; (b) closed ports and instrumentation.

3.2 Development of Retractable Injector System

An initial experimental study was conducted using a stationary bubble system [58]. For the first set of experiments, a light bubble (air) was prepared in the test section filled with argon as shown in Fig. 19(a). This setup only allowed for the study of the early (compression) phase of the shock-bubble interaction. At later post-shock times, the injector used to support the bubble in this experimental series would have obstructed the view of the bubble and significantly altered the flow field. Thus a different initial geometry was used, with a bubble hanging from an L-shaped injector (plastic tube), facing downwards as shown in Fig. 19(b). In this configuration, buoyancy would have

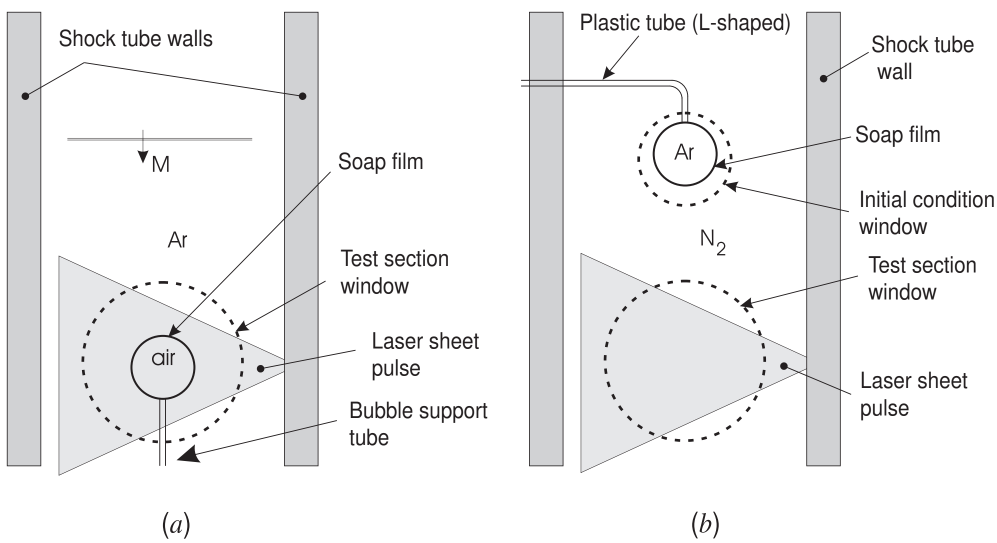

Figure 19: Injector system for stationary bubble experiments: (a) for early-time shock-bubble interaction; and (b) for late-time experiments.

the adverse effect of pushing the bubble upwards, into the injector, therefore, a bubble contains the heavy gas (argon) and the driven section is filled with nitrogen. The L-shaped injector system was still not an ideal system as leaving the injector present in the flow field disrupts the incident shock wave. Also, this setup only allows one to study the shock-bubble interaction for heavy bubbles. Therefore a new injector was designed as shown in Fig. 20 which can provide a free-rising or a free-falling bubble inside the shock tube [56, 57].

A cable connects the injector to a pneumatic piston, which is controlled via a solenoid valve. The inner wall of the injector plug sits flush with the shock tube wall. In each experiment, a bubble is formed on the stainless steel injector, which is then pneumatically retracted at high speed into a slot in the shock tube side wall in order to release the bubble. It takes 240-260 ms to completely retract the injector. This setup results in

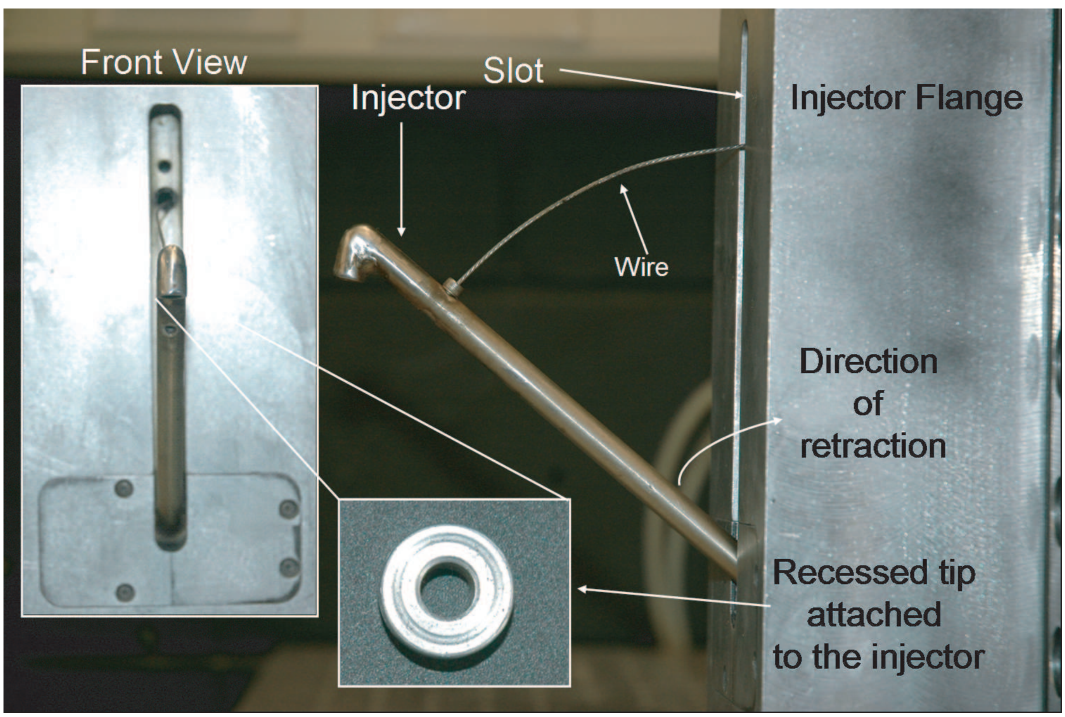

Figure 20: Photograph of the retractable bubble injector showing the front/side view of the injector plug.

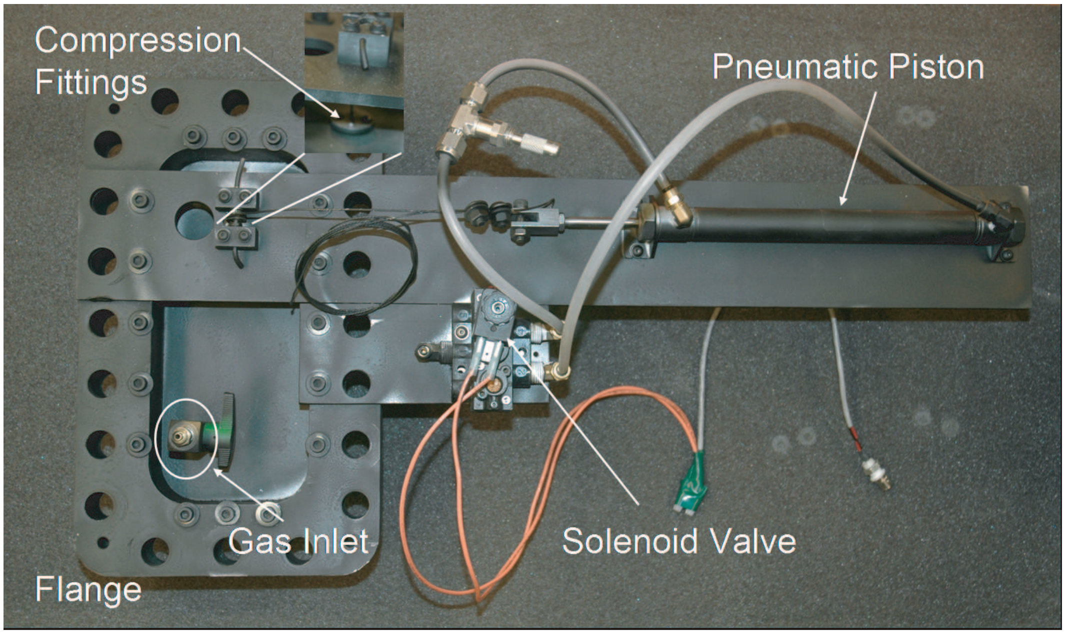

Figure 21: Photograph of the retractable bubble injector showing the back side of the injector plug.

clean experiments where the bubble is in free fall or free rise, and the disruption to the planar shock (that would occur if a holder was left in the flow cross-section) is minimized. Figures 20 and 21 highlight the important features of the retractable injector system.

3.3 Optical Diagnostics

3.3.1 Initial Condition

To characterize the bubble evolution, it is essential to have a precise knowledge of the shape and size of the bubble before shock interaction. In the case of the stationary bubble experiments, a planar-Mie-scattering image is generated by shining a laser sheet (at 532 nm) from a pulsed Nd:YAG laser (Continuum Surelite II) through the midplane of the bubble to obtain the initial condition of the bubble. The image is captured either with a LaVision camera or Andor DV434-BU2 CCD camera. Both of these cameras have the capability of storing multiple exposures on the same CCD array. Figure 22 shows the initial condition for a hanging bubble filled with argon created using the L-shaped injector system.

Figure 22: Initial condition for stationary bubble filled with Ar hanging from the L-shaped injector. The shape deviates from a sphere due to sag from both the Ar being heavier than the N_2 driven gas and also the small accumulation of fluid visible at the bottom of the bubble.

In the case of the retractable injector system, the release and free fall, or free rise, of the bubble are recorded at 250 fps with a CCD camera (DALSA CA-D1-0256A) and front lighting. This allows for imaging the evolution of the bubble during its release from the holder and provides an initial condition image of the bubble prior to (within 10 ms) shock interaction. Figure 23 shows a sequence of injector retraction and the early time oscillation of the bubble after retraction. After release, the bubble oscillates on a time scale of 100 ms, remaining nearly spherical as shown in Fig. 24. The sequence of images in Fig. 25 shows that just before shock wave interaction, the bubble is nearly spherical in shape. It is also evident from the images that the bubble does not deviate from its free fall trajectory.

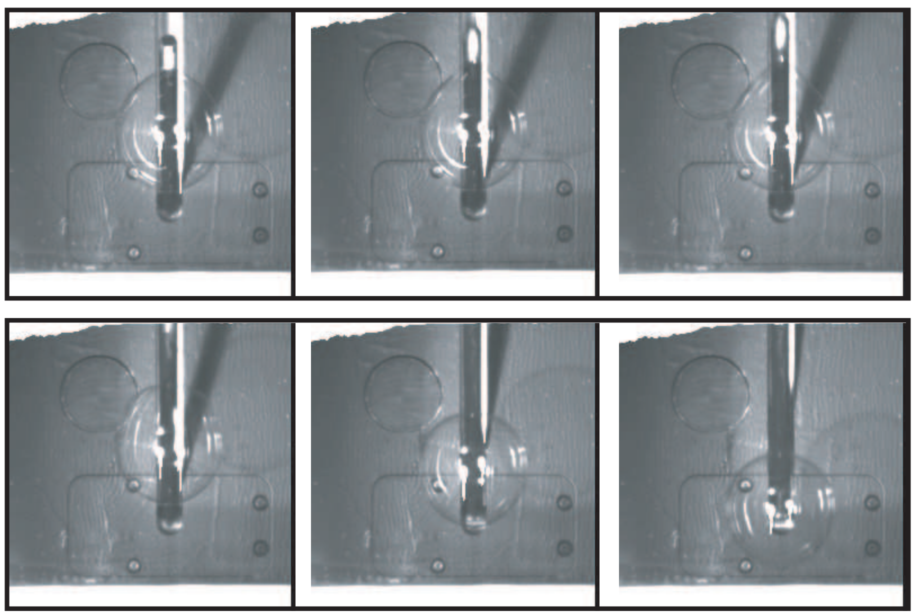

Figure 23: Sequence of images showing the retraction of the injector and early time free fall of an Ar bubble in the driven section of the shock tube filled with N_2. The first image shows the bubble being held by the injector prior to retraction and arrival of the shock wave. The bubble is slightly elliptical immediately after the retraction as seen in the next three images. The last image shows the injector is retracted into the slot present in the shock tube.

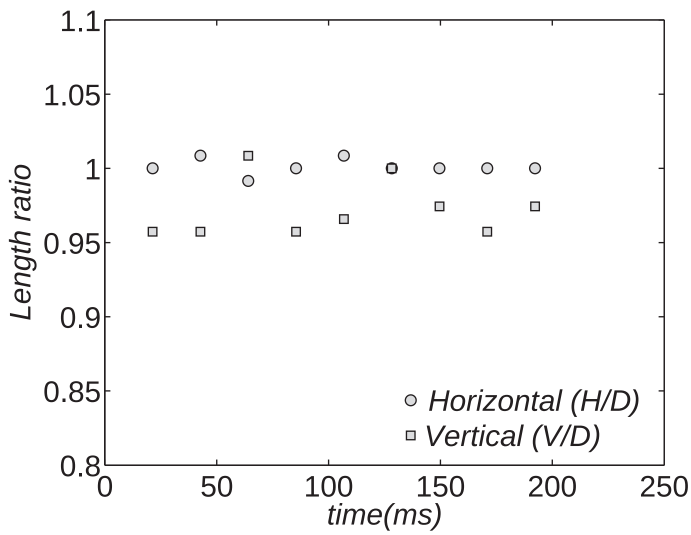

Figure 24: Measurement of oscillation of a heavy bubble with respect to time, after release, from the retractable injector system. D is the initial diameter of the bubble.

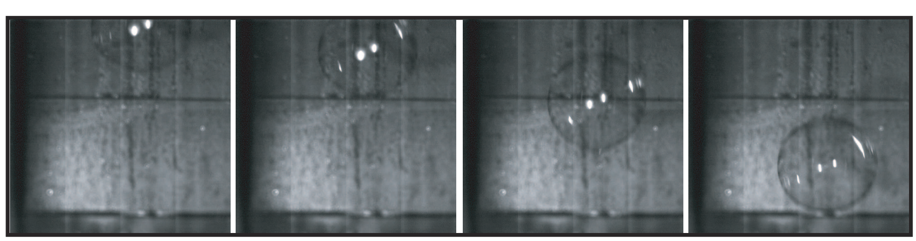

Figure 25: Sequence of images showing the free fall of an Ar bubble in the window directly below the injector system after retraction. The last image is just prior to the shock wave interaction and shows the bubble has regained its near-spherical shape.

3.3.2 Post-Shock Imaging

The evolution of the flow structures is captured using planar laser imaging. The flow is illuminated with a pulsed Nd:YAG laser (Continuum Surelite II) and two Lambda Physik excimer lasers (LPX210).

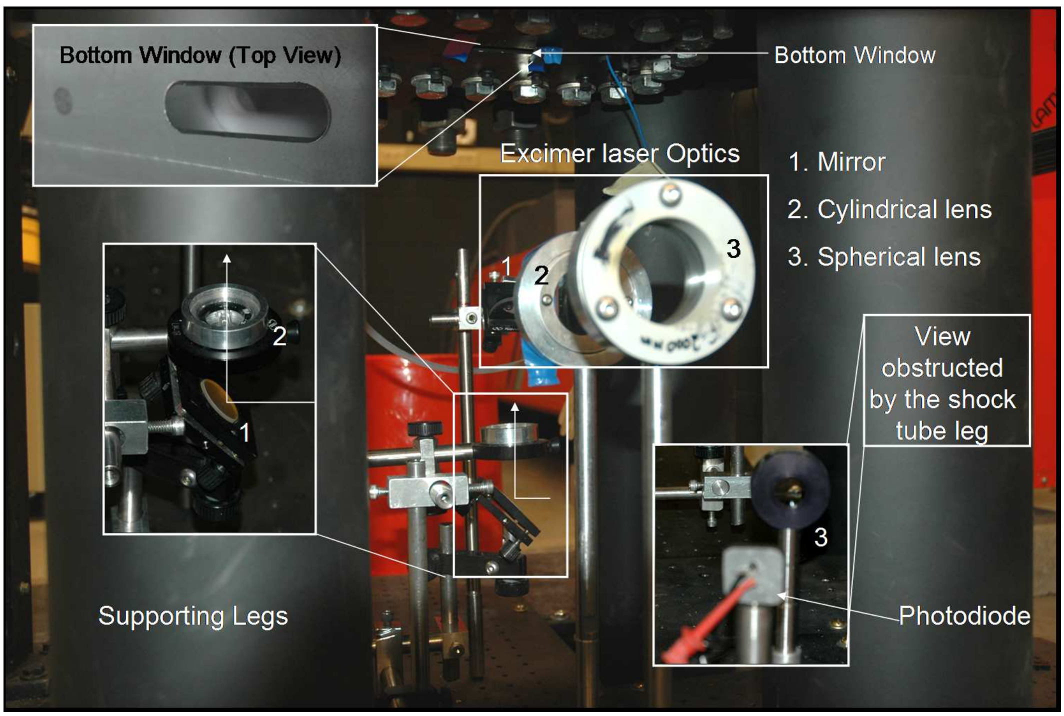

Figure 26: Photograph of the optic setup for the laser sheet imaging.

The Nd:YAG laser is capable of two pulses separated by a minimum of 100 ns with a pulse width of 10 ns duration. The wavelength of light generated by the Nd:YAG laser is 532 nm, while for excimer laser it is 248 nm (ultraviolet). Individual beams are steered into the driven section, using appropriate optics, through a 7.62 cm thick quartz window in the bottom of the shock tube. The beams are formed into sheets, using cylindrical lenses, before entering the driven section vertically through the end wall, and passing through the mid-plane of the bubble as shown in Fig. 26.

The imaging technique used here takes advantage of the atomization of the liquid bubble film as the incident shock wave passes through it. The size of the atomized droplets is dependent on the shock wave strength and the average droplet size is estimated to be on the order of 1 μm for a bubble accelerated by a M=2.88 shock [8, 56]. At lower Mach numbers, it may be noted that, because of the lower energy deposited by the shock on the bubble film, the atomization is less efficient, resulting in an average droplet size on the order of 30 μm for a bubble accelerated by a M=1.33 shock. A detailed description of the bubble breakup mechanism is included later in this chapter.

Three 1024×1024 pixel array Andor (model 434) CCD cameras are used to capture the Mie-scattered light resulting from the laser interaction with the atomized soap-film. Comparisons have been made with the images obtained by seeding the bubble gas with smoke in the case of a stationary bubble and the Mie-scattered signal from the soap film is much brighter compared to that from the smoke particles . The flow structures observed with and without seeding were similar, therefore, seeding of the bubble gas was concluded to be unnecessary in further experiments. This maintains the purity of the bubble gas and allows precise knowledge of the density ratio between the bubble and ambient gases. Two images are recorded on a single CCD frame in dual-exposure mode in the compression phase of the bubble. These two images are the Mie-scattering signal resulting from the interaction of the Nd:YAG laser pulses with the atomized soap film. For later times, a UV lens is used to focus the signal obtained from the interaction of the excimer laser and atomized soap film onto the CCD array.

Since it is required to know precisely the location of the laser sheet with respect to the bubble, a shadowgraph image is taken at a selected location, perpendicular to the

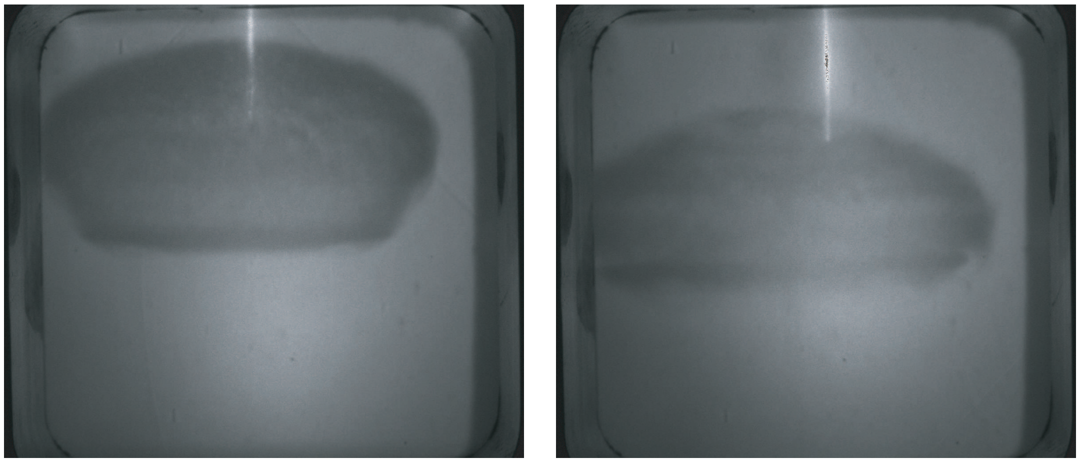

(*a*) (*b*)

Figure 27: Post-shock shadowgraph images of an argon-filled bubble accelerated by an $M = 1.4$ shock wave in N_2 indicate: (*a*) no bubble deviation from the tube's mid plane after departure from the injector, and (*b*) slight bubble deviation to left. The bright line in the images indicates the location of the laser sheet.

laser sheet using a collimated beam from a Xenon arc lamp. The image is captured using a LaVision (Flowmaster3) camera, providing one of the post shock images of the bubble in the compression phase as shown in Fig. 27. The viewing cross-section of this image port is only 0.08×0.08 m. We can only acquire images during the shock compression phase as the height of the bubble needs to be less than 0.08 m. The main purpose of the shadowgraph image is to confirm the location of the bubble relative to the plane of the laser sheet, since it is possible that the bubble's trajectory can cause it to deviate from the tube's mid-plane after departure from the injector. The bright vertical line in the center of the image indicates the location of the laser sheet. Figure 27(*b*) shows that the bubble has slightly deviated towards the left side of the shock tube. For 90% of the experiments performed, the bubble did not deviate a measurable amount from its trajectory. In summary, the optical system is designed to acquire five post shock images, including four using planar laser imaging and one using the shadowgraph technique. This allows for the study of the bubble distortion and development of the instability from a single experiment. Figure 28 shows a simple schematic overview of the experimental system used to study the shock wave interaction with a heavy bubble. In the case of the light bubble experiments, the retractable injector was inverted so that the bubble could rise freely once released from the injector without hitting the injector itself (see Fig. 29).

3.4 Initial Condition Characterization

Although the soap bubble is the simplest way of preparing an interface between two gases of different density, efforts were made to characterize every parameter in the initial condition which could have an effect on the flow field at late-times.

3.4.1 Bubble Film Thickness

In the case of the heavy bubble, the soap film is estimated to be 0.5 μm thick with a slight increase in thickness at the bottom of the bubble due to gravitational flow of the liquid soap film. This estimation is based on the wave nature of light [26, 46], as the brilliant colors observed in soap bubbles occur because of interference of light reflected from the outer and inner surfaces of the bubble. Therefore, at any stage during bubble formation, the thickness of the bubble is on the order of magnitude of the wavelength of visible light. In addition, there is a stage in the life of bubbles referred to as “black bubbles”. This occurs when the thickness of the bubble film is less than the wavelength of visible light, but still a coherent film. When that happens, the bubble seems to disappear, but its

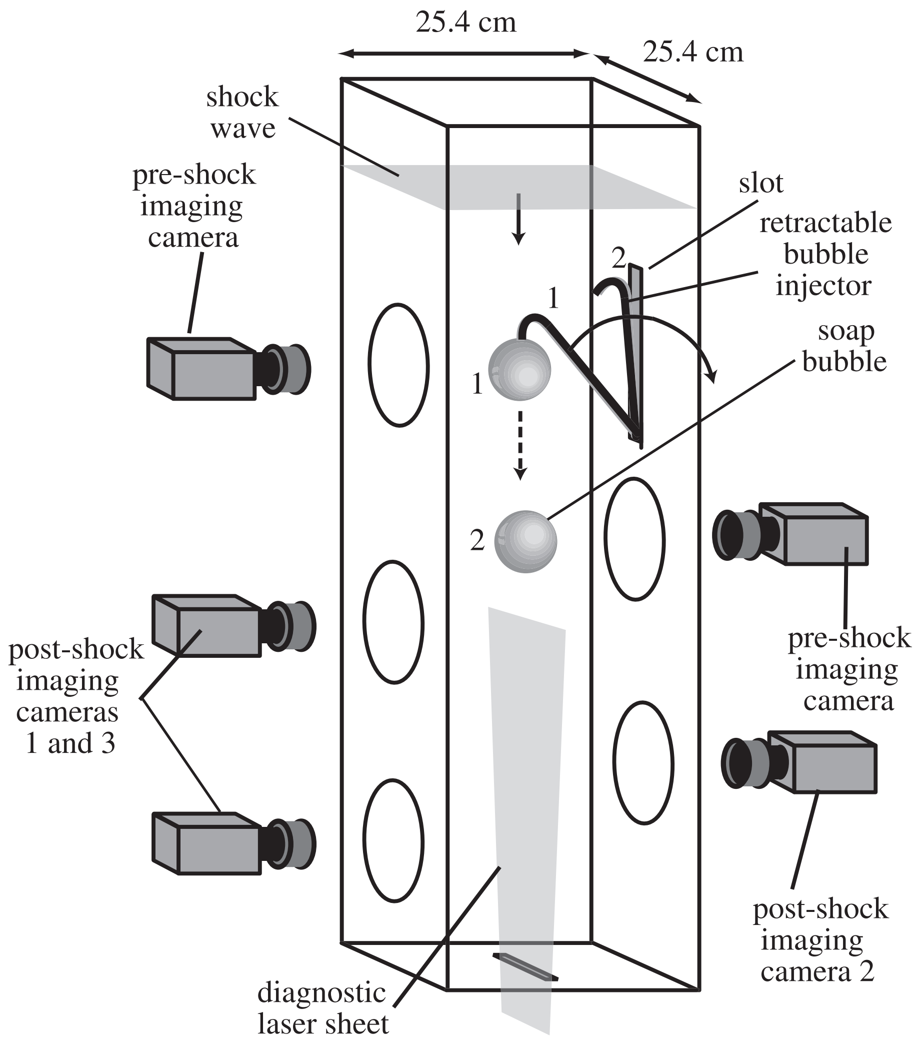

Figure 28: Schematic view of experimental setup (not drawn to scale), showing the configuration (1) before and (2) after retraction of the bubble injector for the heavy bubble scenario.

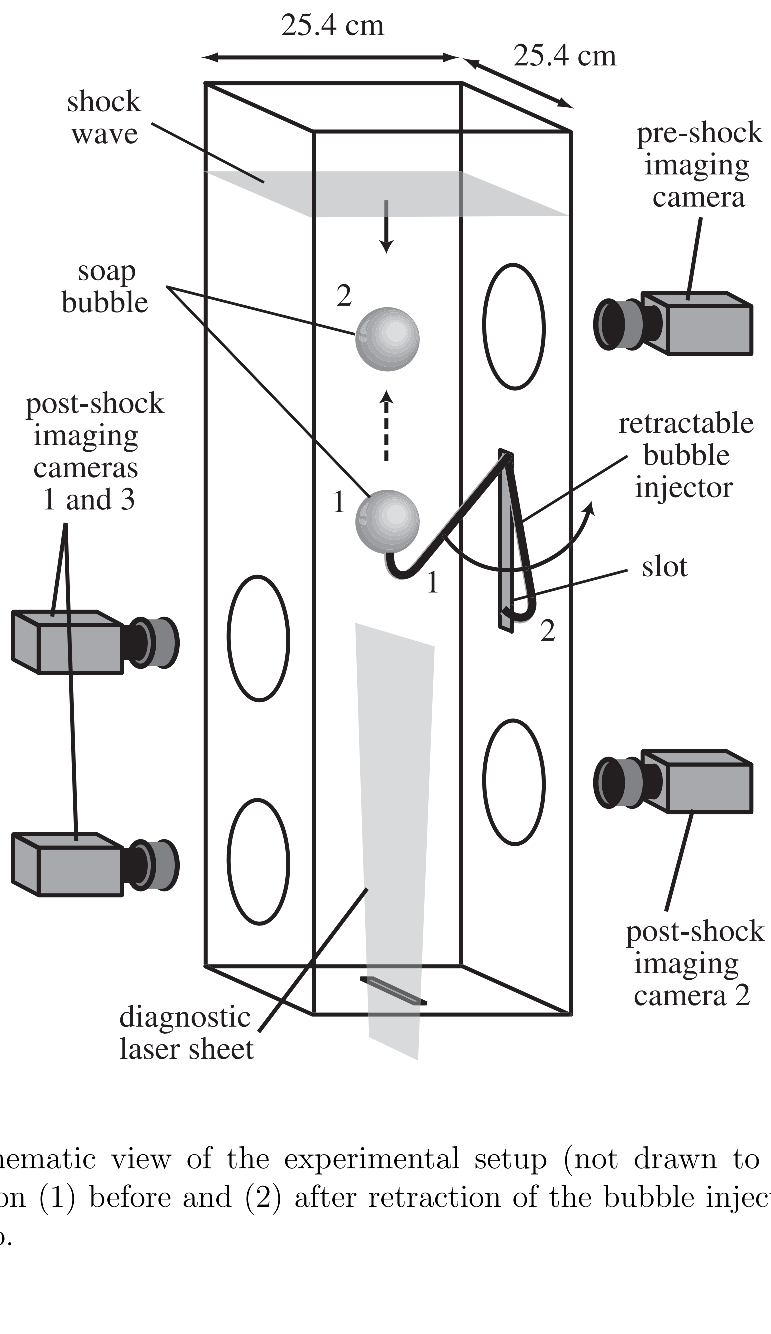

Figure 29: Schematic view of the experimental setup (not drawn to scale), showing the configuration (1) before and (2) after retraction of the bubble injector for the light bubble scenario.

existence is known because droplets can be observed when the bubble pops. Sometimes, during the bubble free fall, the upper hemisphere of the bubble appears to disappear; although one can clearly see the lower hemisphere of the bubble. This suggests that during the free fall or free rise, gravitational flow of the soap film leads to the thinning of the upper half of the bubble.

The film thickness was also estimated by carefully measuring the mass of a film. This was done using an isolated electronic balance (model ER-182 A). A 0.05 m diameter bubble was created and popped carefully on a filter paper. The mass of the filter paper was recorded before and after collecting the popped film. This process was carried out twenty times to obtain the average mass of the film. The average mass of the film, used to create a 0.05 m diameter bubble was found to be 9.0±0.4 milligrams. The density (ρ) of the film solution was measured to be 1013 kg/m^3. The film thickness (δ) was then calculated to be

$$\delta = \frac{m}{\pi D^2 \rho} \approx 1.0\ \mu\text{m}. \tag{3.1}$$

3.4.2 Flow Field Inside the Bubble

The velocity field inside the bubble, just before retraction, is an important parameter which can affect the growth of the bubble at late times. It is believed that residual circulatory motion inside the bubble can lead to the growth of small-scale features at late time. Figure 30 shows a sequence of images during the bubble blowing process and the bubble was seeded with smoke particles for flow visualization. The concentration of the smoke seeding particles was sufficient to obtain the velocity field inside the bubble by cross-correlation between two successive frames. Figure 31 shows the late time flow field inside the bubble after the bubble blowing process was completed. It can be noted

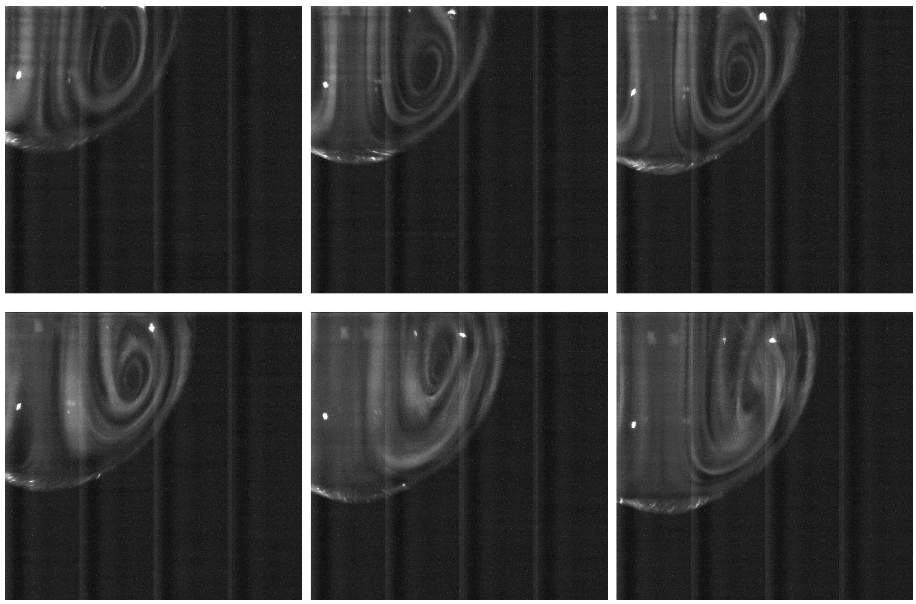

Figure 30: Sequence of images showing the flow field inside the bubble during the bubble blowing process.

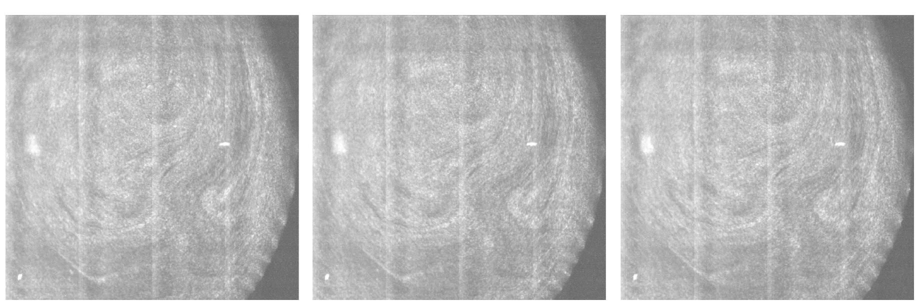

Figure 31: Sequence of images showing the flow field inside the bubble, thirty seconds after completion of the bubble blowing process

that there is a strong circulation during bubble blowing, but it clearly dies out as seen in Fig. 31.

Figure 32 shows the velocity field inside the bubble during and after the blowing process. The maximum velocity was seen on the vertical axis of the bubble during the blowing process and was measured to be 0.015 m/s. During a shock tube experiment, the bubble is left to sit on the injector for two to three minutes before retraction, wherein, the velocity field inside the bubble decays considerably, after completion of the blowing process. It is estimated that the maximum velocity inside the bubble was 0.005 m/s after completion of the blowing process. The particle speed behind the shock wave for a high Mach number experiment is on the order of 750 m/s and this suggests that the velocity field inside the bubble is insignificant compared to the post-shock velocity. The residual bubble-inflation flow only contributes perturbations with relative magnitudes on the order of 10^{-5} to the post velocity field. Therefore, for all the practical purposes, the velocity inside the bubble is assumed to be zero during interaction with the shock wave and the subsequent shock-induced distortion of the bubble.

3.4.3 Bubble Breakup Mechanism

It is very important to understand the bubble breakup mechanism after shock interaction. It is a common experience that the process of rupture is rapid and driven by surface tension; the energy released by the surface reduction is converted into kinetic energy, and partly dissipated. In 1990, Pandit and Davidson [50] reported on experiments studying the hydrodynamics of the rupture of thin liquids films. Since then, extensive experimental and theoretical work has been performed to understand this phenomenon. During the early stage of this dissertation, one of the experimental ideas was to rupture

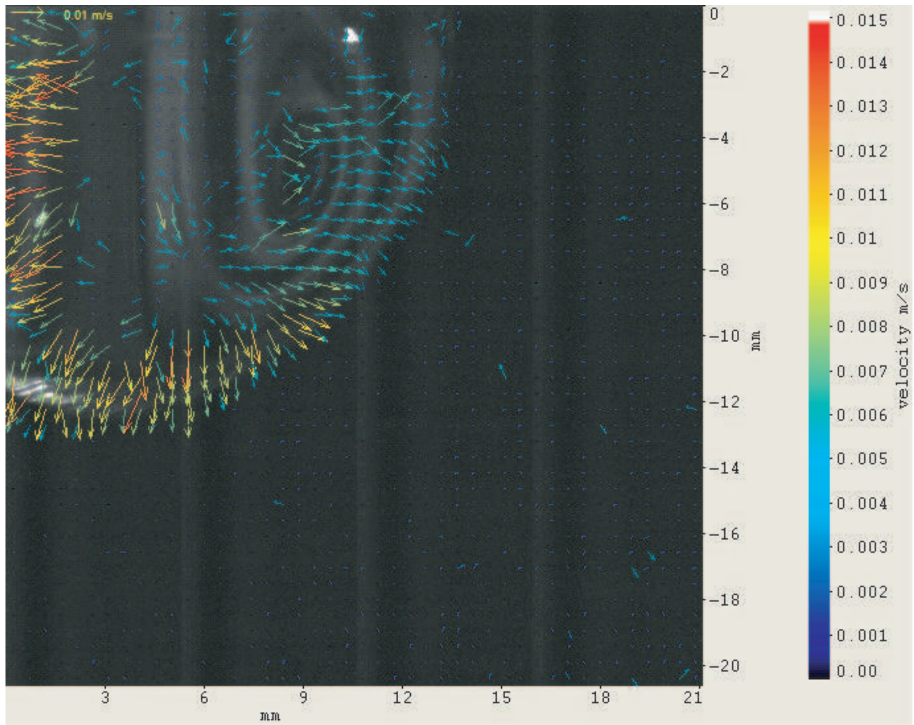

(*a*)

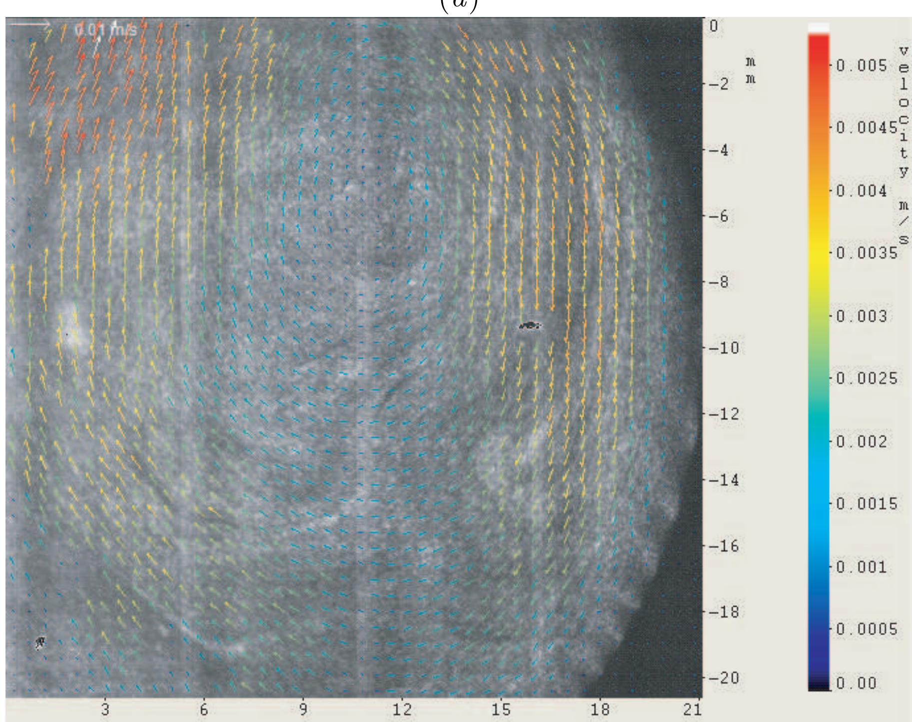

(*b*)

Figure 32: Velocity field inside the bubble: (*a*) during the bubble blowing process, (*b*) 30 seconds after completion of the bubble blowing process.

the soap film before the shock wave arrival which would have provided a filmless spherical three-dimensional continuous interface between two gases. To fully utilize this idea, one had to ensure that the interface was not distorted by the film rupture. To study the effect of the film rupture on the initial interface, careful experiments were performed by creating a helium bubble on a stainless steel pipe. Helium was doped with acetone to perform planar laser induced fluorescence (PLIF) visualization using a Lambda Physik excimer laser, emitting light at 248 nm wavelength. The rupture was initiated by passing a Nd:YAG laser beam through the bubble.

Figure 33 shows a sequence of images depicting the rupture of the bubble. The timing between consecutive frames is 1 ms. One can clearly see two circular holes grow in the bubble after 1 ms, and the circular "rupture rims" following a nearly spherical paths. The rim is subjected to the varicose instability, which leads to the shedding of the droplets from the rim in flight, and is clearly visible in the experimental images after 3 ms. Also, one can clearly see that the upper part of the left and right rims have merged by the end of 3 ms. At this point, small-scale features are evident on the continuous interface between helium and air. This led to the conclusion that the idea of breaking the film before the shock arrival to obtain a clean continuous three-dimensional interface was not feasible at this point. The moving rim velocity from the experiments was estimated to be on the order of 10 m/s. The last image shows that the circular rims have completely merged with each other, and the excess film material is collected at the bottom of the bubble. Also evident at this stage is development of small ligaments on the merged rim due to the varicose instability. This finally leads to the breakup of the rim into fine droplets. Rayleigh [65] calculated a limiting velocity of $v_{rim} = \sqrt{4\sigma/\rho\delta}$ from the surface tension (σ), the density (ρ) of the liquid, and the film thickness (δ),

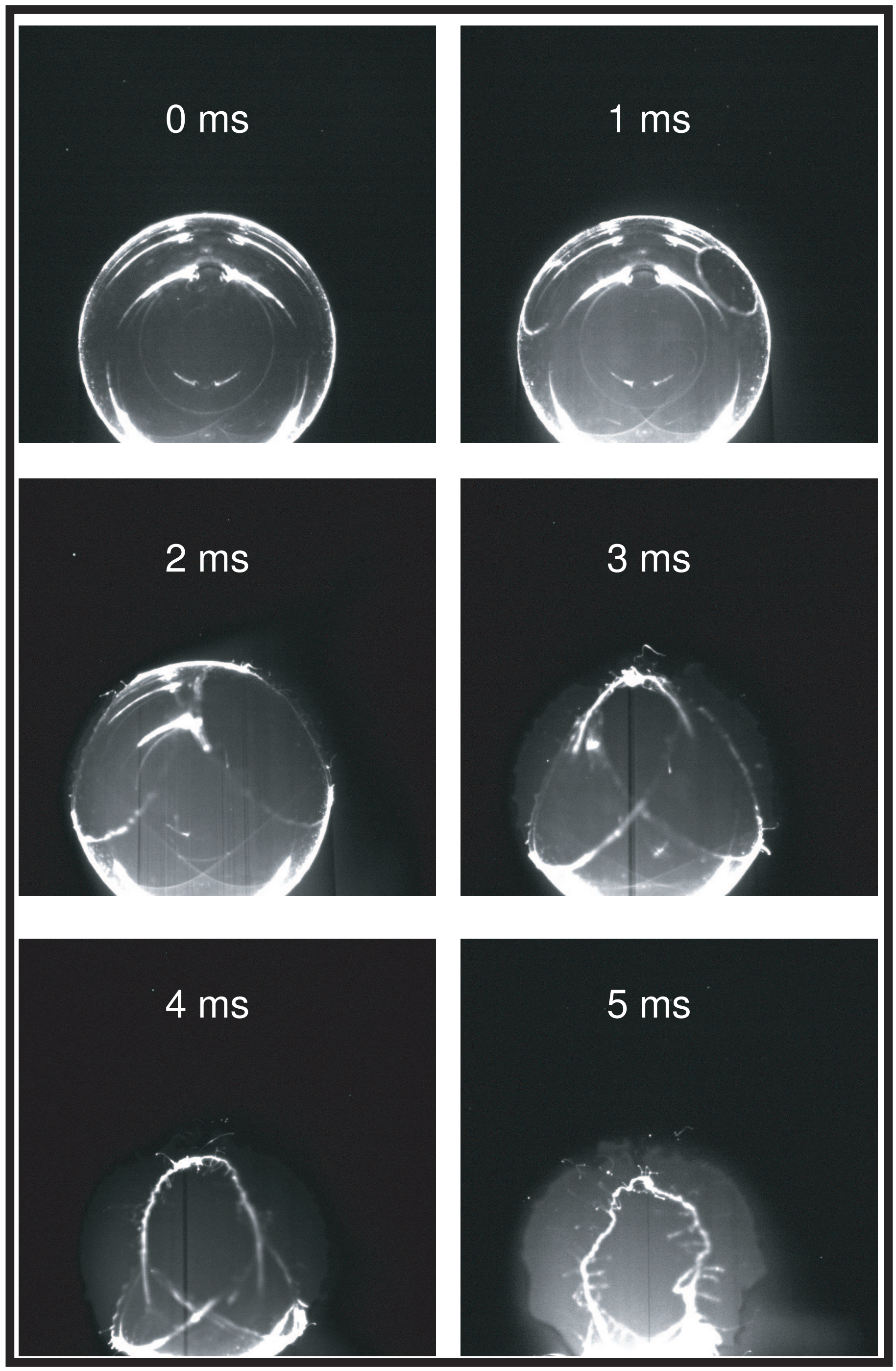

Figure 33: Sequence of images showing the bubble rupturing after being hit by a Nd:YAG laser beam. The times after puncture of the film are stated on the image frames.

under the assumption that all released surface energy is converted into kinetic energy. From the more general momentum balance, Cullick [11] and Taylor [68] derived the rim velocity to be $v_{rim} = \sqrt{2\sigma/\rho\delta}$ and independently retrieved a missing dissipation term in the model. This formulation is valid for the rim surrounding a hole in a spherical bubble case and is estimated to be:

$$v_{rim} = \sqrt{2\sigma/\rho\delta} = \sqrt{2 * 0.07281/1013 * 1e - 6} \approx 11.5 \text{ m/s.} \tag{3.2}$$

The breakdown of the bubble in the case of very low Mach number experiments is similar to the one shown in Fig. 33. The shock wave propagation leads to the growth of the circular holes, and such holes are clearly visible in the experimental image (Figure 9) of Haas and Sturtevant [21]. It has been postulated that these holes are probably triggered by the Rayleigh-Taylor instability induced by the transmitted shock wave. At low Mach number the v_{rim} is comparable to the particle speed behind the shock wave. As the shock strength is increased, more holes are created and consequently they grow to a smaller diameter before merging.

Figure 34 shows that, in the case of moderate Mach number experiments ($M \approx$2.0), the film looks immediately fragmented as a very dense patterns of holes are created. It is evident that, due to immediate atomization of the bubble film, no small-scale structures are visible on the bubble surface.

3.4.4 Drop Size Estimation

The size of the atomized film droplets after shock wave interaction is estimated here using the model proposed by R. Cohen [8]. This is a statistical model (based on energy and entropy principles), which describes the shattering of a single spherical liquid drop

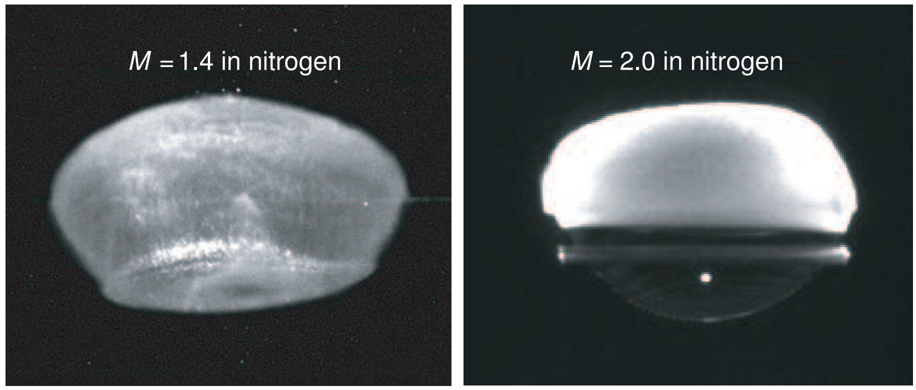

Figure 34: Experimental images indicating the immediate atomization of the bubble film after shock wave interaction. The atomization looks much more efficient for the high Mach number case.

after being subjected to a blast wave in air. The first step in our calculation is to approximate liquid film as lying within a solid sphere of equivalent mass. This is used to calculate the diameter of the equivalent spherical liquid drop D_{eq} as shown below:

$$m = \pi D^2 \rho \delta = \frac{\pi \rho D_{eq}^3}{6} \tag{3.3}$$

$$D_{eq} = \sqrt[3]{6D^2\delta}. \tag{3.4}$$

The second step is to calculate the energy of impact (E_T) transferred to the drop. This can be expressed as

$$E_T = \frac{1}{2}\rho_1 u_1'^2 \frac{1}{6}\pi D_{eq}^3, \tag{3.5}$$

where u_1' is the particle speed of the carrier gas. The Sauter mean diameter, D_{32}, of the atomized particles can be calculated from the following relation

$$\frac{D_{32}}{D_{eq}} = 1.78\widehat{E_T}^{-0.946}, \tag{3.6}$$

where the dimensionless impact energy, $\widehat{E_T}$, is defined as

$$\widehat{E_T} = \frac{E_T}{\sigma \pi D_{eq}^2}. \tag{3.7}$$

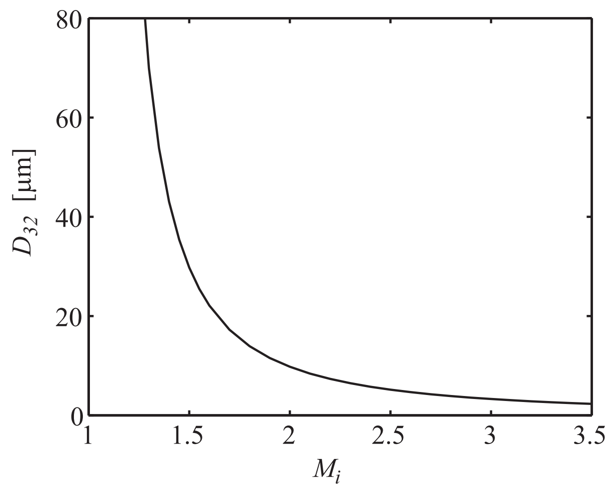

Figure 35: Sauter mean diameter of spherical droplets produced in shock wave atomization of a spherical drop having the same mass as the experimental film layer, plotted against the Mach number of the incident shock wave.

The droplet diameter in this theory has an inverse dependence on the shock wave strength, as shown in Fig. 35. The average droplet size is estimated to be on the order of 1 μm, for a bubble accelerated by a M=2.88 shock wave. At lower Mach numbers, it may be noted that, because of the lower energy deposited by the shock on the bubble film, the atomization is less efficient. The average droplet size is estimated to be on the order of 30 μm, for a bubble accelerated by a M=1.5 shock wave.

3.5 Experimental Procedure

This section describes the sequence of events in the experiment studying the interaction of an $M \approx 2.03$ shock wave in nitrogen with a heavy bubble filled with argon in free fall. Before an experiment is conducted we construct a wave diagram (x-t plot) using the one-dimensional gas dynamics approach [1], and then study the feasibility of the

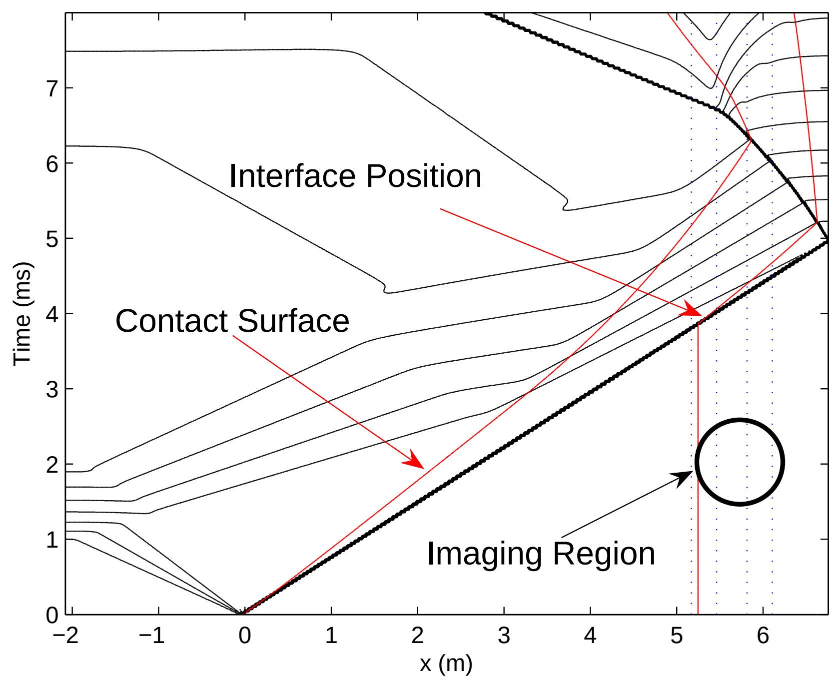

Figure 36: Wave diagram for a $M = 2.03$ shock wave in nitrogen.

experiment. Figure 36 shows a wave diagram for a $M = 2.03$ shock wave in a driven section filled with nitrogen. Since the bubble occupies a very small region of the shock tube driven section, we neglect its presence while constructing the wave diagram. In the wave diagram, the red line on the left denotes the contact surface while one on the right denotes the interface (the location of top of the bubble) which travels at the particle velocity. Note that we are interested in studying a singly shocked bubble at this time. The wave diagram shows that we can study this phenomenon during the time range $3.8 < t < 4.5$ ms. The shocked bubble is unaffected by the driver rarefaction and the reflected shock wave during this range. The sequence of events in the experiment is stated below.

1) A metal diaphragm is chosen which has a rupture pressure corresponding to the pressure needed for the required shock strength. Then, the metal diaphragm is placed between the driver and diaphragm section. The two sections are bolted together using all the twenty-four bolts.

2) All imaging windows are cleaned and bolted to the shock tube. The tip of the bubble injector is also cleaned at this time. Pressure transducer settings are verified at this point.

3) The delay times for laser pulses are calculated from the one-dimensional gas dynamics results, and the experimental history correlating the size of the bubble to the free-flow time. The delay times are then preset in the experiment control program.

4) The driver and driven sections are evacuated to 4800 Pa. The driver section is then pressurized to 95% of the diaphragm rupture pressure with nitrogen. The driven section is filled with nitrogen to atmospheric pressure and the two boost tanks are filled with helium to 10 MPa.

5) Pre-shock background images are acquired with and without laser pulses.

6) A soap bubble is created with the stainless steel injector system by first displacing any nitrogen in the injector with argon, then placing a layer of soap film on the tip of the bubble injector, and finally, using a pneumatic cylinder of prescribed volume to blow an argon bubble, approximately 5 cm in diameter.

7) The bubble is released from the injector by fast retraction of the injector into

the slot located in the shock tube wall. After a delay of 250-350 ms, a downward-moving shock wave impacts the bubble, having been released by discharging the boost tanks, through fast-opening solenoid valves. The retraction process, fast-opening solenoid valve, and the cameras are triggered by computer control program based on the LabView software. Generally, the camera shutters remain open for the entire process.

8) The retraction and free fall of the bubble is imaged with a fast framing camera using front white lighting.

9) When the shock wave passes by a predetermined pressure transducer, the data acquisition system is triggered, which records the pressure data, and also triggers the laser pulses for imaging of the shocked-bubble flow field.

10) The acquired images are then saved and the pressure transducer data shown in Fig. 37, are used to calculate the actual shock wave speed.

11) The initial location of the bubble just prior to shock wave interaction is noted and it is used in conjunction with the measured shock wave speed to obtain the age of the shocked bubble.

3.6 Experimental Study Scenarios

Eleven scenarios are considered, covering the Atwood and Mach number ranges $-0.8 < A < 0.7$ and $1.3 < M < 3.5$. The experimental scenario is designed to facilitate the objectives stated in Chapter 1. In this study, the previous works of Haas and

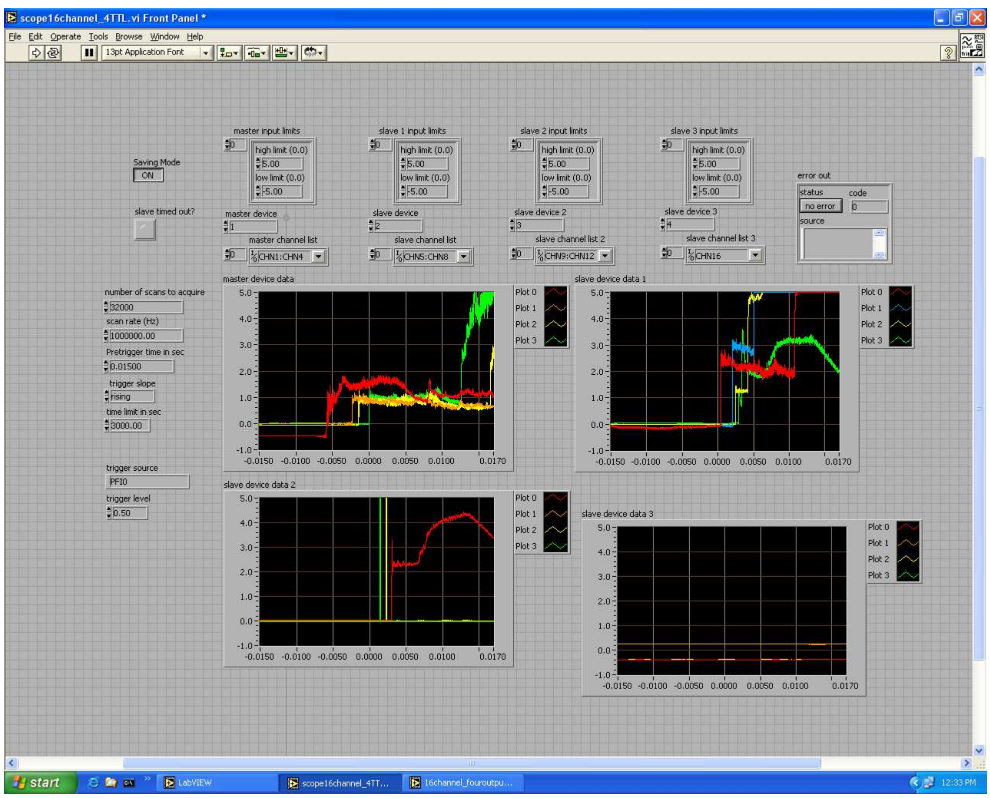

Figure 37: Pressure transducer traces acquired during the experiment.

Sturtevant [21] and Layes *et al.* [35, 36] are extended to higher Mach numbers. An overview of the experimental scenario is included as Table 1.

Scenario #	Bubble gas	Ambient gas	M	A	u'_1/c'_1	Injector system
1	Helium	Air	1.45	-0.757	0.515	Free Rise
2	Helium	Air	2.08	-0.757	**1.007**	Free Rise
3	Helium	Nitrogen	2.95	-0.750	**1.346**	Free Rise
4	Air	Argon	2.13	-0.160	0.828	Stationary
5	Argon	Nitrogen	1.33	0.176	0.438	Free Fall
6	Argon	Nitrogen	2.03	0.176	**0.980**	Free Fall
7	Argon	Nitrogen	2.88	0.176	**1.326**	Free Fall
8	Argon	Nitrogen	3.38	0.176	**1.449**	Free Fall
9	Freon 22	Nitrogen	2.03	0.516	**0.980**	Free Fall
10	SF_6	Nitrogen	2.07	0.681	**1.002**	Free Fall
11	SF_6	Nitrogen	3.00	0.681	**1.359**	Free Fall

Table 1: Experimental study overview. M is the Mach number of the incident shock wave; A is the pre-shock Atwood number at the bubble surface. u'_1 and c'_1 represent the flow speed and the sound speed, respectively, of the shocked ambient gas.

3.7 Numerical Simulation

Several of the experimental configurations described above were simulated numerically in three-dimensions by John Niederhaus using an adaptive-mesh refinement, Eulerian hydrodynamics code called *Raptor*. The results are included in this dissertation for comparison purposes, as well as to understand the evolving vorticity dynamics and subsequent turbulent mixing. A detailed description of the numerical method and problem setup has been reported by John Niederhaus in his doctoral thesis [47] and a very brief description is included here.

Calculations for the shock-bubble interaction using *Raptor* are set up on a Cartesian mesh subtending a quadrant of a typical shock tube flow field, including a quarter-spherical bubble of radius $R = 2.54$ cm. A coordinate system is defined whose y-axis is coincident with the shock tube long axis, with physical dimensions $12.7\times84.7\times12.7$ cm, and a base grid of $42\times280\times42$ cells. Two levels of AMR are applied in the region surrounding the bubble, with a refinement ratio of 4 each yielding a resolution of 134 cells for the bubble radius. The mesh is updated dynamically during the simulation, maintaining all regions with nonzero bubble-fluid volume fraction, and regions in the immediate neighborhood, at the highest level of spatial resolution. Symmetry conditions are applied on the transverse boundaries to enforce quarter-symmetry and allow wave reflections at the shock tube side walls. Inflow/outflow conditions are applied on the axial boundaries to maintain constant driving pressure and allow waves to exit the domain smoothly (no endwall is included).

In the initial condition, a planar shock wave with a specified density, velocity, and pressure jump approaches the bubble. The shock moves in the $+y$-direction, and the bubble is centered on the y-axis. The interface at the surface of the bubble is created carefully in the initialization process by using a subgrid volume-of-fluid model to suppress "stairstep" density features associated with realizing a curved interface in a Cartesian mesh. The development of the flowfield is tracked at closely-spaced time intervals during and after the impact of the shock on the bubble. In the case of an argon bubble, a third fluid is added to the simulation to represent the thin liquid film layer enclosing the bubble. However, this fluid is placed in a one-cell-thick layer (on the finest AMR level), rather than in a layer representing the true film thickness, which is unresolvable here. Therefore, this fluid is given a corresponding reduced density, so that the correct total mass of the bubble film is present in the simulation. As an additional step in modeling the film, excess material is added on the lower extremity of the bubble, on both the inner and the outer surfaces. This excess mass represents tiny exterior droplets (on the order of $D/25$ in size) that form as a result of the technique used to produce the bubble and quickly release it in the shock tube. This excess mass was observed in the experiments for the argon bubble scenario.

Chapter 4

Visualization Results

A series of snapshots showing the bubble development during and after interaction with a shock wave is presented in this chapter. The experimental images illustrate the primary and secondary flow features induced by shock interaction. It is shown that the bubble distortion is completely different for the light bubble compared to the heavy bubble. Also, Mach number effects are investigated for the heavy (convergent-geometry) and light (divergent-geometry) bubble cases.

4.1 Divergent-Geometry: Mach Number Effects

Visualizations of shock-bubble-interaction flow fields from both simulations and experiments are shown in Figs. 38-40 for a shocked helium bubble in air or nitrogen. Experimental images show Mie-scattered light from the midplane of the shocked bubble, as described in Sec. 3.3.2. Numerical images show a slice through the dataset at an angle of $\theta = \pi/6$ to the $x = 0$ plane. The total density field is plotted, with an overlaid contour indicating the isosurface of the helium volume fraction, $f = 10^{-6}$; the vorticity magnitude field $\boldsymbol{\omega} = |\nabla \times \mathbf{U}|$ is plotted alongside the density field as a reflection about the y-axis. The transverse width of the field of view is 8 cm in the experimental and numerical images, and shock wave motion is downward. The time is non-dimensionalized as $\tau = t/t'$. The characteristic time $t' = D/(2W_t)$, is defined as the cloud crushing time, where D is the initial diameter of the bubble and W_t is the velocity of the shock wave transmitted in the bubble. The value of W_t is computed from the one-dimensional gasdynamics of a shock wave-slab interface interaction based on the value of incident shock wave speed (W_i) measured from pressure transducer data.

4.1.1 Helium bubble in air, M=1.45

Visualizations of shock-bubble interaction flow fields for $M = 1.45$ are shown in Fig. 38. At this relatively low Mach number, atomization of the soap film layer by the shock wave is poor. Therefore, the soap film particles in the post-shock flow are larger and have greater inertia than at higher Mach numbers. These larger particles are not as easily entrained into the helium bubble fluid during shock passage, but appear to remain on the interface. This can be seen clearly in Fig. 38(*a*-*b*), where the compressed bubble is outlined by soap film material. Further, as time progresses, a cloud of large soap film particles is left behind the shocked bubble due to their larger inertia. Such a cloud is seen in Fig. 38(*d*-*f*), and can be perceived also in the experimental shadowgraph images of Haas and Sturtevant [21] and Layes *et al.* [35]. This cloud provides a strong Mie scattering source in the present experiments, and a significant absorption region for shadowgraphy diagnostics. However, it is not a feature of the shock-bubble interaction itself, and is therefore not included in measurements of the streamwise and lateral length scales of the shocked bubble.

Disregarding the distribution of soap film material, which is not included in the numerical simulations, we observe that the patterns of deformation undergone by the bubble in the simulations strongly resemble those seen in experiments. The bubble is initially compressed axially during the transit of the initial shock wave, seen in Fig. 38(*a*).

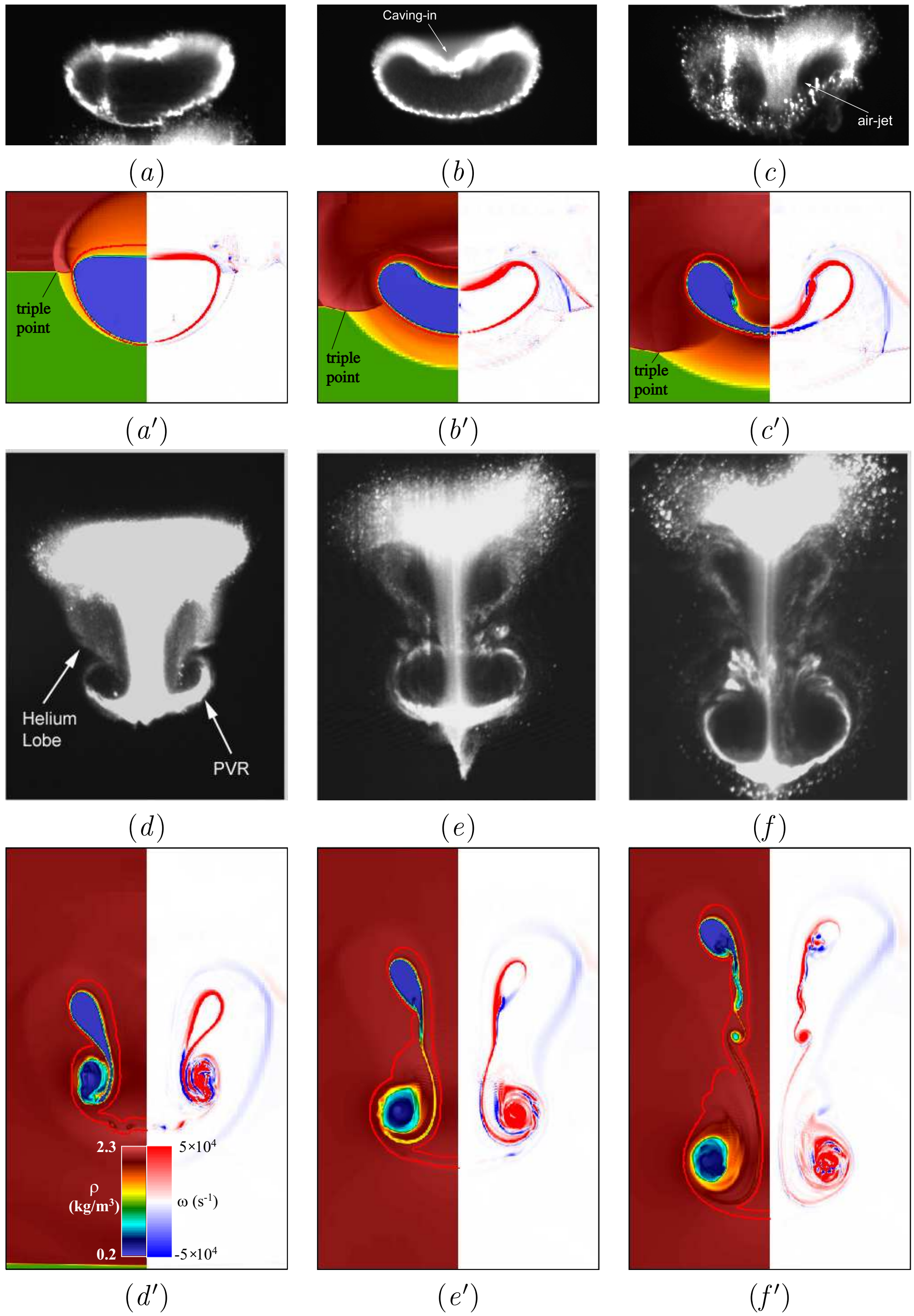

Figure 38: Flowfield evolution of a He bubble in air, $M = 1.45$. Numerical images show the total density on the left with the isosurface of $f = 10^{-6}$ plotted in red, and vorticity magnitude on the right. Dimensionless times τ are (a) 2.4, (a') 2.4, (b) 2.5, (b') 4.8, (c) 11.5, (c') 7.7, (d) 21.6, (d') 21.8, (e) 38.7, (e') 38.9, (f) 57.9, (f') 57.9. The width of the field of view in each image is 8 cm. The characteristic time is $t' \approx 15.3$ μs, for a bubble initially of diameter 3.81 cm.

Vorticity generated by the baroclinic mechanism of Eqs. 2.11-2.12 causes the upstream surface of the bubble to deform and "cave in" toward the downstream surface [57], as seen in Fig. 38(*b*-*c*). The caving-in portion of the upstream surface impinges on the downstream surface, and vorticity generated during shock passage rolls up and draws the bubble fluid into a characteristic primary vortex ring, as seen at the downstream end of the bubble in Fig. 38(*d*). This "caving-in" or inversion process is a well-known feature of divergent-geometry shock-bubble interactions, as observed in Refs. [21], [35], and [57]. This caving in is analogous to the phase reversal observed in a single-mode RMI experiment with the heavy gas above the light.

Meanwhile, some of the bubble fluid departs from the primary vortex ring and forms a large trailing annular lobe of helium, which carries half or more of the bubble fluid volume. The separation between the downstream and upstream volumes is first seen in Fig. 38(*d*), where the upstream lobe is visible as a tear-shaped body between the primary vortex ring and the bright cloud of soap film particles. In Fig. 38(*e*-*f*), this trailing lobe continues to separate from the primary vortex ring, and the deforming bubble thus elongates axially. Simulations show that this lobe is composed of pure, unmixed helium, and although a faint shear layer is visible surrounding it in Fig. 38(f'), the vorticity magnitude is insufficient for the layer to cause the lobe to form a vortex ring. Figure 38(*d*-*f*) illustrates the mass transfer from the helium lobe to the primary vortex ring, and during this period, the primary vortex ring grows in size while the trailing helium lobe continues to shrink.

One curious feature seen at late times ($\tau = 38.7$) in Fig. 38(*e*) is a strong downstream-oriented axial jet at the head of the shocked bubble. This feature is not seen in simulations, and is explained as an artifact of the soap-particle-based flow visualization technique. When the upstream portion of the bubble surface impinges on the downstream surface, strong induced velocities associated with the primary vortex ring draw the impinging fluid into the vortex core. However, the film particles, due to their larger inertia, continue their axial motion and subsequently run ahead of the primary vortex ring. A jet of film material preceding the head of the shocked bubble is also seen in the experimental images of Layes *et al.* [35] for air-helium shock-bubble interactions at $M = 1.25$. This effect is absent at high Mach numbers due to more effective atomization of the soap film layer.

4.1.2 Helium bubble in air, M=2.08

Experimental and numerical visualizations of air-helium shock-bubble interaction flow fields for $M = 2.08$ are shown in Fig. 39. Here we see that, due to the higher Mach number, the size of the atomized film particles has decreased, and the particles are more effectively swept into the helium bubble fluid by the shock wave and the associated post-shock velocity field. Thus, the flow diagnostic of the bubble fluid improves as the Mach number increases.

In the $M = 2.08$ experiments and simulations, we again see the same processes of shock-induced compression, primary vortex ring formation, and axial elongation as observed at $M = 1.45$. The bubble is compressed during the transit of the initial shock wave, as seen in Fig. 39(a-a'), and the inversion of the upstream surface is observed also in Fig. 39(b-b'). At later times, for $M = 2.08$, however, we see the development of well-defined vortical features at the upstream extremity, which are not seen at $M = 1.45$. In Fig. 39(c') the slip surface surrounding the trailing upstream lobe has rolled up into a vortex ring, rotating in the opposite direction to the primary vortex ring, and

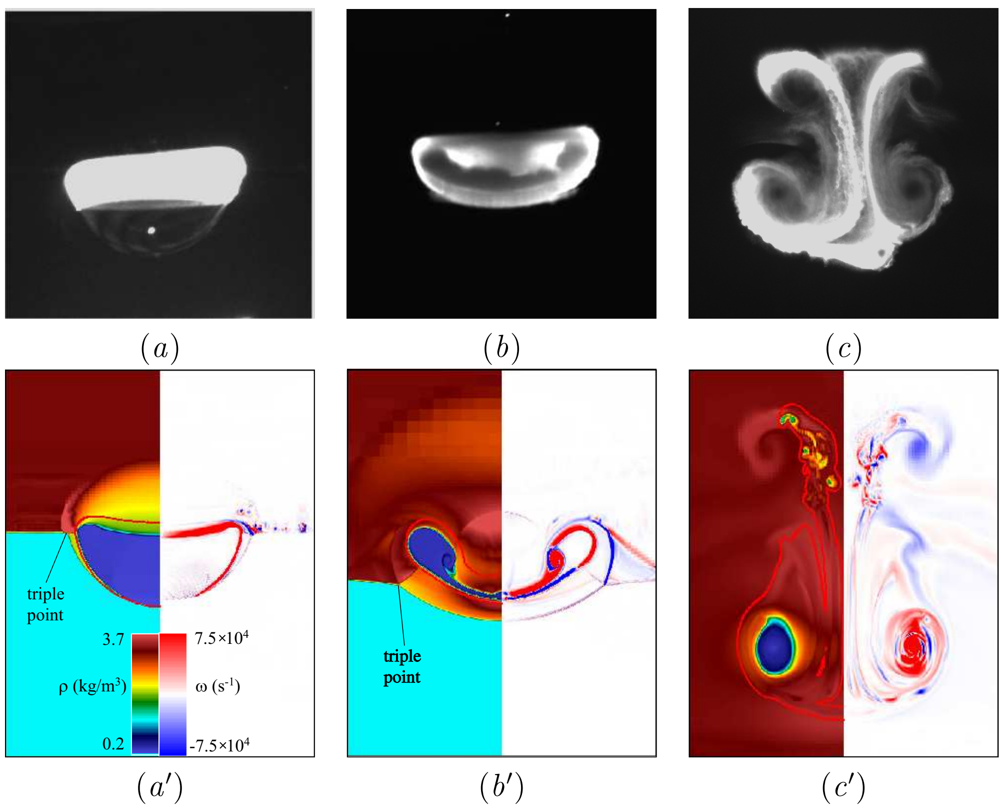

Figure 39: Flowfield evolution of He bubble in air, $M = 2.08$. Numerical images show (on the left) the total density with the isosurface of $f = 10^{-6}$ plotted in red, and (on the right) vorticity magnitude. Dimensionless times τ are (a) 2.0, (a') 2.2, (b) 6.6, (b') 5.8, (c) 41.7, (c') 37.9. The width of the field of view in each image is 8 cm. The characteristic time is $t' \approx 12.3$ μs, for a bubble initially of diameter 3.81 cm.

will be referred to as the secondary vortex ring. A similar, counter-rotating feature is apparent in the experimental image in Fig. 39(c). The mechanism for the development of this feature is discussed in detail in the description of the $M = 2.95$ experiments (Sec. 4.1.3). It is also apparent that the volume of bubble fluid carried by the trailing lobes dramatically decreases as the Mach number increases. For $M = 2.08$, most of the helium bubble fluid is entrained in the primary vortex ring, rather than the trailing lobe.

Finally, another notable difference between the $M = 1.45$ and $M = 2.08$ evolution is the appearance of a small region of complex, disordered motion in the near-axis area just downstream from the location of the secondary vortex ring in Fig. 39(c'), which is not found at the lower Mach number. Small-scale vortical fluctuations appear, as well as regions where the two fluids are strongly intermingled. These features do not appear in two-dimensional simulations, and are the manifestation of three-dimensional vorticity transport modes (vortex stretching) that are absent in two-dimensional vorticity dynamics, and grow here because of the strong shear and vorticity introduced at high Mach numbers.

4.1.3 Helium bubble in nitrogen, M=2.95

Experimental and numerical visualizations of He-N_2 shock-bubble interaction flow fields for $M = 2.95$ are shown in Fig. 40. In this high-Mach-number scenario, the size of atomized film particles in the post-shock flow is very small, which allows them to follow the flow much more closely. The decreased inertia of the soap film particles makes it possible to visualize the shock-bubble interaction flow field without the interference of a cloud of poorly-atomized film material in the upstream region.

In Fig. 40, several features of the flow field are observed to be noticeably altered from

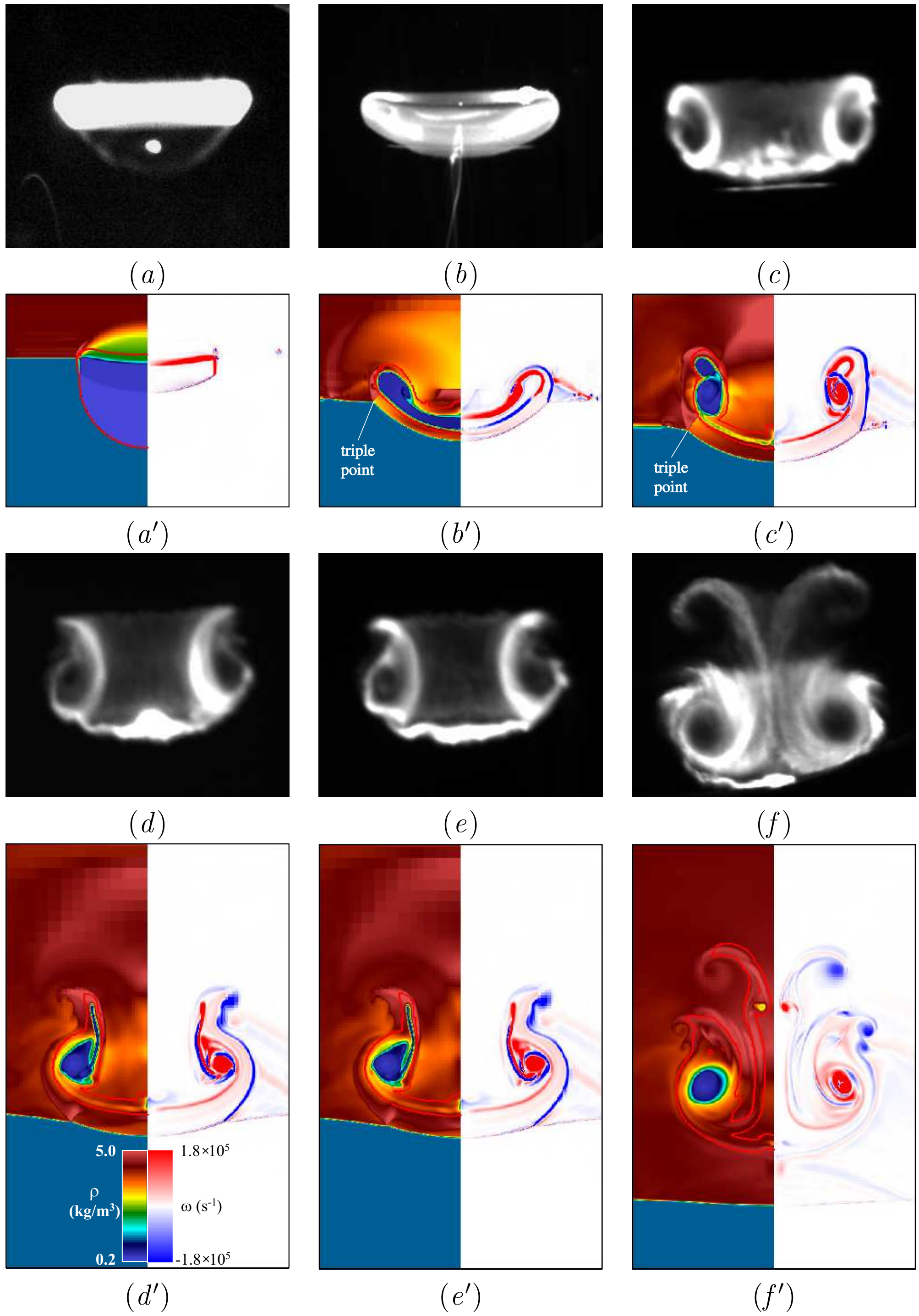

Figure 40: Flow field evolution of He bubble in N_2, $M = 2.95$. Numerical images show (on the left) the total density with the isosurface of $f = 10^{-6}$ plotted in red, and (on the right) vorticity magnitude. Dimensionless times τ are (a) 1.3, (a') 1.3, (b) 4.0, (b') 4.1, (c) 7.7, (c') 7.7, (d) 11.4, (d') 11.5, (e) 11.6, (e') 11.8, (f) 23.8, (f') 23.6. The width of the field of view in each image is 8 cm. The characteristic time is $t' \approx 9.7$ μs, for a bubble initially of diameter 3.81 cm.

the lower-Mach-number scenarios. The axial compression of the bubble during the initial shock wave transit is visibly stronger, as observed in both experiments and simulations, and is as expected from the Rankine-Hugoniot conditions. Further, a distinct primary vortex ring forms very quickly, visible as a well-defined circular feature at $\tau = 7.7$ in Fig. 40(c). The size of the trailing lobe is also much smaller, to the point that only faint wisps remain upstream of the primary vortex ring in Fig. 40(f), with the Mie-scattered signal in Fig. 40(f) being dominated by the region of the primary vortex ring.

Several peculiar features are also visible in these images. First, in Fig. 40(a), we note the bright horizontal discontinuity visible near the equator of the shocked bubble. This feature is the front of atomized soap film particles under the acceleration of the transmitted shock wave. Since these particles have a small but finite acceleration time, they can be assumed to lag slightly behind the shock wave, and therefore do not exhibit the concave curvature of the transmitted shock wave itself. This behavior is also seen at $M = 2.08$, in Fig. 39(a). Another noticeable feature is the appearance of multiple-scattering effects, due to the strength of the Mie-scattered signal generated in the plane of the laser sheet, soap film particles entrained in regions of the bubble that lie outside the plane of the laser sheet are also visible via secondary scattering events. This is responsible for the dim regions visible between opposing vortex cores in Fig. 40(c-e).

Even more noticeable is the fact that by $\tau = 23.8$, the development of a secondary vortex ring is already nearly complete. This can be seen in the rotational motion evident on the trailing wisps in Fig. 40(f), and in the numerical vorticity plots in Fig. 40(e'-f'). As in the $M = 2.08$ case, this vortex ring has opposite sense of rotation compared to that associated with the primary vortex ring. Most of the helium bubble fluid is entrained in the primary vortex ring, but induced velocities associated with the secondary vortex ring cause traces of helium to be drawn into the upstream region at late times.

In general, we observe remarkable agreement between experimental and numerical flow visualizations shown in Fig. 40. The simulations capture both the bulk features of the shocked bubble, including its dimensions and the configuration of vortex rings, as well as many of the more subtle, small-scale features of the flow, including the spacing and relative sizes of the vortex cores and the development of the upstream trailing strands of bubble fluid. The experimental images exhibit a very strong Mie-scattering signal from well-entrained soap film particles, and no individual particles are visible in the images. (This is in contrast to the lower-M cases, where we would expect a much clearer flow visualization if smaller scattering particles could be generated.) Most notable in both experiments and simulations, is the development of a distinct primary vortex ring, which is the dominant feature of both the observed and simulated flow field, and shows no sign of deterioration for the temporal regimes shown in Fig. 40.

4.1.4 Helium bubble in air or nitrogen at late post-shock times

The behavior at later times for all three Mach numbers is depicted in a fourth set of experimental and numerical flow visualizations shown in Fig. 41. The numerical images in Fig. 41 show the helium volume fraction field (f), rather than the total density, plotted on a logarithmic scale. In this way, the distribution of the bubble fluid even at small concentrations can be observed more clearly. Further, in order to facilitate comparison with experimental images, the grey scale for the volume fraction plots is peaked at $f = 10^{-4}$, with the maximum and minimum values of f colored black. In this way, regions of pure helium in the vortex cores appear black, as they do in experiments, due to centrifugal ejection of soap film particles from these vortices.

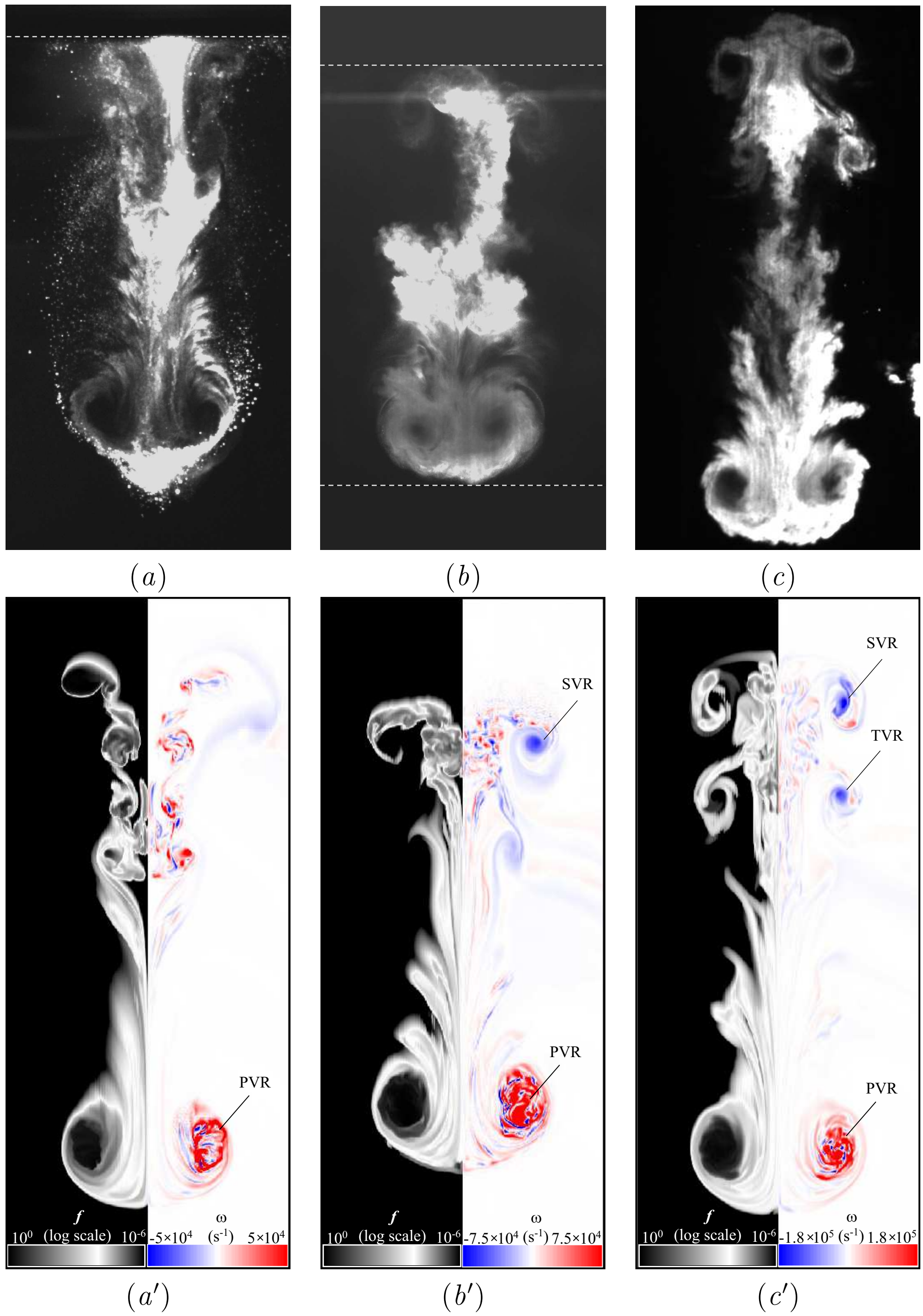

Figure 41: Late-time flow field visualizations of He bubble in air or N_2. Numerical images show (on the left) the helium volume fraction f on a logarithmic gray scale peaked at $f = 10^{-4}$, and (on the right) vorticity magnitude ω. Dimensionless times τ are (a) 105.8, (a') 105.8, (b) 63.4, (b') 63.5, (c) 69.5, (c') 63.5. The characteristic times and Mach numbers (for a bubble of initial diameter 3.81 cm) are $(a - a')t' \approx 15.3$ μs, $M = 1.45$ $(b - b')t' \approx 12.3$ μs, $M = 2.08$ $(c - c')t' \approx 9.7$ μs, $M = 2.95$. The width of the field of view in each image is 8 cm. White dashed lines denote cropping locations for experimental images.

The late-time images in Fig. 41 illustrate the strength and duration of vortical motion in divergent-geometry shock-bubble interactions. In the $M = 1.45$ case, the experimental and numerical flow fields are shown at dimensionless time $\tau = 105.8$, and yet the primary vortex ring remains very well-defined and apparently stable. The visualizations for $M = 2.08$ and 2.95 are shown for much earlier times, $\tau \approx 65$, and in these cases as well, the downstream region of the flow field is dominated by the well-defined primary vortex ring (PVR), which persists as a stable feature of the flow to very late times. In all three cases, the strong axial elongation of the shocked bubble is also clearly evident, which is due to the divergence of the primary vortex ring from either the trailing lobe or the secondary vortex ring. (The elongation has proceeded farther in the low-M case shown in Fig. 41(a) because of the later time.)

For $M = 2.08$ in Fig. 41(b), a secondary vortex ring can be seen at the upstream end of the bubble. At $M = 2.95$, in Fig. 41(c), a stable, well-defined secondary vortex ring (SVR) is visible, as well as a tertiary vortex ring (TVR) which appears at late times just downstream from the SVR. The induced velocities associated with the SVR are so strong that the upstream and downstream portions of the shocked bubble visibly begin to separate from each other in Fig. 41(c). The SVR in both of these cases can be seen to have the opposite sense of rotation to the PVR, however, no SVR of this type appears in the $M = 1.45$ scenario, even at $\tau = 105.8$. The only additional vortex formation that occurs in the $M = 1.45$ scenario is the development of small-scale vortices co-rotating with the primary vortex ring on the long neck between the PVR and the trailing lobe, seen in Fig. 41(a-a').

The origin of the secondary and tertiary vortex rings is in the slip line traced in the flow field around the bubble by the triple point that develops as a result of irregular shock refraction. In Figs. 38(b'-c'), 39(b'), and 40(b'-c'), a triple point is visible in the density field where the re-transmitted shock wave, Mach stem, and incident shock wave all meet. As the shock wave returns to planarity, this point moves circumferentially around the surface of the shocked bubble, just outside the interface. A contact surface develops at the boundary between (1) fluid that has interacted with the re-transmitted shock wave and the Mach stem and (2) fluid that has interacted only with the incident shock wave. The path traveled by the triple point marks the boundary between these two regions. Because fluid that has interacted with the Mach stem has a lower velocity magnitude than fluid that has interacted with the incident shock wave, a shear layer develops on the contact surface, with vorticity in the opposite sense to the PVR.

After the shock wave returns to planarity, a slip surface is left in the flow field, just outside the surface of the shocked bubble. This process is depicted schematically in Fig. 42. The slip surface can be seen in the numerical vorticity plots of Figs. 38-40 as a blue streak traced around the shocked bubble. As time progresses, this shear layer deforms in Kelvin-Helmholtz-like roll-ups, which appear first at the farthest-upstream point on the shocked bubble and later at other locations nearer to the primary vortex ring. This is seen most clearly in the $M = 2.95$ late-time images shown in Fig. 41(c-c').

The emergence of these secondary vortices is significant for two reasons. First, they contribute to the elongation of the mixing region, as the two counter-rotating vortex rings tend to pull away from each other and eventually pinch off, as seen in Fig. 43. Second, vortex rings are stable coherent structures that persist to very late times and propagate downstream at nearly constant velocity. Thus, in shock-accelerated inhomogeneous flows where strong irregular shock refraction takes place in the inhomogeneities, long-lived vortex projectiles of this sort may be expected to arise in the flow as artifacts of shock

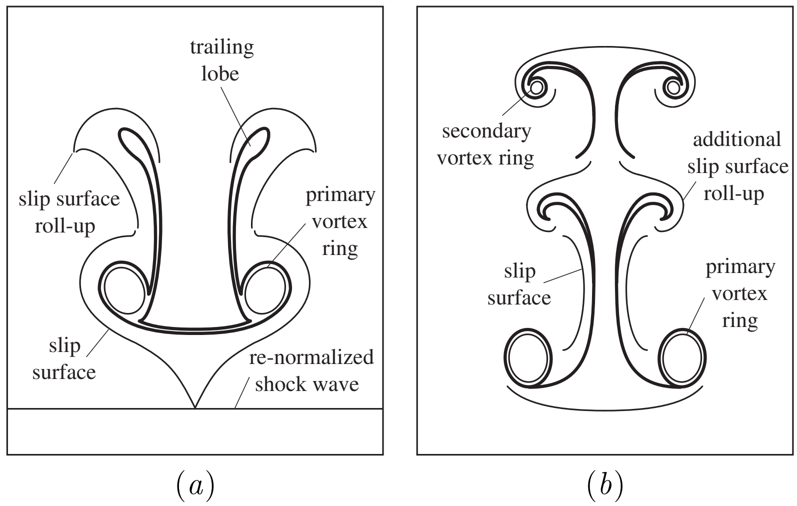

Figure 42: Schematic view of a secondary vortex ring generation in divergent refraction geometry ($A < 0$): (a) seeding of secondary vortex ring; (b) late-time separation of primary and secondary vortex rings.

refraction and persist to very late post-shock times.

Several relevant length scales are visible in the vortex dynamics of the shock-bubble interaction as shown in Fig. 44. The largest scale is the axial distance between the PVR and the SVR (scale 1). The second scale (scale 2) can be associated with the geometrical features (vortex major/minor diameter) of the PVR formed due to the initial baroclinic vorticity deposition. The smallest scale is that of the features associated with secondary instabilities like the Kelvin-Helmholtz instability seen on the edges of the PVR.

4.2 Convergent-Geometry: Mach Number Effects

Flow visualization images of a shocked Ar bubble in N_2, for $1.33 \leq M \leq 3.38$ are shown in this section, to highlight the Mach number effects in the convergent-geometry shock bubble interaction. This scenario corresponds to an Atwood number of $A = 0.176$.

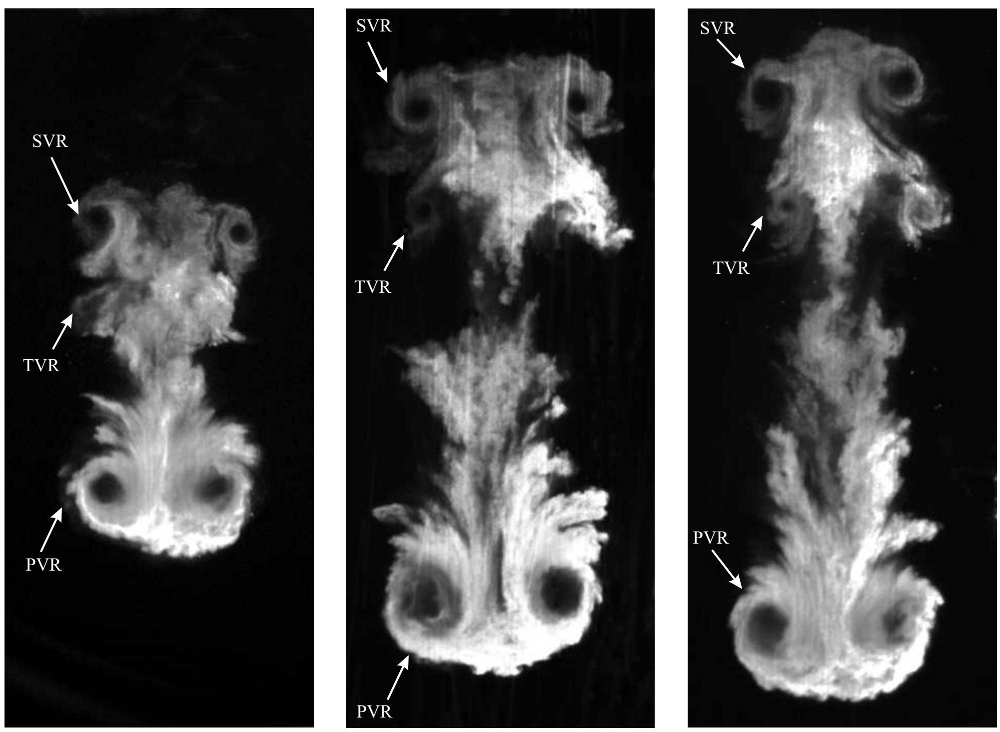

(a) (b) (c)

Figure 43: Late-time flow field visualizations of He bubble in N_2, $M = 2.95$. Dimensionless times τ are (a) 46.3, (b) 63.5, (c) 69.5. The characteristic time is $t' \approx 9.7$ μs, for a bubble initially of diameter 3.81 cm.

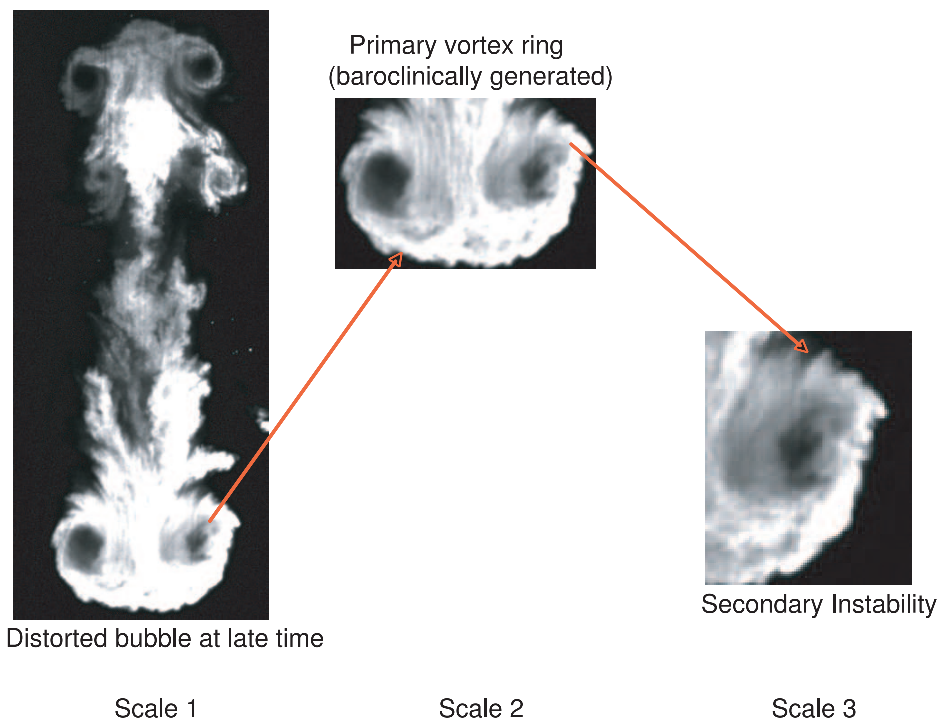

Figure 44: Length scales observed in shock-bubble interaction.

4.2.1 Argon bubble in nitrogen, $M = 2.88$

Figures 45-47 show the evolution of the shocked bubble after contact with a $M = 2.88$ shock with a wave velocity $W_i = 1017$ m/s, an N_2 particle velocity $u_1' = 745$ m/s and transmitted shock wave speed $W_t = 993$ m/s. Several experiments have been conducted and the reproducibility between different experiments is quite good with initial bubble diameters in the range $D = 5.0 \pm 0.02$ cm and incident Mach numbers in the range 2.88 ± 0.04. The time is non-dimensionalized in a similar fashion as described above.

In Fig. 45(a), the shock is visible midway through its transit across the argon bubble region. Bright points at the upper and lower limbs of the bubble indicate the upper and lower edges of the initial bubble film. The film layer is atomized upon shock impact, and microscopic particles of liquid film are entrained nearly uniformly into the flow behind the transmitted shock. The refractive effect of the heavier gas introduces a slight upward bow into the shock front, and the longitudinal compressive effect of the shock flattens the upper portion of the bubble. Shock refraction is complete in Fig. 45(b)and atomized film material still appears to be nearly uniformly distributed throughout the argon volume.

When the refracted shock wave is just downstream of the bubble, vortical features begin to emerge on the bubble surface, small perturbations can be seen developing on the outer limbs of the bubble in Fig. 45(c). These perturbations are the manifestation of the baroclinic vorticity deposition on the Ar-N_2 interface, which is strongest on the bubble surface tangent to the flow direction. Figure 45(d) shows the bubble when the shock is approximately 1.5 diameters downstream and the bubble has been compressed into an inverted bowl-type shape. The strongest vorticity deposition predicted by the

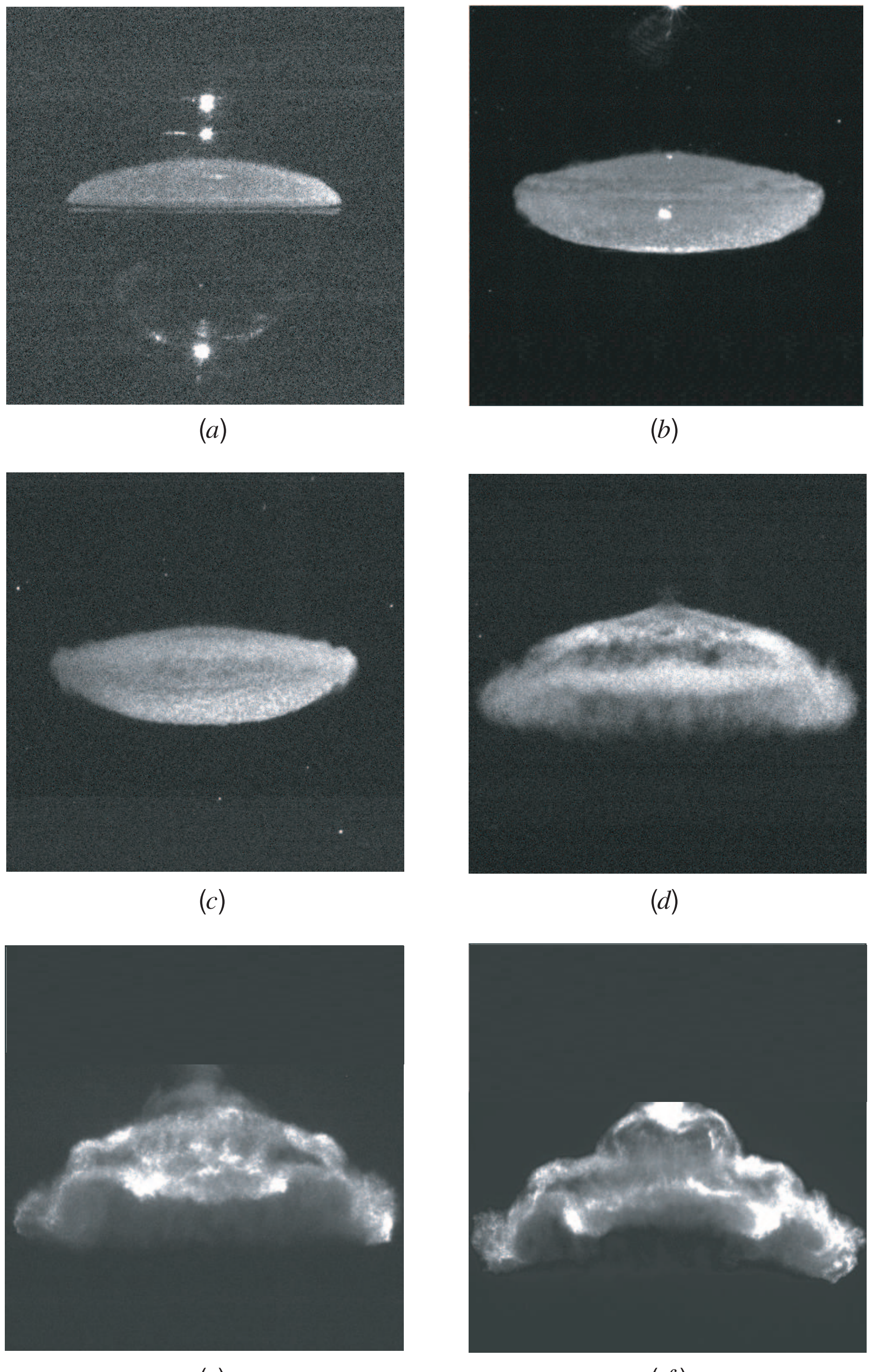

Figure 45: Experimental images of planar laser light Mie-scattered near the bubble midplane, at time τ after the initial interaction of a $M = 2.88$ shock wave in N_2 with an Ar bubble: (a) $\tau = 0.92$, (b) $\tau = 2.02$, (c) $\tau = 2.52$, (d) $\tau = 6.61$, (e) $\tau = 9.06$, (f) $\tau = 10.91$. The characteristic time is $t' \approx 25.2$ μs, for a bubble initially of diameter 5.0 cm.

baroclinic model is at the left and right bubble limbs, and at these locations, in Fig. 45(e-f), a primary vortex ring (hereafter referred to as PVR) can be seen developing at the downstream end of the bubble. Furthermore, the small scales introduced into the vorticity field by the presence of the film material lead to a number of secondary features that can be seen forming on the bubble surface at this time. The presence of film leads to the formation of the reflected shock wave from the downstream end of the bubble. The upper surface of the bubble is becoming distorted and a secondary vortex ring (hereafter referred to as SVR) associated with the appearance of an upper mushroom structure is becoming evident.

Figure 46 shows the development of the PVR and SVR in the flow field. The dominant feature seen in Fig. 46(a-b) is the PVR at the downstream end of the bubble while a small SVR is also observed at the upstream end of the bubble. The SVR at the upstream surface has the same sense of rotation as the PVR at the downstream surface of the bubble. The PVR entrains ambient fluid from the central/side portion of the image and swirls it into the center of the vortex ring. This is observed from the long tails, or dendrite-like structures, associated with the PVR, visible in Fig. 46(a-b).

In Fig. 46(c), along with the PVR and the SVR, a secondary jet (SJ) is evident at the top of the image. The secondary jet and vortex ring on the upstream surface of the bubble represent the combined effect of nonuniformities on the initial bubble film, and of the passage of the internally reflected shock over the upstream surface of the bubble. In particular, liquid film mass accumulated at the bottom of the initial bubble film in a gravitational meniscus is ejected in the upstream direction after shock passage, forming a jet which pierces the upstream surface of the bubble. This leads to the growth of additional vortical features near the apex and upper shoulders of the bubble. At the

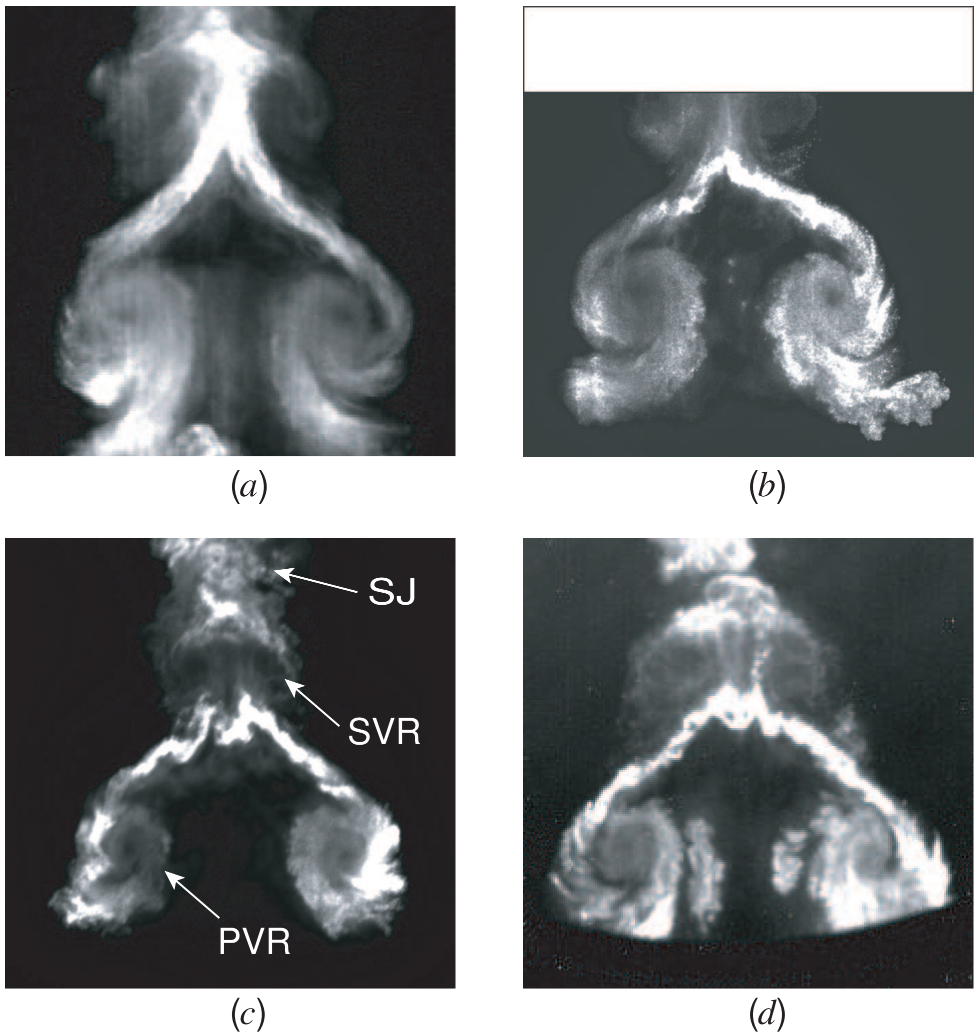

Figure 46: Experimental images of planar laser light Mie-scattered near the bubble midplane, at time τ after the initial interaction of a $M = 2.88$ shock wave in N_2 with an Ar bubble: (a) $\tau = 15.52$, (b) $\tau = 18.42$, (c) $\tau = 21.08$, (d) $\tau = 21.30$. The characteristic time is $t' \approx 25.2$ μs, for a bubble initially of diameter 5.0 cm.

same time, a reflected shock wave moves upstream across the Ar region from the interior bottom surface of the bubble, and upon crossing the upstream surface of the bubble, induces the further growth of secondary vortices as shown numerically by Zabusky *et al.* in 1998 [74] but never before confirmed experimentally.

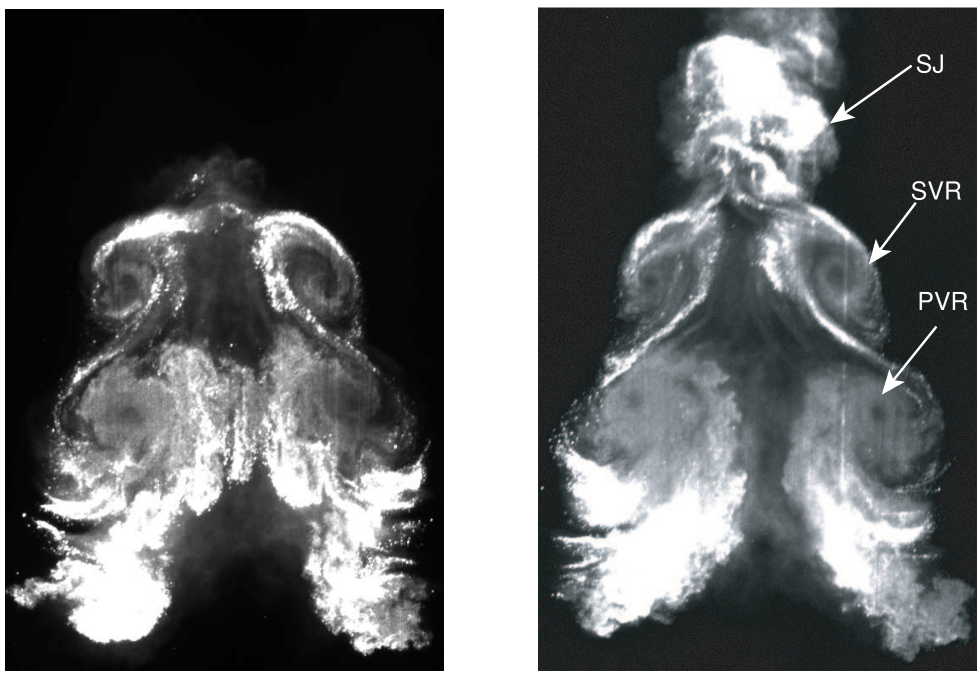

(a) (b)

Figure 47: Late-time experimental images of planar laser light Mie-scattered near the bubble midplane, at dimensionless time τ after the initial interaction of a $M = 2.88$ shock wave in N_2 with an Ar bubble: (a) $\tau = 28.68$, (b) $\tau = 29.09$. Each image represents a 9.0 cm $\times$ 13.6 cm region of the flow. The characteristic time is $t' \approx 25.2$ μs, for a bubble initially of diameter 5.0 cm.

The bubble asymmetry about the vertical axis observed in Fig. 46(d) is due to the onset of the bending mode instability commonly known as Widnall instability [71] for laminar flows. One can also observe that the PVR is connected at the top of the image through a cone-shaped channel (appearing as bright lines in a two dimensional

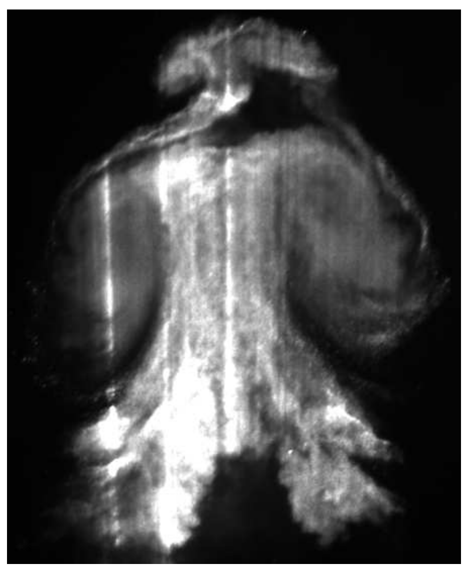

Figure 48: Experimental image of planar laser light Mie-scattered near the Ar bubble midplane, for incident shock wave strength $M = 2.88$ and dimensionless time $\tau = 39.70$. This image represents a 10 cm $\times$ 11 cm region of the flow. The characteristic time is $t' \approx 25.2$ μs, for a bubble initially of diameter 5.0 cm.

image) forming an approximately 45° angle to the horizontal. Figure 46 shows that this channel continues to shrink in thickness and increase in length as the ambient fluid is pulled into the vortex. The sum effect of these processes is the streamwise elongation of the bubble regions and the development of the secondary vortex ring on the upstream bubble surface. The primary vortex is stable even to very late times.

Figure 47(a) is at a much later time, when the shock is approximately ten diameters downstream. At this point of its evolution, the bubble appears to be undergoing intense fine-scale turbulent mixing in addition to major length scale growth. The PVR has pulled fluid from above into the central portion previously filled with nitrogen gas and tails of fluid also appear to develop from the PVR. Examination of the initial condition for this experiment has shown that there was no excess film accumulated at the bottom of the bubble. In contrast, Fig. 47(b) shows that the shocked bubble exhibits a strong upstream jet when excess film is initially present at the bottom of the bubble. Therefore, it is concluded, that the formation of the SVR is the result of the interaction of the internally-reflected shock wave with the upstream bubble surface. The excess mass of the film at the bottom leads to the secondary jet and enhances the geometry of the SVR. At late-times, the induced velocity due to the PVR leads to the entrainment of the SVR as it is apparent in Fig. 48. Similar flow features are visible in experiments involving shocks of higher and lower strength outlined in Sec. 4.2.2- 4.2.3.

The computed density and Ar volume fraction fields and their evolution over time, for a $M = 2.88$ planar shock, and a bubble with both the film layer and excess mass included, are shown in Fig. 49. Simulations without film material [47] have shown that shock diffraction, combined with a reflected rarefaction, can lead to the development of weak secondary upstream jet and vortex ring, but this effect becomes more intense with

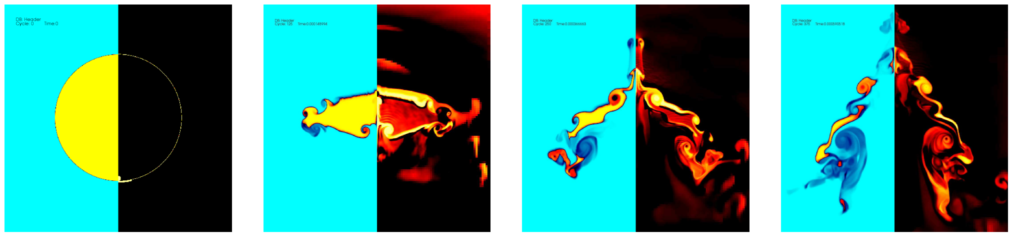

(*a*) (*b*) (*c*) (*d*)

Figure 49: Montage of computed flow field for $M = 2.88$ and a nonuniform initial film layer. Left: Ar volume fraction; right: total density. (*a*) $\tau = 0$, (*b*) $\tau = 4.65$, (*c*) $\tau = 13.17$, (*d*) $\tau = 21.93$. The characteristic time is $t' \approx 25.2$ μs, for a bubble initially of diameter 5.0 cm.

the presence of a film layer. This is clearly seen in Fig. 49(*b*-*d*). Early-time comparison between the experimental and simulation image is shown in Fig. 50. Five geometrical features are marked on both the experimental and simulation image. All of these features, except the vortex core (feature 5), are small scale features of the flow. In both experiment and simulation, we observe the breaking of axial symmetry at late times. The experimental bubble has inherent asymmetry in its initial condition due to perturbations imposed by the bubble inflation and release processes; the simulated bubble has grid-seeded perturbations. At late-times, these lead to the growth of azimuthal variations in the flow field, by a Widnall- type bending mode instability [71]. Vortex rings develop bends and kinks, and vortical fluctuations grow, leading to chaotic, turbulent motion in some regions of the flow. This is clearly illustrated in the three-dimensional rendered plot of the late-time flow field shown in Fig. 51.

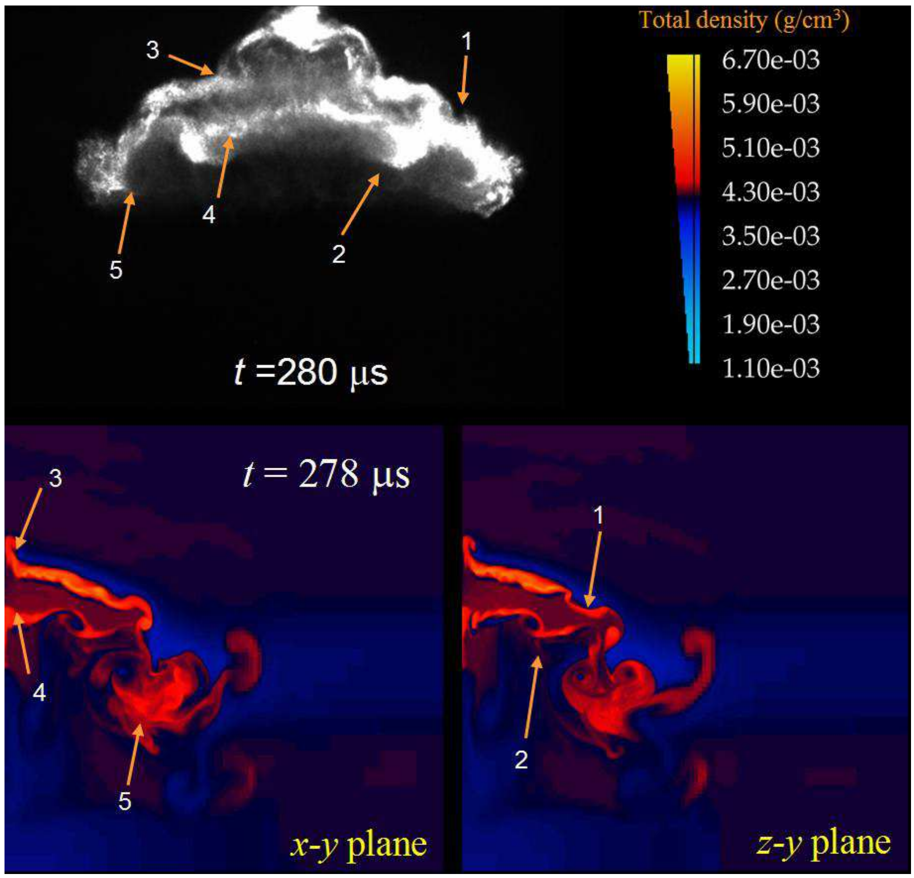

Figure 50: Comparison between experimental and simulation image at early-time, $M = 2.88$. Simulation shows density plot on two different planes of the shocked bubble. Five similar features are labeled on the experimental and simulation images: (1) vortical inward divot at shocked bubble shoulder, (2) filaments at interior bubble waist being drawn inward, forming a KH-type radially-inward oriented rollup or arc, (3) bases of axial pedestal at bubble upstream pole, (4) shocked bubble downstream surface and (5) spiral/cyclonic structure at outermost rim of shocked bubble, rotating under influence of the primary vortex core.

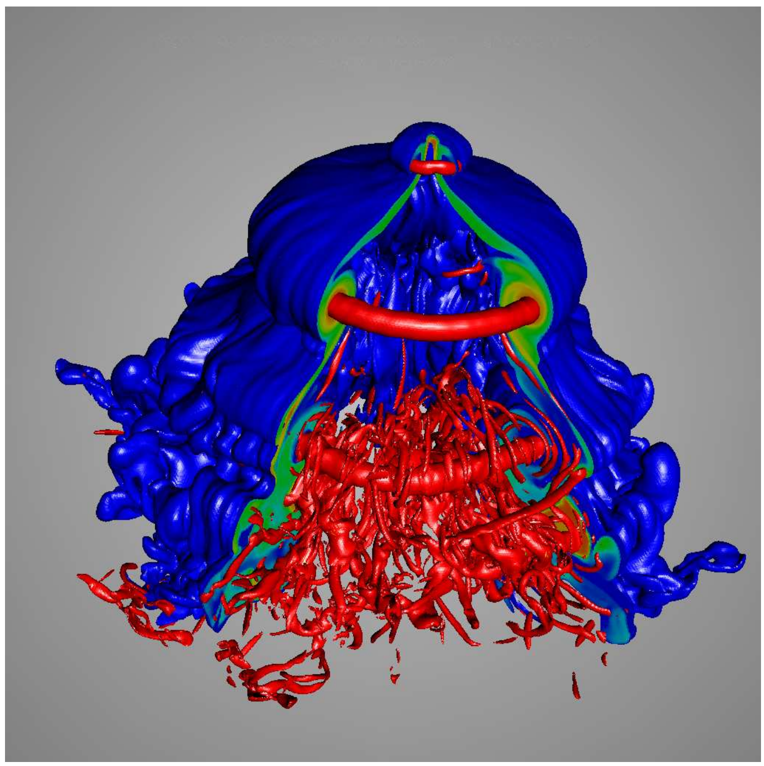

Figure 51: Argon bubble with soap film, shocked at $M = 2.88$ in a nitrogen environment, from a three-dimensional simulation using *Raptor*. The 0.1 isosurface of argon volume fraction is shown in blue, and an isosurface of vorticity magnitude is shown in red in the cut-out region. The bubble is shown at a dimensionless time $\tau = 20.14$. The characteristic time is $t' \approx 25.2\ \mu$s, for a bubble initially of diameter 5.0 cm.

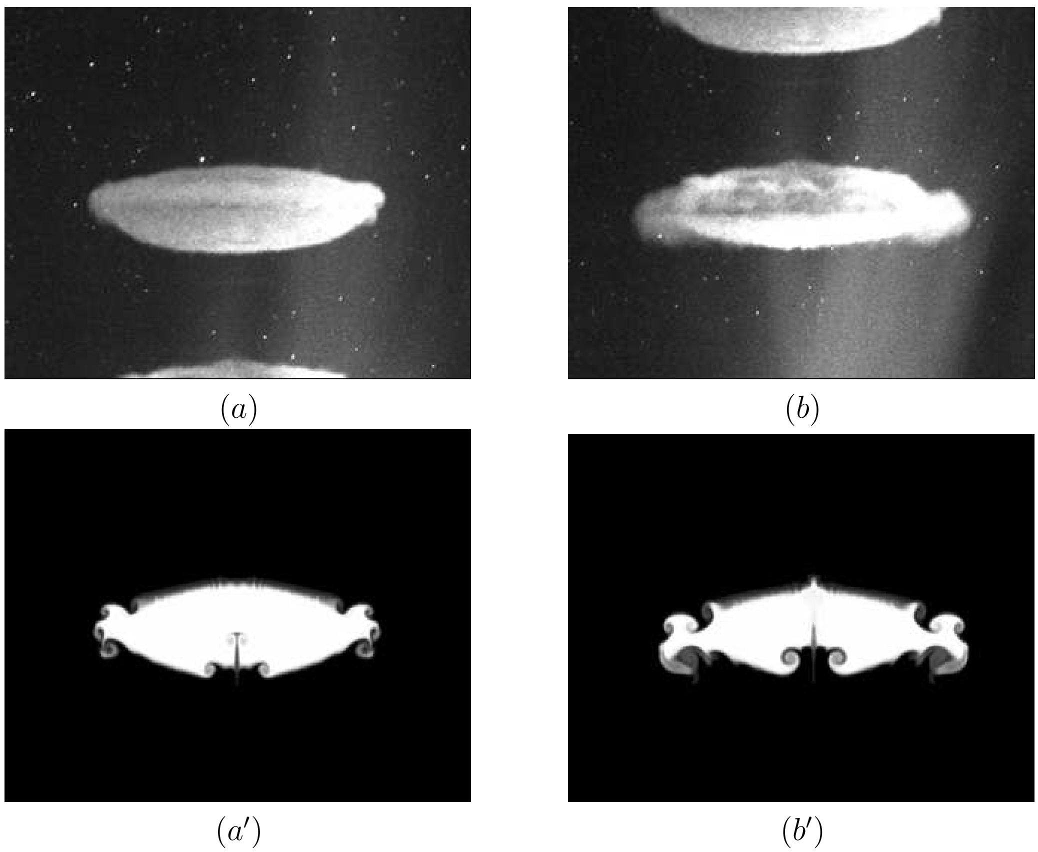

Figure 52: Experimental images (a,b) and computational argon volume fraction (c,d) , for an $M = 3.38$ shock in nitrogen (moving vertically from top to bottom) incident on an argon bubble. Non-dimensional times τ are given relative to shock arrival at the top of the bubble. (a) $\tau = 2.0$, (b) $\tau = 4.0$, (a') $\tau = 3.0$, (b') $\tau = 4.6$. The characteristic time is $t' \approx 21.3$ μs, for a bubble initially of diameter 5.0 cm. Shock motion is from top to bottom.

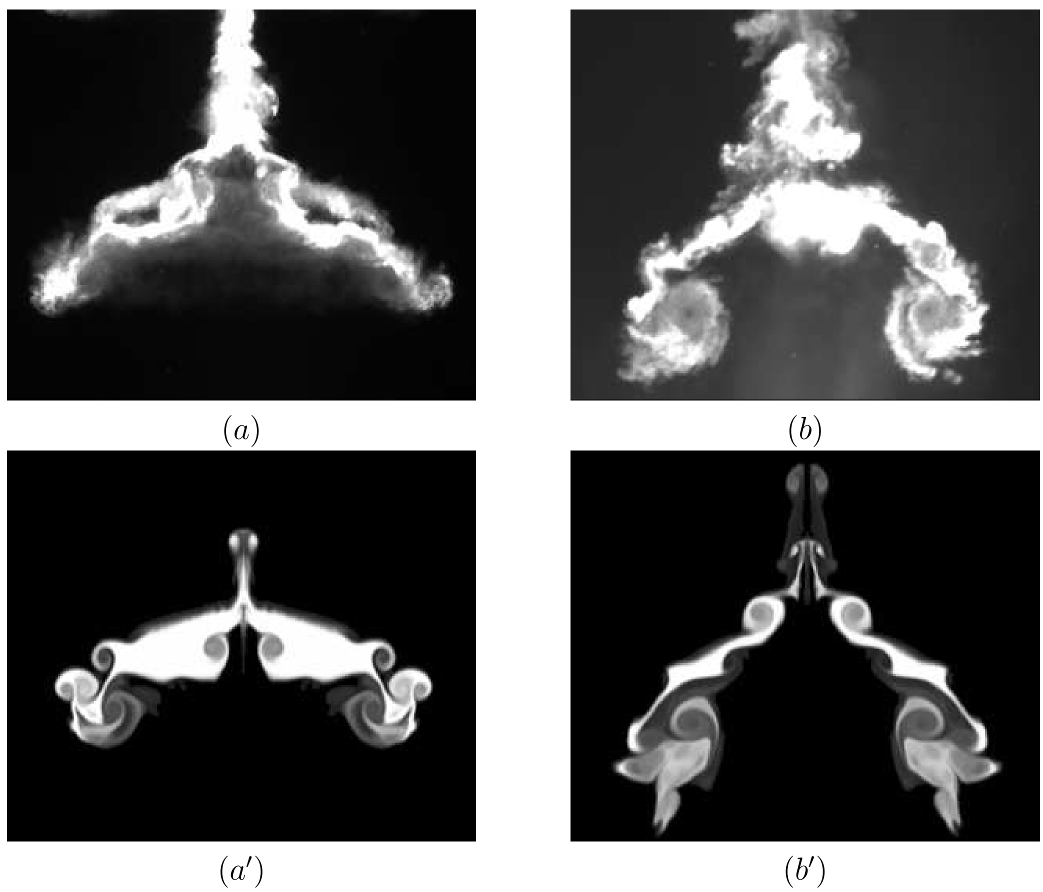

Figure 53: Experimental images (a,b) and computational argon volume fraction (c,d) , for an $M = 3.38$ shock in nitrogen (moving vertically from top to bottom) incident on an argon bubble. Non-dimensional times τ are given relative to shock arrival at the top of the bubble. (a) $\tau = 7.1$, (b) $\tau = 14.3$, (a') $\tau = 7.9$, (b') $\tau = 14.7$. The characteristic time is $t' \approx 21.3$ μs, for a bubble initially of diameter 5.0 cm. Shock motion is from top to bottom.

4.2.2 Argon bubble in nitrogen, $M = 3.38$

Figure 52 shows the early-time shocked bubble development for $M = 3.38$. Figure 52(a, a') illustrates the initial compression of the bubble to an ellipsoidal shape, and developing vortical features can be seen in the Fig. 52(b, b') at the outer limbs of the bubble, which grow to form a well-defined vortex ring at later times. In Fig. 53(a, a') a strong jet due to excess film material is seen extending upstream from the apex of the bubble, along with a SVR growing on the upstream bubble surface. The PVR, however, remains the dominant feature of the flow, and maintains its coherent structures even at late time, as seen in Fig. 53(b). The bending of the vortex ring is evident in both the experimental and simulation images. Figure 54 shows that the vertical jet and secondary vortex rings are amplified if both an interior and exterior drop of film material are present in the initial condition at the bottom extremity of the bubble. It is important to note that even in the absence of excess film material adhering to the bottom extremity, a very small vertical jet and SVR are visible in the simulation image.

During the $M = 3.38$ experimental campaign, one of the imaging windows was broken due to the dynamic shock loading, which significantly changed our experimental plan for this Mach number. After this incident, no more experiments were performed at this Mach number. Therefore, no experimental image is available to show the late-time behavior for the shocked bubble at this Mach number.

4.2.3 Argon bubble in nitrogen, $M = 1.33$

At $M = 1.33$, the evolution of the shocked bubble is similar and experimental results are shown in Fig. 55. Figure 55a represents the shadowgraph image acquired during

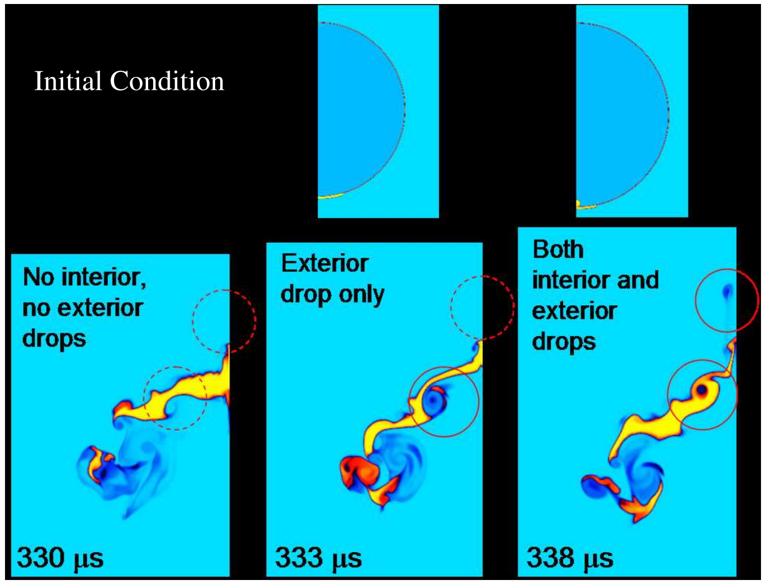

Figure 54: Simulation images indicating the effect of the non-uniformities on the post-shock flow. Vertical jet and secondary vortex rings are amplified if both and interior and exterior drop of film material are present in the initial condition.

the compression phase of the bubble. The bright vertical line in the center of the image indicates the location of the laser sheet. The shock deposits vorticity on the bubble surface, which subsequently deforms into a PVR. Also it may be noted that, because of the lower energy deposited by the shock on the bubble film, the atomization is less efficient, which results in large particles of liquid film in the flow, as seen in Fig. 55(b). Due to the presence of film in the experiment, the internally reflected shock is stronger than in the filmless numerical case. Therefore, even at a low Mach number a small SVR is evident in Fig. 55(d) but is no longer seen in Fig. 55(e-f), while the PVR remains the most dominant feature of the flow. The vortical cores are much more defined when compared with the high Mach number experiments at late times. During these experiments, efforts were made to eliminate the excess initial mass deposition at the downstream pole of the bubble. With the excess initial film mass eliminated, no secondary vertical jet at the apex of the bubble is observed in the post-shock flow shown in Fig. 55. However, the simulations were performed using the same initial condition as the other Mach numbers. Simulation images in Fig. 56 show a very good agreement with the experimental images even at the late-time. The only difference between simulation and experiment is the presence of the secondary vertical jet in the simulation. Figure 57 highlights the similarities between the experimental and simulation image at late-time, where the entrainment patterns observed in the experiments are observed in the same spatial locations as the bubble density in the simulation.

4.2.4 Argon bubble in nitrogen, M=2.03

Figure 58 shows the development of an argon bubble accelerated by a $M = 2.03$ shock wave in nitrogen. The evolution of the shocked bubble is similar to the low and high Mach number scenarios discussed earlier in this section. The shock wave propagation leads to the compression of the bubble visible in Fig. 58(b). A distinguishable vortex ring core forms in the flow field by $\tau = 11$ as seen in Fig. 58(c) due to the baroclinic vorticity deposition, and remains the dominant feature of the flow through late times, as seen in Fig. 58(d).

To summarize, in all the four cases, a distinguishable vortex ring core forms in the flow field due to the baroclinic vorticity deposition. In the case of $M = 1.33$, this core is visible by $\tau = 20$; while in the case of $M = 3.38$, it is visible much sooner (by $\tau = 8$). In all the cases, the refractive effect is very weak due to the small magnitude of A. Therefore, as seen in Fig. 58(a), the transmitted shock wave front inside the bubble looks planar. A secondary vortex ring is visible at the apex of the bubble in all the

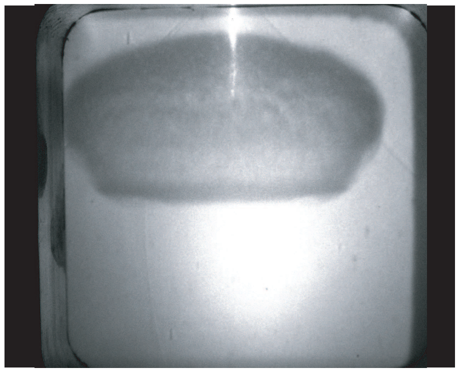

(a)

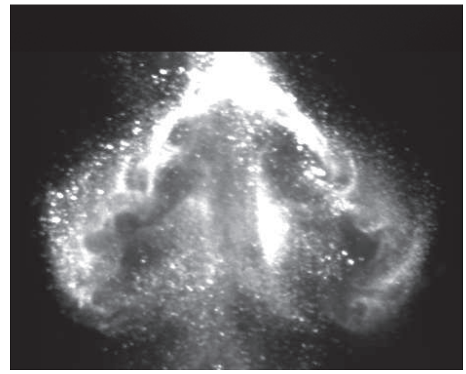

(b)

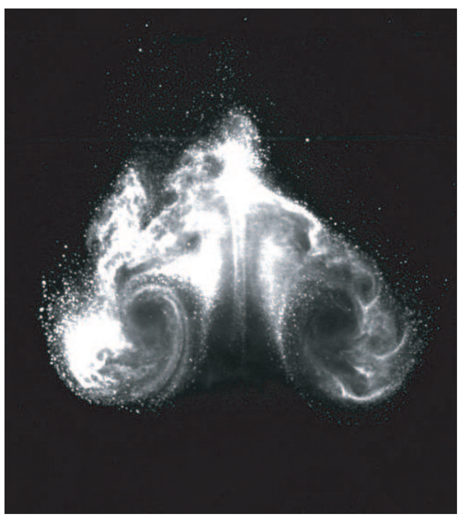

(c)

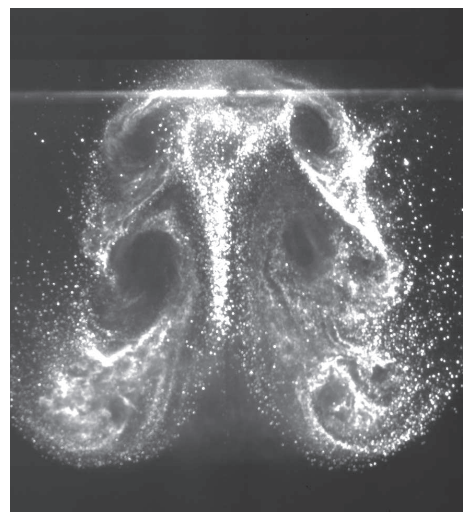

(d)

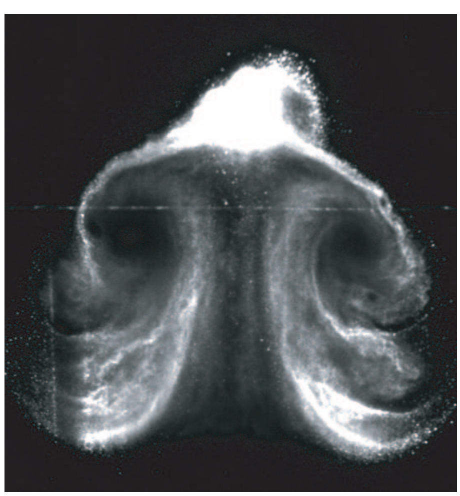

(e)

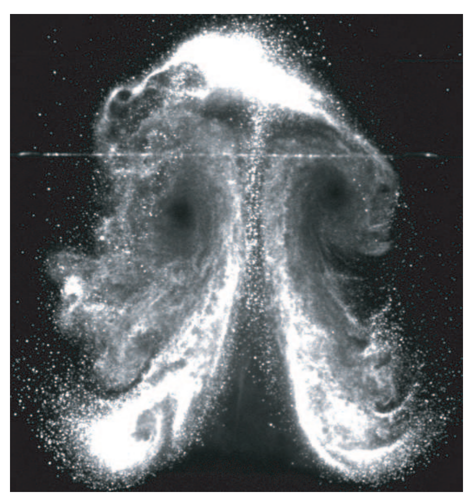

(f)

Figure 55: Flow field evolution for Ar bubble in N_2, $M = 1.33$. Dimensionless times τ are (a) $\tau = 9.5$, (b) $\tau = 15.5$, (c) $\tau = 26.6$, (d) $\tau = 46.5$, (e) $\tau = 51.5$, (f) $\tau = 71.5$. The characteristic time is $t' \approx 57.1$ μs, for a bubble initially of diameter 5.0 cm. Shock motion is from top to bottom. Image shown in (a) is obtained using shadowgraphy technique.

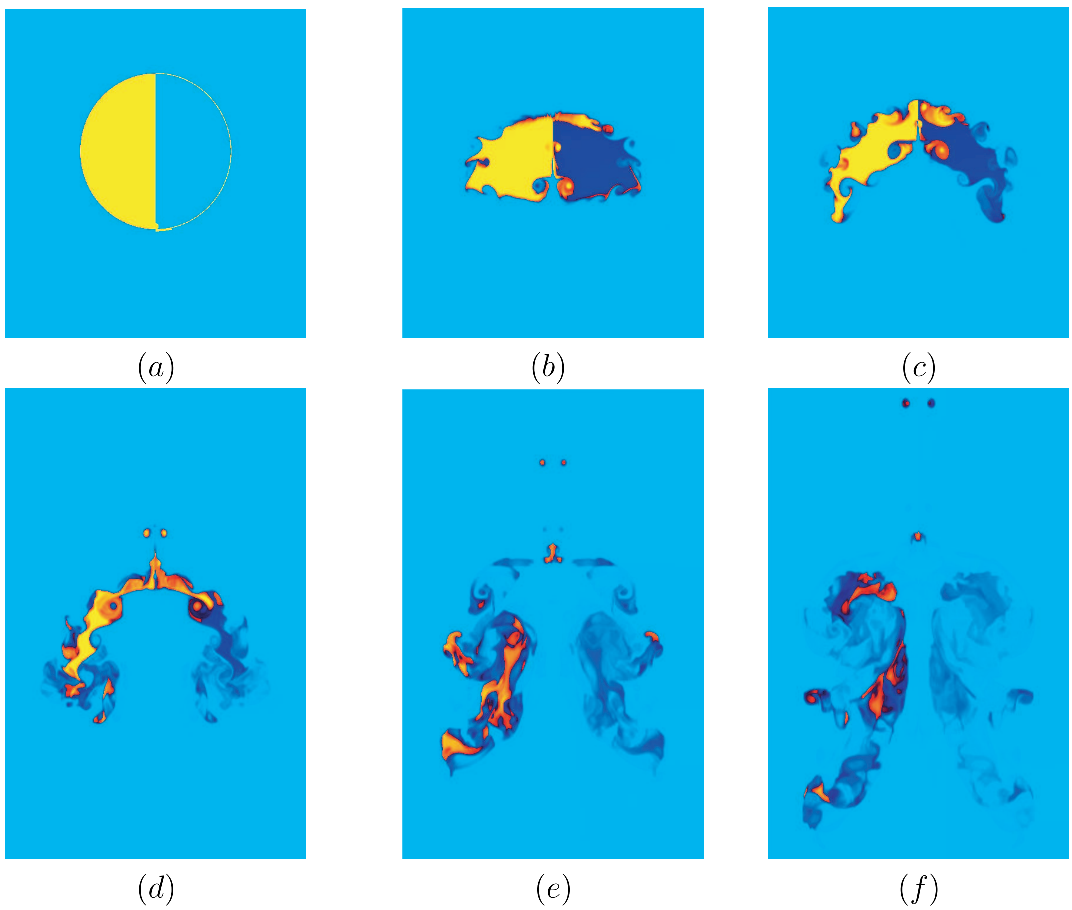

Figure 56: Montage of computed flow field for $M = 1.33$ and a nonuniform initial film layer. Left: Ar volume fraction; right: total density. (a) $\tau = 0$, (b) $\tau \approx 9.5$, (c) $\tau \approx 15.5$, (d) $\tau \approx 26.0$, (e) $\tau \approx 47.5$, (f) $\tau \approx 71.0$. Non-dimensional times τ are given relative to shock arrival at the top of the bubble. The characteristic time is $t' \approx 57.1$ μs, for a bubble initially of diameter 5.0 cm. Shock motion is from top to bottom.

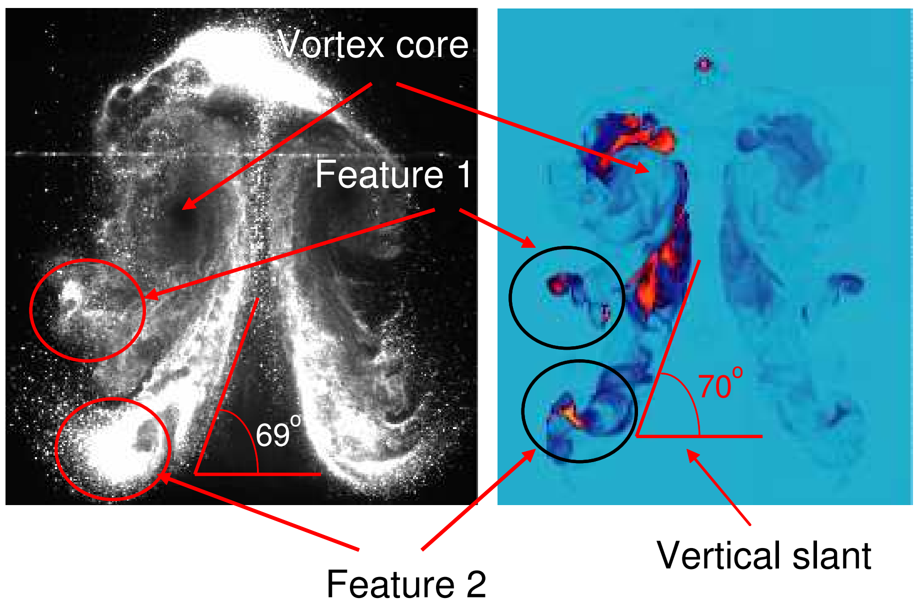

Figure 57: Comparison between experimental and simulation images (Left: Ar volume fraction; right: total density) at late-time ($\tau \approx 71.5$), $M = 1.33$. Feature 1: petal or filament of shocked bubble material (or film material) trailing the primary vortex core in a spiral structure. Feature 2: Similar feature as 1 but trailing at greater downstream distance, in longer, more gentle arc. The characteristic time is $t' \approx 57.1$ μs, for a bubble initially of diameter 5.0 cm.

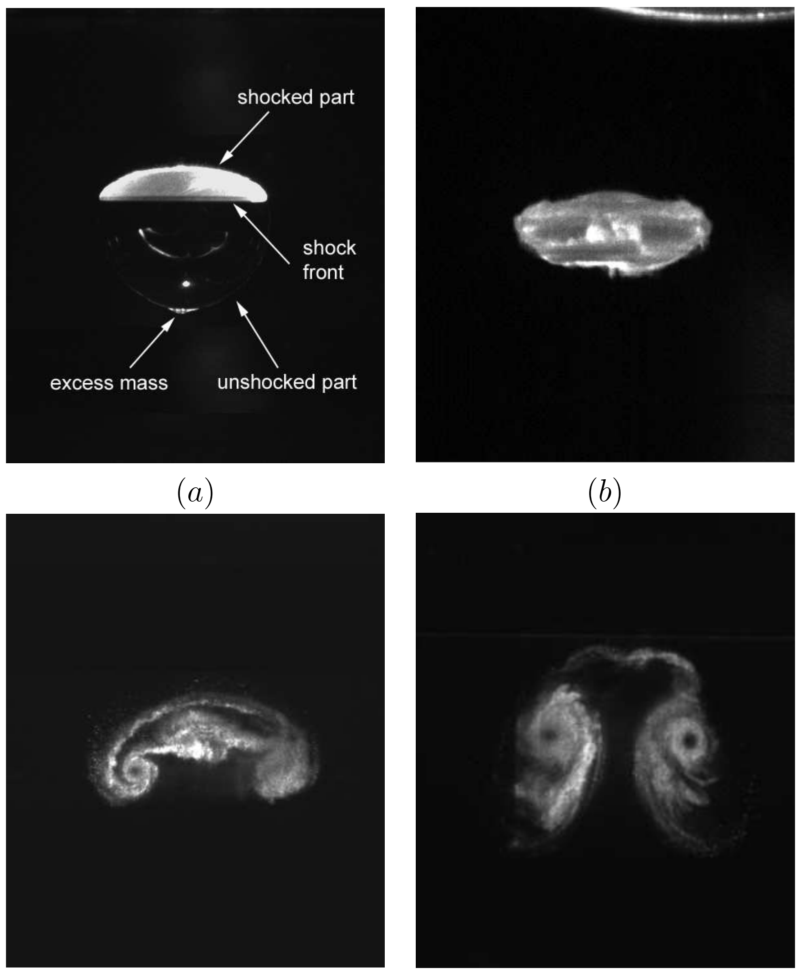

(a) (b) (c) (d)

Figure 58: Experimental images of a shocked ($M = 2.03$) Ar bubble in N_2. Non-dimensional times τ are given relative to shock arrival at the top of the bubble. (a) $\tau = 0.74$, (b) $\tau = 3.05$,(c) $\tau = 11.55$, (d) $\tau = 36.87$. The characteristic time is $t' \approx 36.3$ μs, for a bubble initially of diameter 5.0 cm. The width of the field of view in each image is 7.5 cm.

cases; however, it is more prominent in the high Mach cases. The presence of excess film mass at the bottom of the bubble leads to the formation of a secondary jet at the apex of the bubble, and in all four cases, the flow field at late-times is dominated by the primary vortex ring.

4.3 Convergent-Geometry: Atwood Number Effects

In order to study the Atwood number effects, and to deepen the understanding of the shock-refraction phenomenon for convergent-geometry shock-bubble interaction, three more experimental campaigns (scenarios 9-11, Tab. 1) are performed for $A > 0.5$. In this section, flow visualization images are presented for those three scenarios and comparisons are made to the results obtained for low Atwood number scenarios discussed in Sec. 4.2.

4.3.1 Refrigerant-22 bubble in nitrogen, M=2.03

Figure 59 shows the development of a Refrigerant (R-22) bubble accelerated by a $M =$ 2.03 shock wave in nitrogen. This scenario corresponds to an Atwood number of $A =$ 0.516. In this case, $t' \approx 35.4$ μs, for a Refrigerant (R-22) bubble initially of radius 1.6 cm. The upper and lower images of Fig. 59(a) illustrate the initial compression of the bubble and development of the vortical structures at the side of the bubble. The one striking difference between the flowfield shown in Fig. 59(a) and Fig. 58(b) is the appearance of a small axial jet at the downstream end of the bubble. This small jet is formed due to the focusing of the transmitted shock wave at the downstream pole of the bubble.

In the high Atwood number scenarios as depicted in figure 8, a portion of the shock

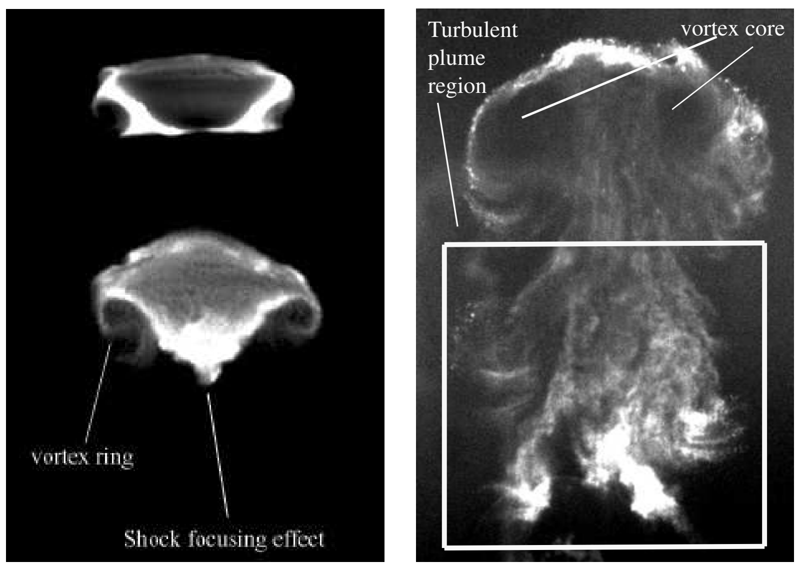

(a) (b)

Figure 59: Experimental images of a shocked ($M = 2.03$) R-22 bubble in nitrogen. Non-dimensional times τ are given relative to shock arrival at the top of the bubble. (a) top: $\tau = 2.0$; bottom:$\tau = 2.6$, (b) $\tau = 25.1$. The characteristic time is $t' \approx 35.4$ μs, for a bubble initially of diameter 3.2 cm. The width of the field of view in each image is 7.5 cm.

wave front sweeping around the bubble periphery is diffracted, meaning it is turned toward the axis so that the surface of discontinuity remains nearly normal to the interface [21, 48]. The diffracted shock waves then collide with each other at the downstream pole. The diffracted shock wave collision, along with the focusing of the transmitted shock wave, produces an intense pressure jump and initiates additional baroclinic vorticity deposition. Secondary shock waves are generated due to shock focusing and lead to dramatic changes in the observed flow field at late times. This effect can be compared to a reshock phenomenon, familiar from Richtmyer-Meshkov flows in shock tubes. Figure 59(b) shows that the late-time flow field is dominated by a turbulent plume rather than the primary vortex ring as seen in Fig. 58(d).

4.3.2 Sulfur-hexafluoride bubble in nitrogen, M=2.07, 2.94

Figure 60 shows the development of a sulfur-hexafluoride bubble accelerated by a $M = 2.07$ shock wave in nitrogen. This scenario corresponds to an Atwood number of $A = 0.681$. In this case, the refractive effect is quite strong when compared to the Ar-N_2 scenario. Thus, the transmitted shock wave has a concave curvature right from the beginning of the shock propagation through the bubble as shown in Fig. 60(a). The shock wave propagation leads to the compression of the bubble visible in Fig. 60(b), where the unshocked part of the bubble is also visible. Due to the shock focussing effect described in sec 4.3.1, the late-time flow field is again dominated by a turbulent plume as seen in Fig. 60(d).

A complex field of secondary shock waves is generated between the shocked bubble and the incident shock wave after shock focussing. The secondary shock waves propagating in the lateral and upstream directions traverse the already deforming bubble and

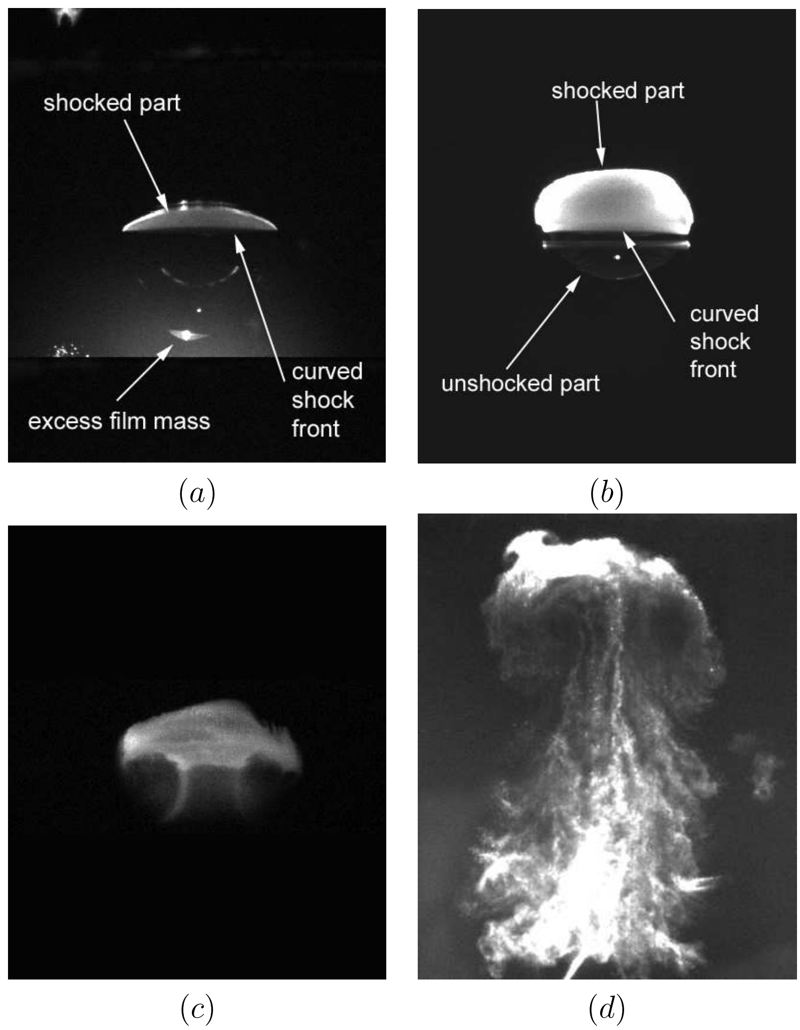

Figure 60: Experimental images of a shocked ($M = 2.07$) sulfur-hexaflouride bubble in nitrogen. Non-dimensional times τ are given relative to shock arrival at the top of the bubble. (a) $\tau = 0.43$, (b) $\tau = 0.82$,(c) $\tau = 2.18$, (d) $\tau = 14.14$. The characteristic time is $t' \approx 43.0$ μs, for a bubble initially of diameter 3.2 cm. The width of the field of view in each image is 7.5 cm.

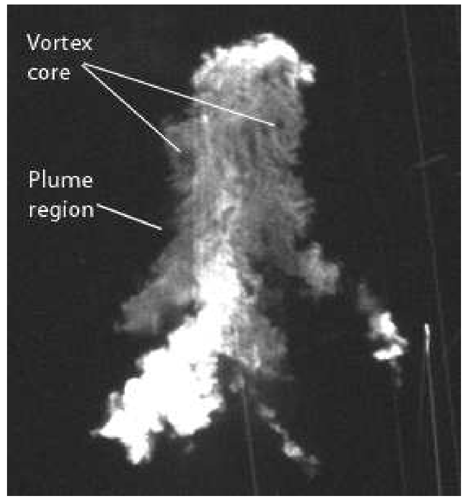

Figure 61: Late-time experimental image of a shocked ($M = 2.94$) sulfur-hexaflouride bubble in nitrogen. The bubble is shown at a dimensionless time $\tau = 17.9$. The characteristic time is $t' \approx 28.2$ μs, for a bubble initially of diameter 3.2 cm.

enhance the complexity of the evolving vorticity field. More small-scale features are observed in the turbulent plume region here, compared to the one seen in Fig. 59(d) for R-22 bubble. The plume region observed in Fig. 60(d) represents a strongly disordered state of the vorticity field. Fig. 61 shows the late-time flow field for a sulphur-hexafluoride bubble accelerated in nitrogen by a $M = 2.94$ shock wave. Due to the combined intensity of the shock focusing effects and the azimuthal transport of vorticity, the vortex ring is highly distorted and nearly indistinguishable. The shocked bubble is effectively reduced to a small core of compressed fluid, which trails behind a plume-like structure indicative of a well-developed mixing region.

These results show good agreement with calculations performed by Niederhaus *et al.* [48], showing the distinct effects that arise due to shock focusing in the case of an R12 bubble ($A = 0.613$) accelerated by a $M = 5.0$ shock wave. Results presented in Section 4.2.2 showed that the primary vortex ring existed at very late times in the case of low Atwood number flow even at high Mach number and suggest that the increased Mach number is not itself sufficient to induce the development of this plume feature. The growth of this turbulent plume is mostly due to the nonlinear acoustic effects which are associated with the density contrast between the bubble and the ambient gas.

Chapter 5

Analysis and Discussion

This chapter provides a detailed analysis of quantitative measurements obtained from the experimental data. Quantitative measurements include: a) translational velocities of the bubble and the associated vortex rings, b) circulation (deduced from the rings' velocity-defect), and c) different geometrical length scales (axial/lateral extents of the bubble and minor/major diameters of the vortex rings).

Figure 62 shows the pixel intensity line-out across the core of the primary vortex ring formed during the interaction of an argon bubble with an $M = 2.88$ shock wave in nitrogen. The line-out reveals the location of the center of the vortex ring, vortex core and edges of the core. From these line-outs, the length scales are measured in the experiments. Features from the line-out identified by local minima and maxima in pixel intensity can be directly compared with those from the numerical simulation results.

5.1 Translational Velocity

The translational velocities of the bubble and vortex ring after shock interaction have been studied numerically and theoretically. Different velocity models have been discussed in Section 2.6.

Figure 63 shows three pairs of post-shock images, where each pair was captured on the same CCD array. The bubble and vortex displacements measured from such images

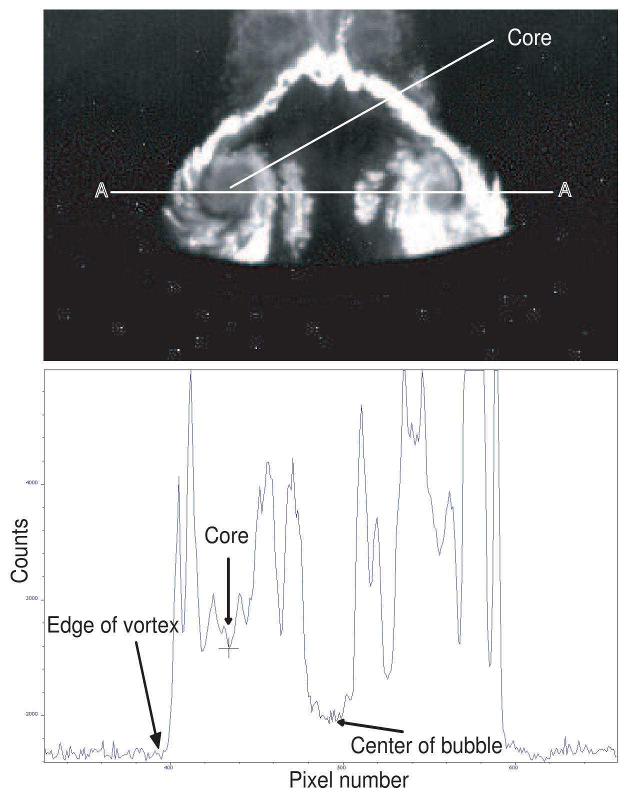

Figure 62: Pixel line-out across the core of primary vortex ring formed during the interaction of an argon bubble with an $M = 2.88$ shock in nitrogen.

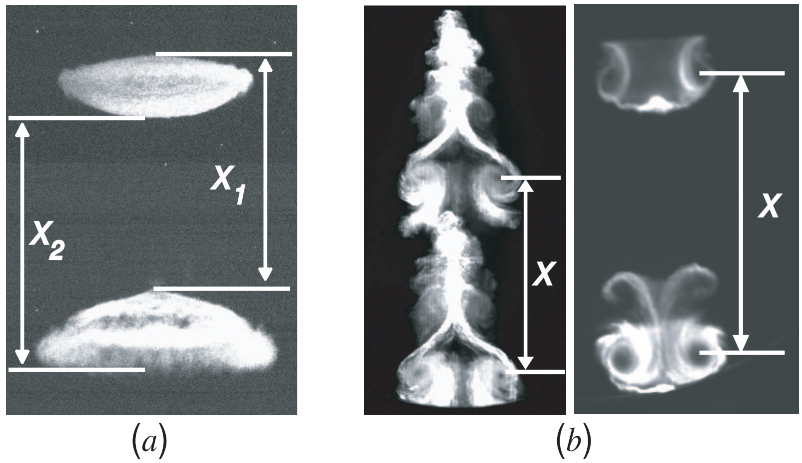

Figure 63: Schematic representation of displacement measurement in shock-bubble interactions at: (a) early-phase and (b) late-times.

are used to obtain the bubble velocity V_b and vortex velocity V_v. At early times, the velocity is that of the bubble whose location is measured as the average of the top and bottom of the bubble as shown in Fig. 63(a). The initial bubble velocity is then computed as $V_b = 0.5\,(X_1 + X_2)\,/\Delta t$, where Δt is the time difference between these images. After a distinct, identifiable vortex core has formed, the vortex velocity is measured for experiments where two post-shock images are obtained on a single image as shown in Fig. 63(b). The translational velocity of the vortex ring is computed as $V_v = X/\Delta t$, where X is the displacement of the vortex measured over Δt. This velocity is plotted at the mean of the two image times.

Figure 64 shows the velocity of an argon bubble V, accelerated by a $M = 2.88$ shock wave in nitrogen and non-dimensionalized by the shocked gas particle speed (u_1'), as a function of time. The bubble velocity behaves in a similar fashion to that observed for a weakly-shocked krypton bubble in air by Layes *et al* [35]. That is, the bubble initially accelerates up to the particle velocity (within the experimental error), and then the velocity falls below the particle speed at later times due to the formation of the vortex ring. The measurement error is on the order of 1% based on the spatial accuracy of the CCD image and the timing jitter for the two laser pulses.

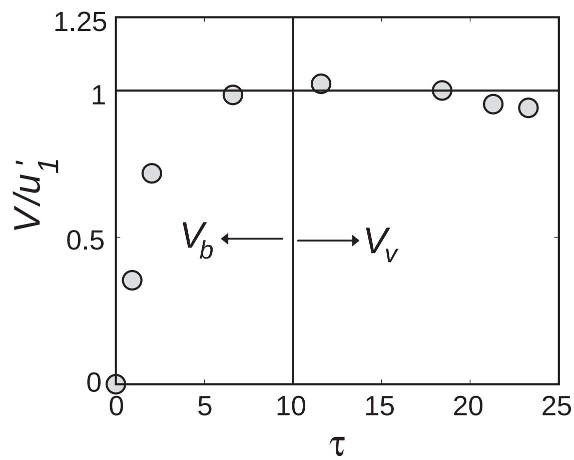

Figure 64: Velocity of an argon bubble accelerated by a $M = 2.88$ shock in nitrogen ($A = 0.176$). In the early phase of the bubble growth, it is represented as V_b and later, after the growth of the vortex ring, as V_v.

The ratio of the vortex velocity to the particle speed, V_v/u_1', is calculated at late-time using the Picone-Boris (Eq. 2.20) and Rudinger-Somers velocity models (Eq. 2.16). Table 2 shows the normalized vortex velocity V_v/u_1' averaged over all times $2tu_1'/D > 20.0$ for experimental scenarios 5-8 (see Tab. 1), along with the predictions of the Picone-Boris and Rudinger-Somers model. The circulation-based model of Picone and Boris provides a reliable prediction for the experimentally measured values for $M > 2.0$, with the difference between the model and the experimental data being less than 2%. On the other hand, the difference between the Rudinger-Somers model and the experimentally measured data is about 5% for $M < 2.5$. In summary, both models show very good agreement with the measured values from the experiments for these scenarios.

M	V_v/u'_1 Experiment	V_v/u'_1 PB model	V_v/u'_1 RS model
1.33	0.94	0.954	0.912
2.03	0.96	0.961	0.935
2.88	0.96	0.964	0.960
3.38	0.97	0.965	0.970

Table 2: Normalized vortex velocity, measured in experiments, and predicted by the Picone-Boris (PB) and Rudinger-Somers (RS) models for Ar bubble in N_2 scenarios ($A = 0.176$). In the experiments, the value is computed as a mean of velocities for $2tu'_1/D > 20.0$.

In the case of the shocked helium bubble (Tab. 1, scenarios 1-3), multiple vortex rings are seen at late-times in the flow field. In order to compare the vortex velocity in these scenarios, the ratio of the translational velocity associated with the primary vortex ring to the post-shock ambient flow speed u'_1, is plotted in Fig. 65 along with the simulation results. Also shown in this plot (right margin) are the values predicted using the Picone-Boris model. The experimentally measured velocities, like those obtained from simulations, oscillate strongly during the initial transient phase (particularly for $M = 1.45$), and arrive at a nearly steady value slightly greater than u'_1 at later times. The initial variability persists only until a coherent vortex structure forms.

After $2tu'_1/D \approx 5$, the vortex ring velocity does not diminish significantly throughout the duration of the experiments or simulations. The normalized vortex ring velocity V_v/u'_1, averaged over all times $2tu'_1/D > 7.5$ for each scenario, is shown in Table 3, along with the predictions of the Picone-Boris and Rudinger-Somers models, and the experimentally measured averaged values. We see that the vortex ring which rotates in an opposite sense to the heavy bubble, moves at a substantially higher speed than the surrounding gas – as much as 35% higher in the simulations – although the relative

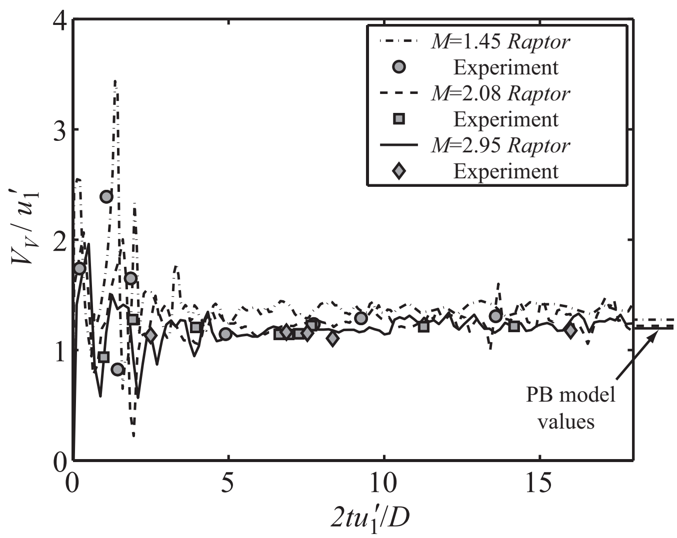

Figure 65: Normalized translation speed of primary vortex ring, plotted on a dimensionless timescale based on the ambient shocked flow speed u_1' for helium bubble in air/nitrogen scenarios ($A \approx -0.8$). Symbols represent experimental data; lines represent simulation results. Horizontal lines on the right margin indicate normalized translation speeds predicted by the Picone-Boris model.

M	V_v/u'_1 Simulation	V_v/u'_1 Experiment	V_v/u'_1 PB model	V_v/u'_1 RS model
1.45	1.354	1.277	1.276	1.589
2.08	1.255	1.216	1.220	1.589
2.95	1.219	1.146	1.197	1.581

Table 3: Normalized primary vortex ring translation speed for helium bubble in air/N_2 ($A \approx -0.8$), computed from simulations, measured in experiments, and predicted by the Picone-Boris (PB) and Rudinger-Somers (RS) models for divergent geometry shock-bubble interactions. In the experiments and simulations, the value is computed as a the mean of velocities measured for $2tu'_1/D > 7.5$.

velocity between the bubble and the ambient gas decreases significantly as the Mach number increases.

Once again, the circulation-based model of Picone and Boris provides a reliable prediction for the experimentally measured velocity. The difference between the Picone-Boris model and the experimentally measured values is less than 2%. The Rudinger-Somers model, on the other hand, drastically overestimates the vortex ring velocity relative to both simulations and experiments for the divergent geometry of these particular scenarios, although it showed good agreement for the convergent-geometry shock-bubble interactions. As for the vortex ring velocities obtained from the simulations, they consistently exceed those measured from the experiments, though the difference is roughly 6% or less. This difference can be attributed to the effect of film material in the experiments. The film material provides a very strong acoustic impedance mismatch on the bubble surface, so that some portion of the shock wave impulse is transferred to reflected shock waves, as well as to the atomization process. Shock waves of this type – reflected from helium-filled soap bubbles in air – were also observed by Haas and Sturtevant [21]; however, their strength and their influence on the subsequent development of the flow field are only inferred here. Measurements of these effects are not provided here or elsewhere, and are left for future work. Despite these effects, the agreement between measured, simulated, and modeled vortex ring velocities indicated in Fig. 65 and Table 3 is remarkable.

Table 4 shows the measured non-dimensionalized vortex ring velocity,V_v/u_1', for the high Atwood number convergent-geometry shock-bubble interactions. Both, the Picone-Boris and Rudinger-Somers velocity models fail to provide a reliable prediction for the experimentally measured velocity. In all three cases, the Picone-Boris model overestimates the vortex velocity by roughly 5% or more, whereas the Rudinger-Somer model underestimates it by roughly 10%. It can be noted from Tables 2-4, that for a constant Mach number ($M \approx 2.0$ cases), the vortex ring velocity ratio decreases with an increase in Atwood number. This suggests that for a fixed Mach number, the circulation associated with the primary vortex ring increases in strength with an increase in the Atwood number.

Gas pair	M	A	V_v/u_1' Experiment	V_v/u_1' PB model	V_v/u_1' RS model
R22-N_2	2.03	0.516	0.74	0.868	0.675
SF_6-N_2	2.07	0.681	0.63	0.785	0.623
SF_6-N_2	2.94	0.681	0.74	0.778	0.611

Table 4: Normalized vortex velocity, measured in experiments, and predicted by the Picone-Boris (PB) and Rudinger-Somers (RS) models for high Atwood number, convergent-geometry, shock-bubble interactions. In the experiments, the value is computed as a mean of the velocities for $2tu_1'/D > 8.0$.

5.2 Geometrical Length Scales

The most readily obtainable quantities from the experimental images of a shocked bubble are the axial (height) and lateral (width) extent of the bubble. Figure 66 shows four relevant length scales of the shocked heavy bubble: w is the maximum width, h is the maximum height, D_v is the major diameter of the vortex ring, and d_v is the minor diameter of the vortex ring. Figure 67 is a drawing of the relevant length scales of the shocked light bubble at different phases of the evolution. In the analysis, the length scales are non-dimensionalized by the initial bubble diameter for both heavy and light bubbles, *e.g.* L_h=h/D. The time is non-dimensionalized as, $\tau = t/t'$. The characteristic time $t' = D/(2W_t)$, is defined as the cloud crushing time, where D is initial diameter of the bubble and W_t is the transmitted shock wave velocity in the bubble.

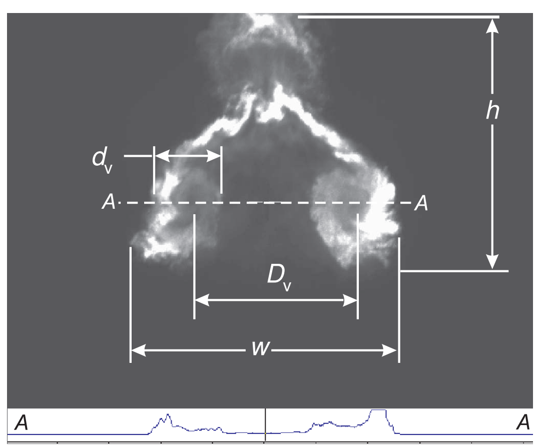

Figure 66: Geometrical length scales for a heavy bubble.

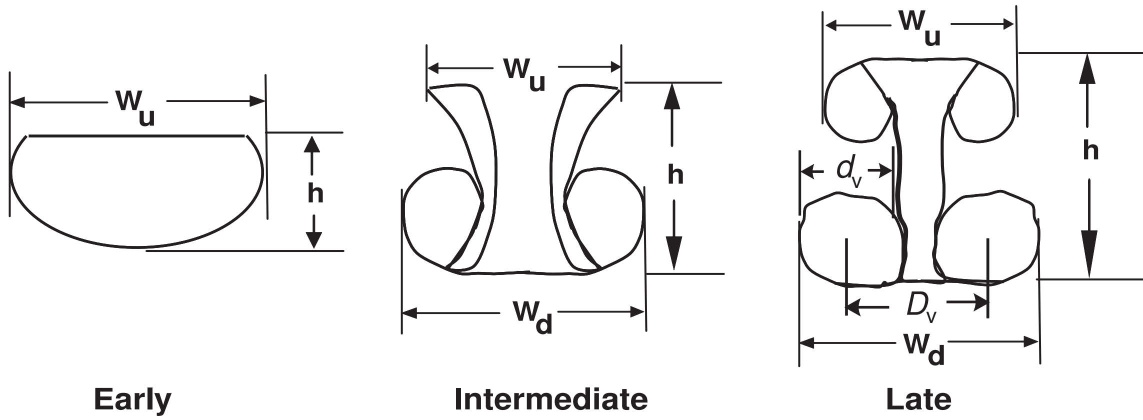

Figure 67: Geometrical length scales for a light bubble at the different phases of evolution.

5.2.1 Convergent-geometry: argon bubble scenarios

Figure 68 shows the width, height, and vortex size measurements for an Ar bubble in N_2, accelerated by a $M = 2.88$ shock wave. Three temporal regions of interest are observed, separated with the dashed vertical lines on the plots: region 1 is the compression zone ($0 < \tau < 7.5$); region 2 is the vortex-pair-induced mixing zone ($7.5 < \tau < 18.0$); and region 3 is the highly turbulent mixing zone ($\tau > 18$). The earliest post-shock picture shows an initial flattening of the bubble caused by the compression of the shock wave. From the height plot (Fig. 68*b*) the compression is observed taking place until τ=7.5, after which, L_h starts to grow. This axial compression is accompanied by a transverse spreading, as observed in the width plot (Fig. 68*a*) where L_w has reached a local maximum. Near τ=10 the width suddenly decreases due to the shock wave reflected from the shock tube side walls which originated when the incident shock wave reflected off the surface of the bubble. The influence of the shock tube walls on w was discussed previously in a numerical study of a weakly shocked bubble [55]. The vortex

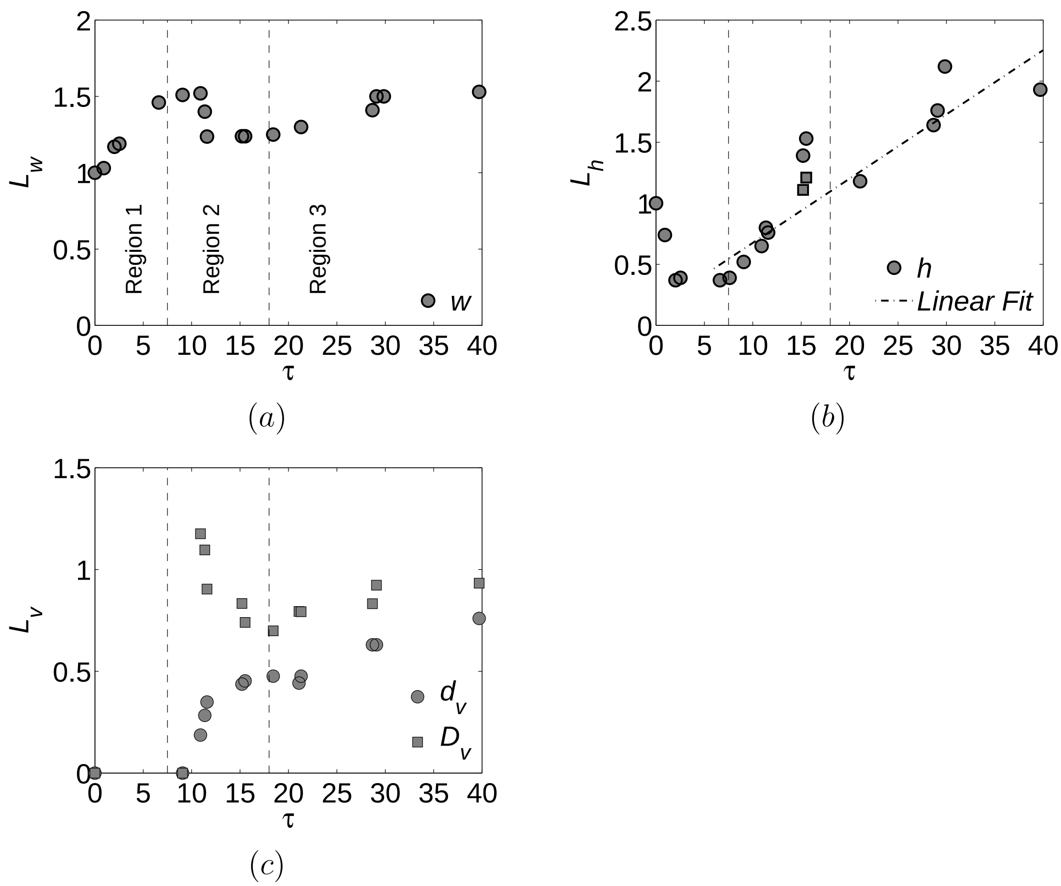

Figure 68: Non-dimensional length scales of an argon bubble accelerated by an $M = 2.88$ shock wave as functions of non-dimensional time: (a) width, (b) height, and (c) vortex dimensions.

formation begins at τ=9.0 (Fig. 68c) in region 2 where the height is increasing rapidly and the width, which has reached a plateau, decreases. The formation of the vortex ring enhances the mixing and this is evident in the rapid increase in the core diameter (minor diameter of the vortex ring).

The width, which increased during the compression region, decreases and reaches a second plateau at $L_w \approx$1.25. The height, however, continues to increase within $7.5 < \tau < 16$ and then decreases for $16 < \tau < 18.5$. The reason for the measured decrease of the height is the suction of the tail of the vortex inside the vortex ring. The data points denoted by square symbols represent the height of the bubble excluding the tail of the vortex ring. The tail swirl inside the vortex ring leads to entrainment of the surrounding N_2 gas into the vortex ring. Later in time, this leads to the splitting of the vortex rings and then the experiment enters a phase of highly turbulent mixing. During this phase the width begins to increase at a constant rate. Further experiments are needed at later times to determine if this growth continues or reaches an asymptotic value. Also in this region the L_h and L_v curves appear to begin a constant growth phase, and the height (L_h) of the bubble grows linearly (after the compression phase) and the rate of the axial elongation ($\alpha = dL_h/d\tau$) of the bubble is measured to be $\alpha = 0.051$.

Figure 69 shows a comparison between the growth trends for $M = 2.88$ and $M = 3.38$ shocked Ar bubbles in N_2 with computational data obtained from *Raptor* also included. Computational and experimental results show good agreement for the height during the compression phase of the bubble, although experimental results show higher lateral growth rates. After $\tau \approx 10$, the effect of shock reflections from the shock tube side walls can be seen on the transverse growth plot in Fig. 69(b). In the simulations, this halts the lateral growth; whereas, in the experiments, it dramatically decreases the bubble width

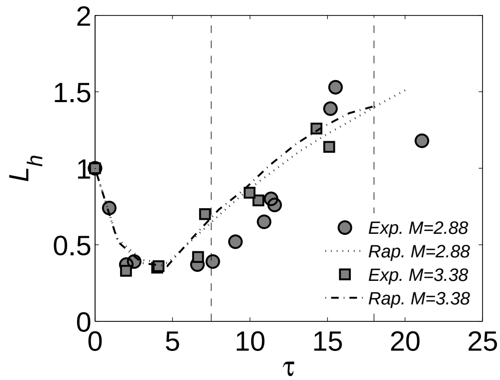

(a)

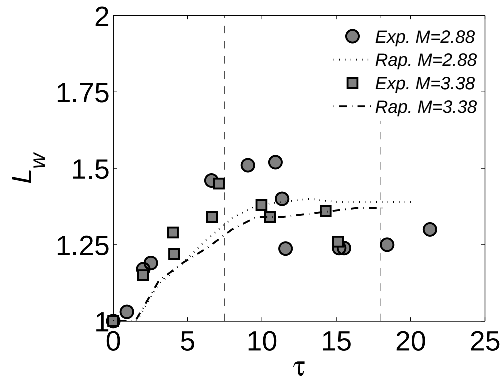

(b)

Figure 69: Comparison between non-dimensional growth trends for shocked Ar bubble in N_2, $M = 2.88, 3.38$: (a) height, and (b) width.

as discussed before. In the axial growth trend shown in Fig. 69(a), the re-expansion effect is stronger in the simulations.

Figure 70 shows the growth trends for a $M = 1.33$ shocked Ar bubble. The axial growth trends plotted in Fig. 70(a) indicate the compression of the bubble for $\tau < 10$, while the transverse growth trends shown in Fig. 70(b) reflect a corresponding lateral expansion. Figure 70(a) again shows that the re-expansion effect is stronger in the simulation. The height (L_h) of the bubble grows linearly after the compression phase, and the rate of the axial elongation $(\alpha = dL_h/d\tau)$ of the bubble is measured to be $\alpha = 0.027$. The observed difference in the rate of the elongation between higher and lower Mach number experiments can be attributed to the formation of the secondary vortex ring in higher Mach number scenarios.

Figure 71 shows the growth trends for a $M = 2.03$ shocked Ar bubble. The growth trends are similar to the other Mach numbers described above. The rate of axial elongation of the bubble is measured to be $\alpha = 0.028$. Figure 72 highlights the comparison

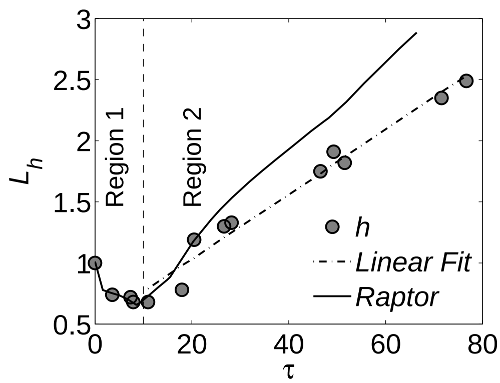

(a)

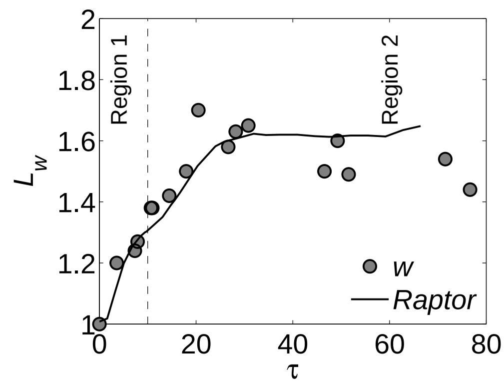

(b)

Figure 70: Non-dimensional growth trends for shocked Ar bubble in N_2, $M = 1.33$: (a) height, and (b) width.

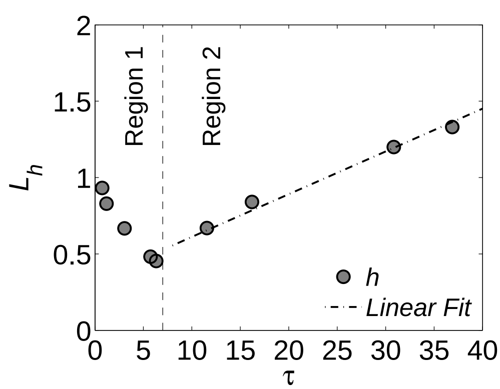

(a)

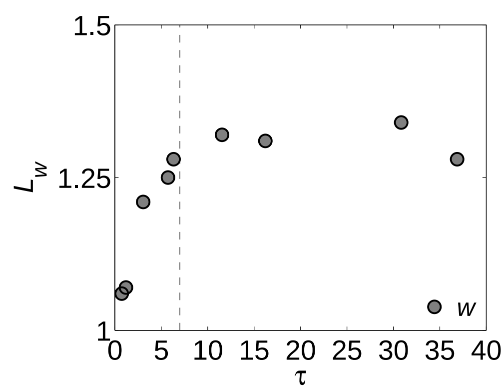

(b)

Figure 71: Non-dimensional growth trends for shocked Ar bubble in N_2, $M = 2.03$: (a) height, and (b) width.

between the growth trends for the $M = 1.33$ and $M = 2.03$ experiments. Figure 72 (a) shows that the axial compression effect is stronger in the case of the $M = 2.03$ experiments although, the rate of elongation is same for both cases. Surprisingly, the lateral growth is higher in the case of the $M = 1.33$ experiments. This observed difference can be attributed to the strength of the shock waves reflected off the shock tube side walls. In the case of the low- Mach- number experiments, the reflected waves are very weak, and hence, the lateral extent of bubble continues to grow in time.

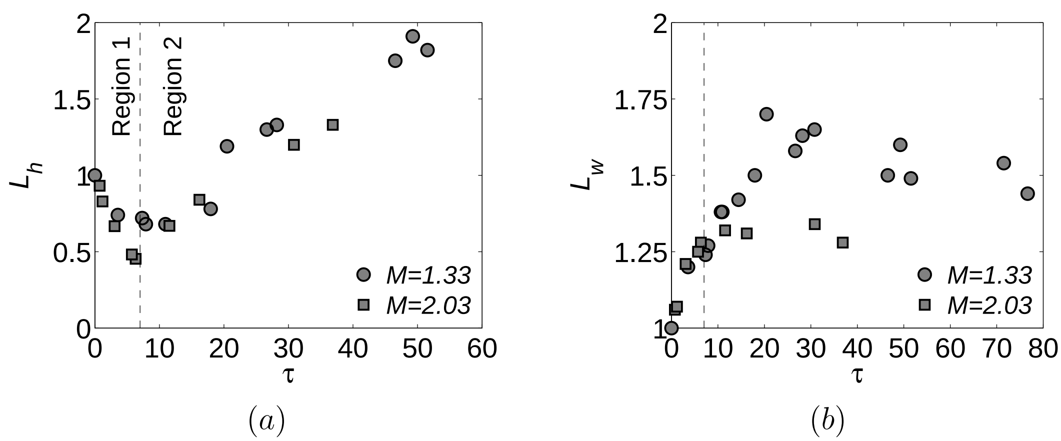

Figure 72: Comparison between non-dimensional growth trends for shocked Ar bubble in N_2, $M = 1.33, 2.03$: (a) height, and (b) width.

Table 5 summarizes the results discussed so far for the shocked argon bubble. The minimum expected value for L_h is estimated from the conservation of mass as $(L_h)_{min} = (W_i - u_1')/W_i$. The minimum axial dimension reached by the bubble during the experiment varies significantly with the Mach number. The experimental values of the $(L_h)_{min}$ are significantly higher compared to the theoretical value for $M > 2.0$. In general, for $M > 2.0$, the minimum axial dimension reached by the bubble is $1.3(W_i - u_1')/W_i$. The rate of axial elongation significantly increases for $M > 2.03$, suggesting some sort of transition for $M > 2.03$. It is thought that at Mach numbers where the flow speed of the shocked ambient gas becomes supersonic (for a shock wave in nitrogen at atmospheric temperature this occurs at $M = 2.07$), there are compressibility effects that may alter the growth of the bubble. Although the data suggest this is probably the case, it is still premature to make a definite conclusion.

M	W_i [m/s]	u'_1 [m/s]	Theoretical $(L_h)_{min}$	Experimental $(L_h)_{min}$	Asymptotic width $(L_w)_{stab}$	Axial Growth $\alpha = dL_h/d\tau$
1.33	469.4	170.1	0.64	0.68	1.5	0.027
2.03	716.5	452.4	0.37	0.48	1.3	0.028
2.88	1016.5	745.2	0.27	0.37	1.5	0.053
3.38	1192.9	907.5	0.24	0.33	1.4	0.067

Table 5: Experimental result overview for a shocked Ar bubble in N_2. M and W_i represents the Mach number and speed of the incident shock wave respectively. u'_1 represent the flow speed of the shocked ambient gas.

Although the dimensionless timescale for growth measurements used thus far is based on the transmitted shock wave speed, a number of other timescales were also tested. Figure 73 shows the temporal evolution of the axial dimension of the shocked bubble for $1.33 \leq M \leq 3.38$, plotted on three different dimensionless timescales. In Fig. 73(a) the dimensionless timescale is based on the transmitted shock wave speed W_t and in Figs. 73(b) and 73(c), the incident shock wave speed W_i, and the flow speed of the shocked ambient gas u'_1 are utilized respectively, to calculate the dimensionless timescales. None of the timescales displayed a collapse of the bubble dimension data to a single trend for all M. This may be considered a shortcoming of the dimensionless timescales discussed so far, or a lack of self similarity behavior over the Mach number regime considered here.

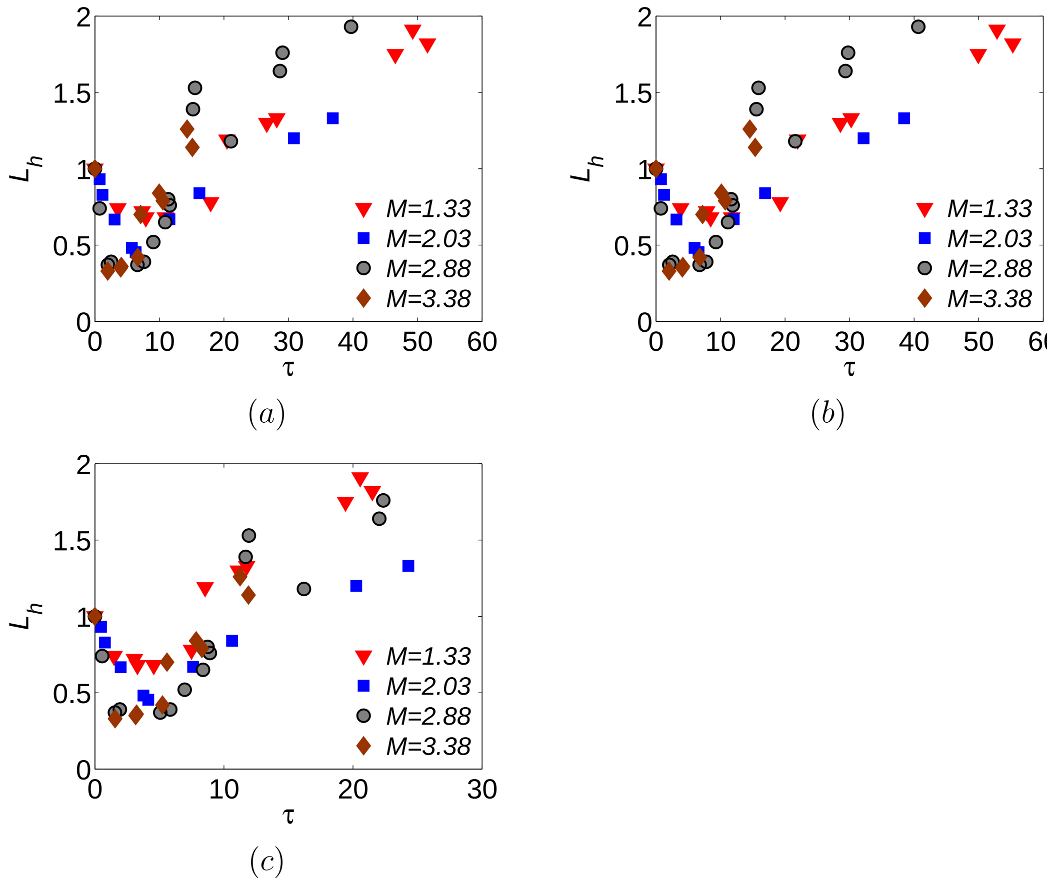

Figure 73: Axial dimension of a shocked Ar bubble in N_2, for $1.33 \leq M \leq 3.38$, plotted on a non-dimensional timescale. The time is non-dimensionalized as $\tau = t/t'$; where (a) $t' = D/(2W_t)$, (b) $t' = D/(2W_i)$, and (c) $t' = D/(2u_1')$.

5.2.2 Divergent-geometry: Helium bubble scenarios

Figures 74-75 show the evolution of the axial (height) and lateral (width) extents of a shocked helium bubble. Four regions of interest have been labeled on the width plot separated by vertical dashed lines to facilitate the description of the evolution. The earliest post-shock images show an initial flattening of the bubble caused by compression due to shock interaction. The height plot in Fig. 74(b) shows compression taking place until τ=4.0. The transverse spreading associated with the initial flattening can be observed in region 1 of the width plot, Figure 74(a), where L_{w_u} reaches a local maximum. This early phase of evolution up to τ=7.0 is denoted as region 1. Similar growth trends for the lateral and axial extents of the bubble are observed in Fig. 75(a)-(b) for the low-Mach-number scenario during region 1.

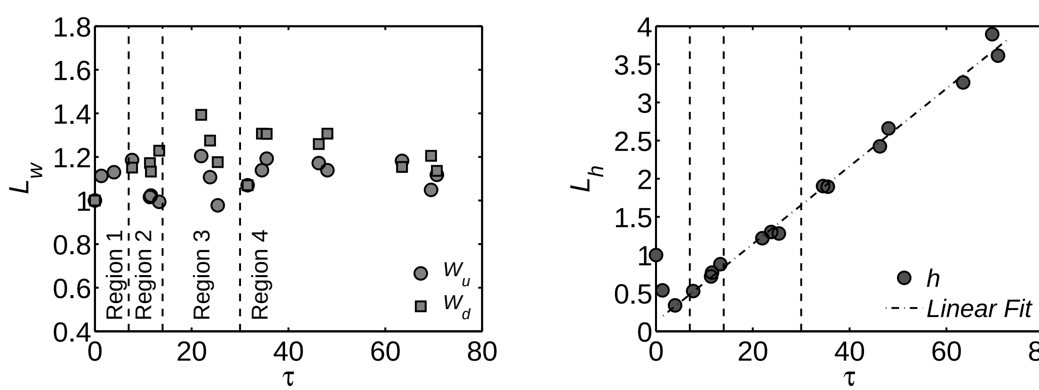

(a) (b)

Figure 74: Non-dimensional length scales of a helium bubble accelerated by a $M = 2.95$ shock as functions of non-dimensional time: (a) width , and (b) height.

The next phase of the bubble evolution, region 2, sees the mass transfer from the body of the bubble to the primary vortex ring (PVR) occurring. This can be clearly seen in the width plot (Fig. 75a) where L_{w_u} starts decreasing with an increase in L_{w_d}.

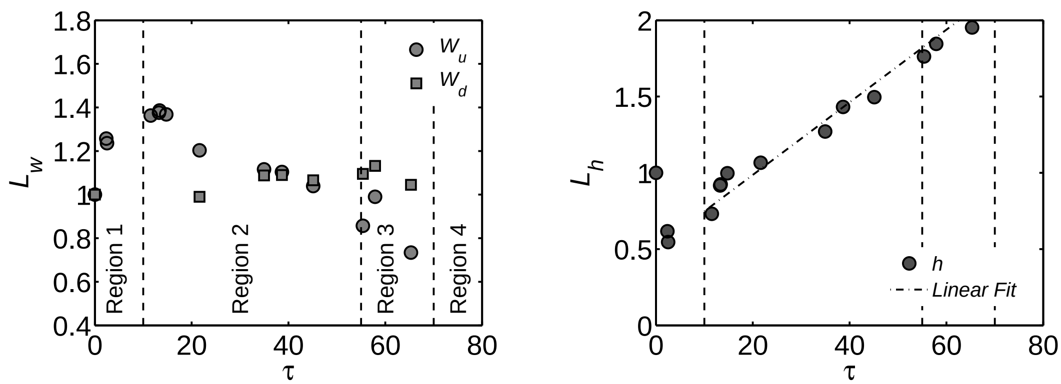

(*a*) (*b*)

Figure 75: Non-dimensional length scales of a helium bubble accelerated by a $M = 1.45$ shock as functions of non-dimensional time: (a) width , and (b) height.

The second phase (region 2) of the shocked bubble evolution is of much shorter duration in the $M = 2.95$ case (see Fig. 74a), which suggests that the primary vortex ring is much stronger in high- Mach- number scenario. The height grows linearly after the compression phase, and the rate of axial elongation ($\alpha = dL_h/d\tau$) of the bubble for the $M = 2.95$ case is measured to be α= 0.051. The rate of axial elongation (α) of the bubble for the $M = 1.45$ case is measured to be α= 0.024. This difference can be attributed to the higher shock strength. It may be noted that the particle velocity behind the shock wave, in the case of $M = 2.95$ experiments, is supersonic while in the case of low-M experiments it is subsonic. The observed difference in the rate of axial elongation, supports the argument that compressibility effects play an important role in the shocked flows when the particle velocity behind the shock becomes supersonic. Following region 2, a sudden decrease is observed in L_w, due to the shock wave reflected from the shock tube side walls which originated when the incident shock wave was reflected off the surface of the bubble (this can be attributed to the presence of the soap film). Finally, in region 4, L_w reaches a plateau at late times.

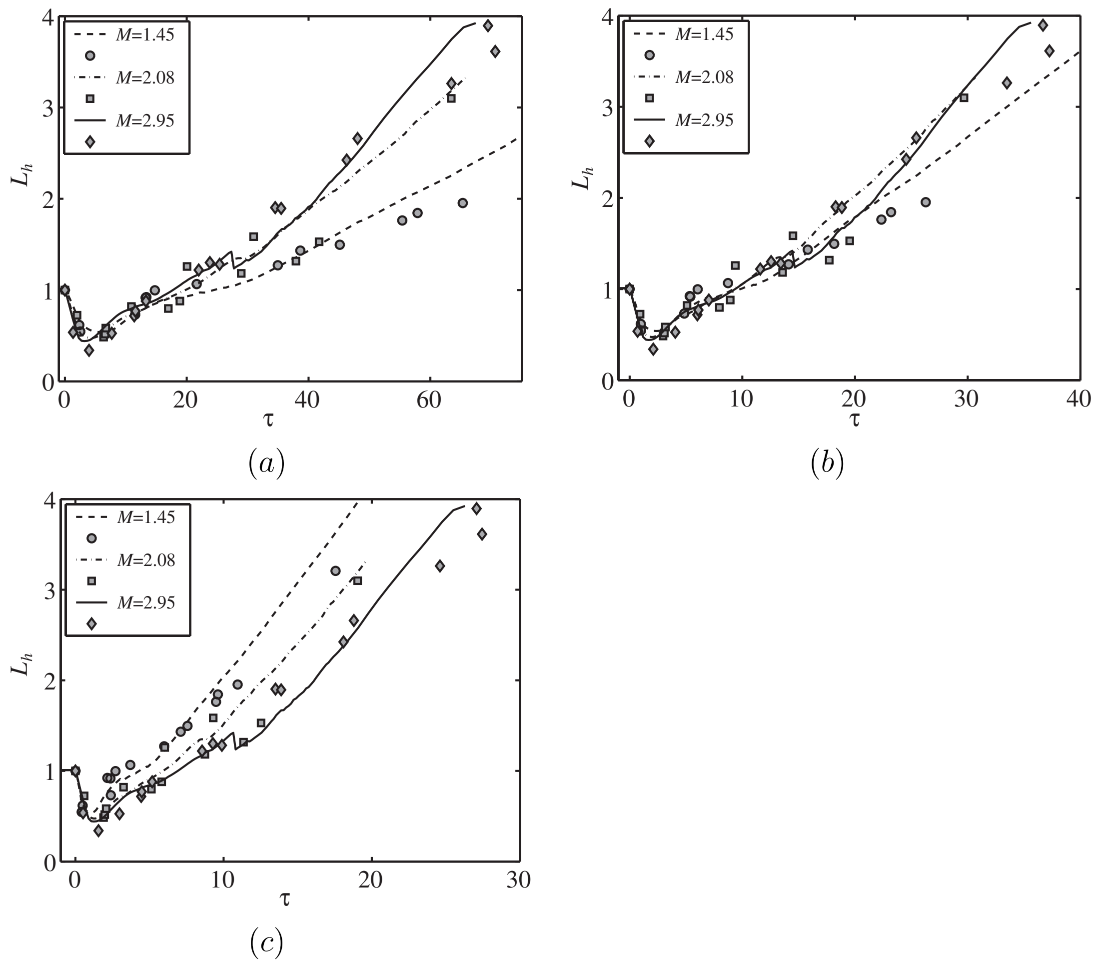

Figure 76: Axial dimension of a shocked helium bubble for $1.45 \leq M \leq 2.95$, plotted on a non-dimensional timescale. The time is non-dimensionalized as $\tau = t/t'$; where (a) $t' = D/(2W_t)$, (b) $t' = D/(2W_i)$, and (c) $t' = D/(2u_1')$. Symbols represent experimental data; lines represent *Raptor* simulation results.

The experimental results obtained here are also compared to their numerical counterparts. The experimental and numerical data are plotted on a series of dimensionless timescales in Figs. 76-77. Comparing the axial dimension trends for timescales based on various characteristic velocity scales, we see that, for these scenarios, a timescale based on the incident shock wave speed W_i as a characteristic velocity (Fig. 76*b*) yields the closest approach to a self-similar growth trend by collapsing the data for $\tau < 20$. Such a conclusion is justified by the observation that: the speed of the incident shock wave, not the transmitted shock wave or the shocked ambient flow, sets the speed with which the slip surface and secondary vortex ring (SVR) are generated in the flow field; and the separation of the SVR from the PVR is the primary agent of the elongation seen after the compression phase in the trends, for $M > 2$. It can also be noted from these plots that the *Raptor* simulations capture the evolution in the axial dimension of the bubble with good accuracy, although the agreement deteriorates at later times, particularly for the low-Mach-number scenarios. Table 6 presents a summary of the axial compression observed in the case of the shocked helium bubble. The experimental values of the $(L_h)_{min}$ are significantly higher compared to the theoretical value for $M > 2.0$. In general, for $M > 2.0$, the minimum axial dimension reached by the bubble is $1.3(W_i - u_1')/W_i$, which was also observed for the heavy Ar bubble scenarios.

M	W_i [m/s]	u_1' [m/s]	Theoretical $(L_h)_{min}$	Experimental $(L_h)_{min}$
1.45	503.3	220.0	0.56	0.55
2.08	721.9	462.7	0.36	0.48
2.95	1042.0	768.2	0.26	0.34

Table 6: Experimental result overview for a shocked He bubble in air or N_2. M, W_i and u_1' represent the Mach number, speed of the incident shock wave and flow speed of the shocked ambient gas respectively.

The evolution of the lateral dimension of the shocked bubble is also compared to the *Raptor* simulations as shown in Fig. 77. In the simulation, the maximum diametral dimension is tracked for the bubble. Therefore the experimental data shown in Fig. 77,

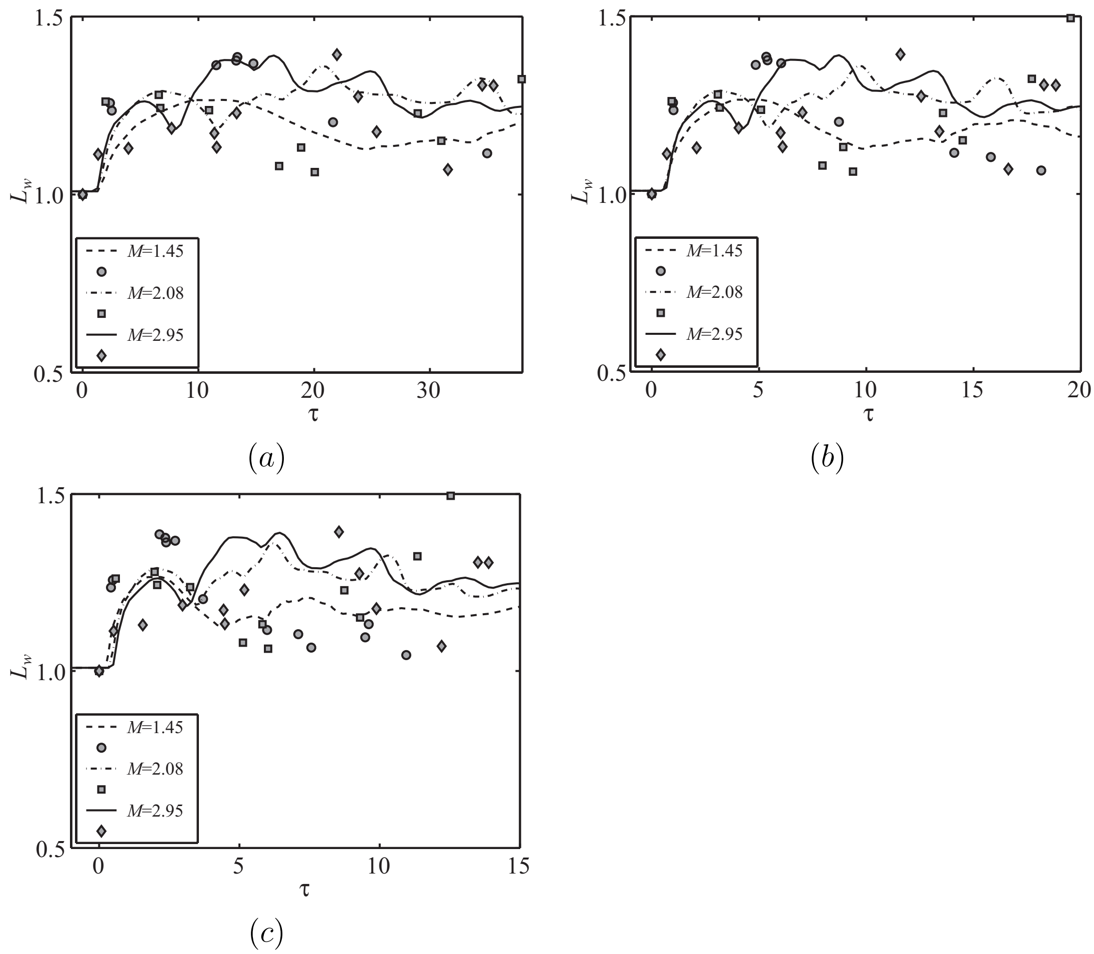

Figure 77: Lateral dimension of a shocked helium bubble for $1.45 \leq M \leq 2.95$, plotted on a non-dimensional timescale. The time is non-dimensionalized as $\tau = t/t'$; where (a) $t' = D/(2W_t)$, (b) $t' = D/(2W_i)$, and (c) $t' = D/(2u_1')$. Symbols represent experimental data; lines represent *Raptor* simulation results.

denotes either w_u or w_d, depending upon whichever is maximum. The lateral dimensions grow as vortices form around the bubble, but remain at a relatively constant level subsequently, with some oscillations due to secondary shock waves and the rotation of material around the vortices. Here we see that although the trends in the axial dimension of the bubble scale according to a characteristic timescale based on W_i, trends in the lateral dimension collapse to a near self-similar trend (for early times) only on a timescale based on u_1', the post-shock ambient flow speed as shown in Fig. 77(c). Comparison between experimental and numerical data in Fig. 77 indicates a much stronger lateral growth at early times for $M = 1.45$ experiments than is found in simulations, though the early-time agreement is improved for higher Mach numbers. At late times, the experimental data do not show a clear trend, however, both experiment and numerical results indicate that the lateral extent of the shocked bubble does not exceed $1.5D$.

5.2.3 Convergent-geometry: $M \approx 2.0$ scenarios

Here, we measure the axial and transverse dimension of the shocked bubble for a fixed M in order to determine the effect of Atwood number on the growth trends. The temporal evolution of the axial (height) and lateral (width) extents of the $M \approx 2.03$ shocked bubble, for the Atwood number range $0.17 \leq A \leq 0.68$, are plotted on a series of dimensionless timescales in Figs. 78-79. The axial dimension of the bubble goes through a minimum during the shock-compression phase, and then grows at a nearly constant rate until very late times. Comparing the trends for timescales, based on different characteristic velocities, we see that, for these scenarios, a timescale based on the W_i, shown in Fig. 78(b), yields the closest approach to self-similar trend by collapsing the data for $A > 0.5$ cases. Figure 78 indicates much stronger axial growth for higher

Atwood numbers, although at early-times, the minimum axial dimension reached by the bubble is roughly the same for all the scenarios. This difference can be attributed to the complex field of secondary shock waves generated due to shock focusing in the case of high Atwood number flows. Regions of intense mixing develop in the flow field which significantly increase the axial growth of the bubble. For higher Atwood number cases, the lateral dimension of the bubble shows a stairstep growth profile. In Fig. 79(c), a dramatic drop in the lateral dimension of bubble, even below the initial value, is evident for the $A > 0.5$ cases. Such behavior has not been seen in any other scenarios. The width of the bubble reaches a plateau by $\tau \approx 8.0$, and again starts to increase by $\tau \approx 20$. It finally reaches a second plateau by $\tau \approx 25$, and subsequently remains at a relatively constant level.

Comparing the trends for timescales, based on different characteristic velocities, we saw that, for these scenarios, the Atwood number has a significant effect on the axial growth rate of the bubble. Therefore, a new non-dimensional timescale is built which includes the Atwood number (A) in its formulation. The new non-dimensional timescale is given as $\tau = t/t'$, where $t' = D/(2W_i A^p)$. At this time, there is no physical justification for choosing the exponent of A. Different values of p were tested, and we found that $p = 0.95$, provided the best fit to the experimental data for the post shock compression phase. The axial elongation rates of the bubble for various values of p are presented in Tab. 7. Figure 80(a) shows the temporal evolution of the axial dimension of the bubble based on this new timescale for $p = 0.95$. We see that this new timescale yields a self-similar growth trend for the axial dimension of the bubble, however, the lateral dimension resembles a self-similar growth trend only for $5 \leq \tau \leq 10$. Although the data suggest this is probably a very good scaling law, it is still premature to make a definite

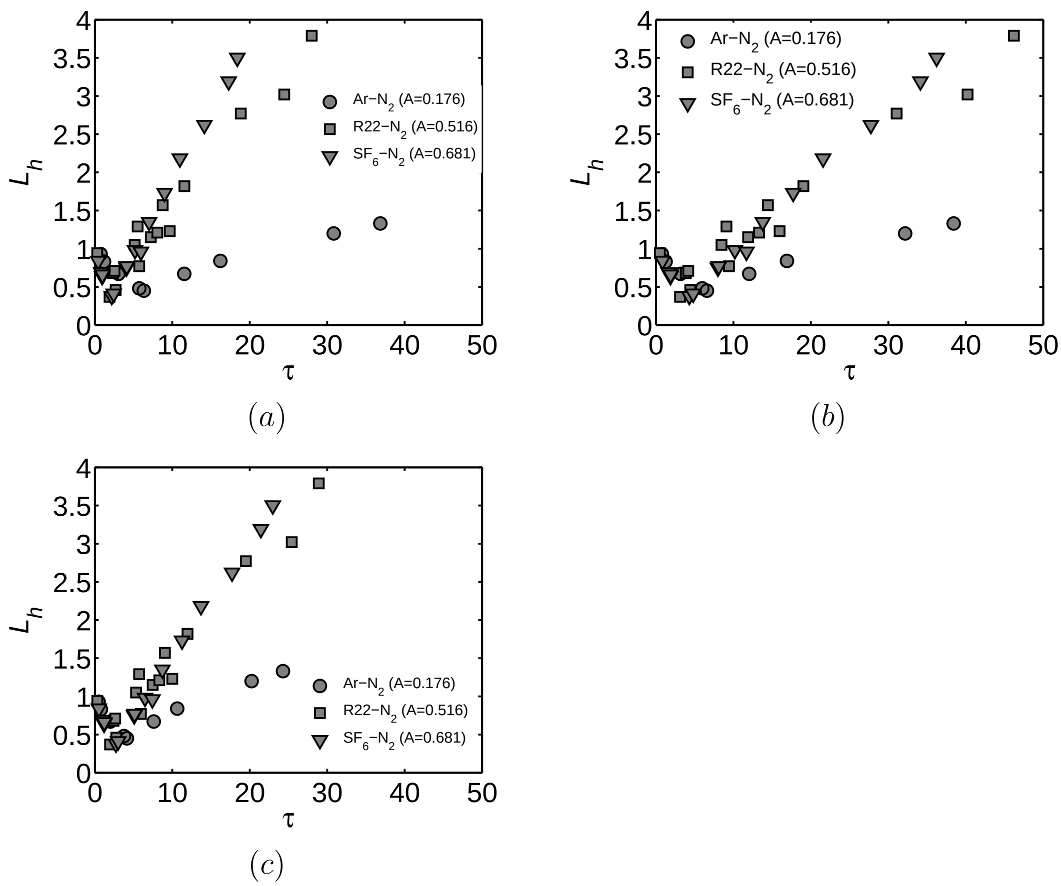

Figure 78: Axial dimension of a shocked heavy gas bubble ($0.17 \leq A \leq 0.68$) for $M \approx 2.03$, plotted on a non-dimensional timescale. The time is non-dimensionalized as $\tau = t/t'$; where (a) $t' = D/(2W_t)$, (b) $t' = D/(2W_i)$, and (c) $t' = D/(2u_1')$.

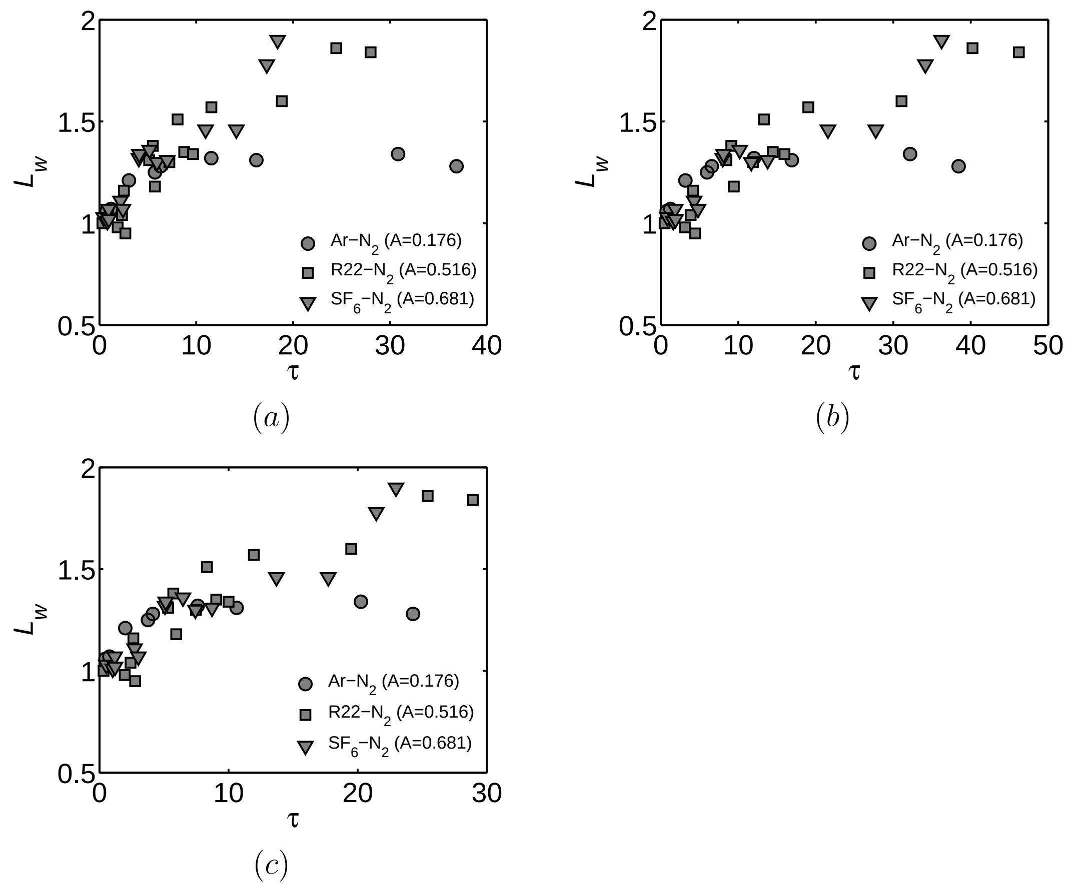

Figure 79: Lateral dimension of a shocked heavy gas bubble ($0.17 \leq A \leq 0.68$) for $M \approx 2.03$, plotted on a non-dimensional timescale. The time is non-dimensionalized as $\tau = t/t'$; where (a) $t' = D/(2W_t)$, (b) $t' = D/(2W_i)$, and (c) $t' = D/(2u_1')$.

Gases	M	A	$\alpha = \frac{dL_h}{d\tau}$ $p = 0.8$	$\alpha = \frac{dL_h}{d\tau}$ $p = 0.9$	$\alpha = \frac{dL_h}{d\tau}$ $p = 0.95$	$\alpha = \frac{dL_h}{d\tau}$ $p = 1.0$	$\alpha = \frac{dL_h}{d\tau}$ $p = 1.1$
Ar-N_2	2.03	0.176	0.1074	0.1277	**0.1393**	0.1520	0.1808
R22-N_2	2.03	0.516	0.1249	0.1344	**0.1379**	0.1425	0.1523
SF_6-N_2	2.07	0.681	0.1314	0.1366	**0.1392**	0.1419	0.1475

Table 7: Axial growth rate ($\alpha = dL_h/d\tau$) for different values of p. The non-dimensional timescale is given as $\tau = t/t'$, where $t' = D/(2W_iA^p)$.

conclusion here. Therefore, this remains a subject for future work.

5.3 Circulation

The method by which shock-bubble interactions have most commonly been understood and analyzed is by the means of the circulation. The circulation quantifies the net strength of the vortex rings generated by the shock-bubble interactions. For this reason, it has been the subject of a number of analytical models with various conceptual bases as discussed in Sec. 2.6. Circulation models proposed by three sets of authors are considered here: Picone and Boris (PB) [51, 52]; Yang, Kubota, and Zukoski (YKZ) [72]; and Samtaney and Zabusky (SZ) [64, 74]. Each of these models predicts the total circulation in the flow field after the shock wave passage through the bubble.

In the PB and YKZ models, Eq. 2.18 is utilized to obtain the circulation in one half of the bubble, with the only source term for the vorticity being the baroclinic term. In our notation, the PB model, is given by

$$\Gamma_{\mathrm{PB}} \approx 2u_1' \left(1 - \frac{u_1'}{2W_i}\right) \left(\frac{D}{2}\right) \ln\left(\frac{\rho_1}{\rho_2}\right), \tag{5.1}$$

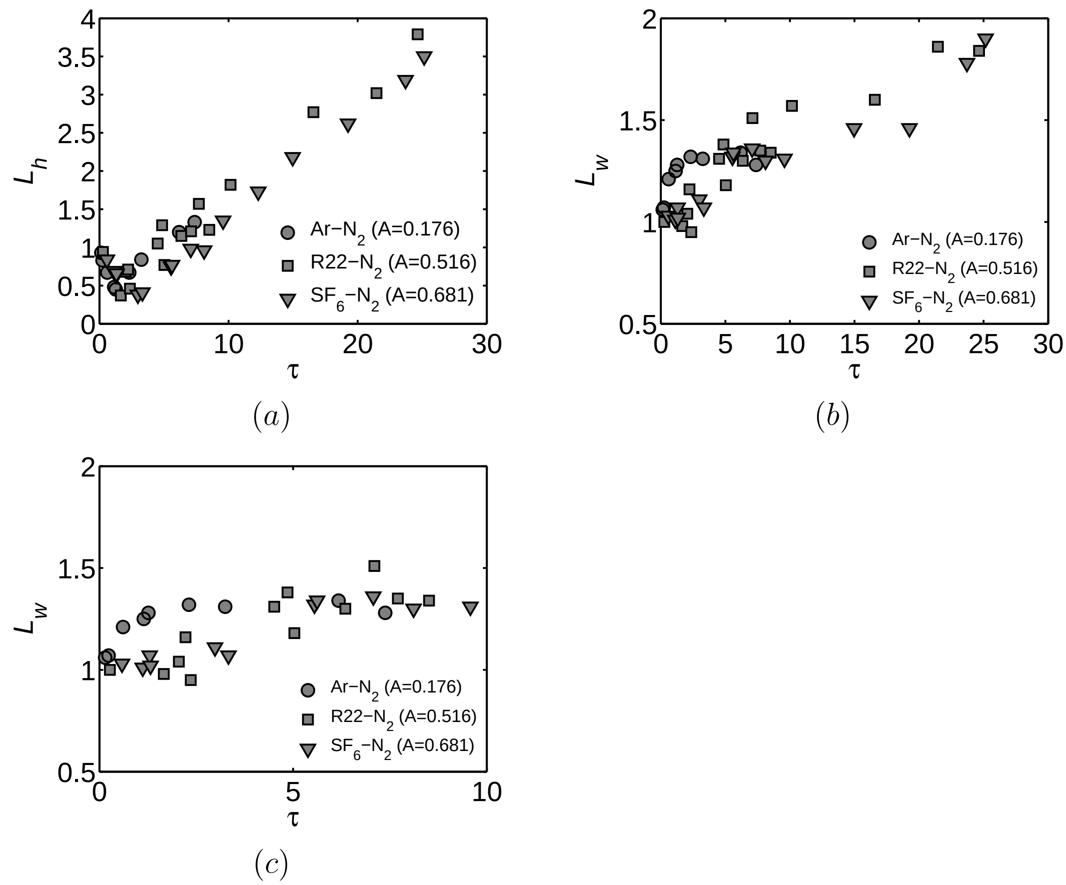

Figure 80: Non-dimensional length scales of a shocked heavy gas bubble ($0.17 \leq A \leq 0.68$) for $M \approx 2.03$, plotted on a non-dimensional timescale given as $\tau = t/t'$, where $t' = D/(2W_i A^p)$. (a) Axial dimension, (b) lateral dimension and (c) zoomed view of lateral dimension for $0 \leq \tau \leq 10$.

and the YKZ model by

$$\Gamma_{\text{YKZ}} \approx \frac{2D}{W_i}\frac{p_1' - p_1}{\rho_1'}\left(\frac{\rho_2 - \rho_1}{\rho_2 + \rho_1}\right). \tag{5.2}$$

Samtaney and Zabusky produced an in-depth analysis of the baroclinic vorticity deposition on a planar interface using shock polar analysis and extended it to the spherical case using a "near-normality" condition. Recently, for the case of $0 < A < 0.2$, Niederhaus *et al.* [48] observed that the "near-normality" condition does not hold, and suggested a minor modification to the model. This yields the following formula for the circulation:

$$\Gamma_{\text{SZ}} = \begin{cases} \left(\frac{4}{1+\gamma}\right)\left(1 - \chi^{-\frac{1}{2}}\right)\left(1 + M^{-1} + 2M^{-2}\right)(M-1)(D/2)\,c_1, & 0 < A < 0.2 \\ \left(1 + \frac{\pi}{2}\right)\left(\frac{2}{1+\gamma}\right)\left(1 - \chi^{-\frac{1}{2}}\right)\left(1 + M^{-1} + 2M^{-2}\right)(M-1)(D/2)\,c_1, & A \geq 0.2 \end{cases}, \tag{5.3}$$

where the dimensionless scaling law (equation 5.15 of SZ) has been multiplied by the ratio $c_1/\gamma^{\frac{1}{2}}$, in order to obtain the circulation in physical units.

In order to obtain the circulation from experimental data here, Kelvin's vortex model is used, following the method of Haas and Sturtevant [21]. The Kelvin formula [34, 63] for the velocity of a moving vortex ring of major diameter D_v and minor diameter d_v is given as :

$$U = \frac{\Gamma}{2\pi D_v}\left[\ln\left(\frac{8D_v}{d_v}\right) - \frac{1}{4} + \wr\left(\frac{d_v}{D_v}\right)\right], \tag{5.4}$$

where Γ is the circulation about the ring. Moore in 1985 [63], presented a modified version of Kelvin's vortex model for the propagation speed of a uniform vortex ring in a compressible fluid to lowest order in the Mach number given as

$$U = \frac{\Gamma}{2\pi D_v}\left[\ln\left(\frac{8D_v}{d_v}\right) - \frac{1}{4} - \left(\frac{5M_v^2}{12}\right)\right], \tag{5.5}$$

where $M_v = U/c_1$ is the translational Mach number of the vortex ring. In our experiments the velocity defect $U = V_v - u_1'$, and the major and minor diameters of the vortex ring are known. Therefore the circulation associated with a vortex ring can be estimated using the Kelvin's (Γ_K) and Moore's (Γ_M) formula as

$$\Gamma^{\mathrm{K}} = 2\pi D_v \left(V_v - u_1'\right) \left[\ln\left(\frac{8D_v}{d_v}\right) - \frac{1}{4}\right]^{-1}, \tag{5.6}$$

$$\Gamma^{\mathrm{M}} = 2\pi D_v \left(V_v - u_1'\right) \left[\ln\left(\frac{8D_v}{d_v}\right) - \frac{1}{4} - \left(\frac{5M_v^2}{12}\right)\right]^{-1}. \tag{5.7}$$

This quantitative analysis across a broad parameter space makes the present study useful as a tool for the evaluation of various analytical models. For each scenario, a "mean" circulation is calculated from experiments by averaging over all times $2tW_t/D > 10$ for the convergent-geometry, and $2tW_t/D > 20$ for divergent-geometry shock-bubble interactions. The circulation values in the model and experiments are scaled for a bubble of initial diameter, $D = 0.0381$ m. Comparisons have also been made with the available *Raptor* simulation results.

5.3.1 Divergent-geometry shock-bubble interactions

Experimental results from divergent-geometry shock-bubble interactions are presented in Table 8, along with the predictions of the various analytical models, and the results computed from the *Raptor* simulations. The data shown in Table 8 indicate remarkable agreement between (1) the PVR circulation (Γ_{PVR}) measured from experimental data (through Kelvin/Moore model), (2) that obtained from net integrated vorticity in simulations ($\bar{\Gamma}_0$), and (3) that predicted by the YKZ model (Γ_{YKZ}), except at $M = 1.45$. These results indicate that the YKZ model gives the most accurate prediction of the late-time circulation, long after the initial shock wave transit. The difference between the circulation obtained using Kelvin's and Moore's formula is less than 3%. It can also

Gases	M	$\Gamma^{\mathrm{K}}_{\mathrm{PVR}}$ Exp.	$\Gamma^{\mathrm{M}}_{\mathrm{PVR}}$ Exp.	$\bar{\Gamma}_0$ *Raptor*	$\Gamma^{\mathrm{K}}_{\mathrm{PVR}}$ *Raptor*	Γ_{YKZ} Model	Γ_{PB} Model	$\Gamma^{\mathrm{K}}_{\mathrm{SVR}}$ Exp.	$\Gamma^{\mathrm{K}}_{\mathrm{SVR}}$ *Raptor*
He-air	1.45	4.80	4.83	8.415	8.169	7.058	12.819	–	–
He-air	2.08	9.82	10.01	9.827	12.869	9.472	23.447	–	-2.279
He-N_2	2.95	10.38	10.64	12.366	18.282	11.373	35.504	-2.29	-5.592

Table 8: Mean circulation extracted from experiments and *Raptor* simulations for $2tW_t/D > 20$, and predicted by analytical models for divergent-geometry shock-bubble interactions. $\Gamma^{\mathrm{K}}_{\mathrm{PVR}}$ (Exp.) and $\Gamma^{\mathrm{M}}_{\mathrm{PVR}}$ (Exp.) represent mean experimental values of the circulation calculated using Kelvin's model (Eq. 5.6) and Moore's model (Eq. 5.7), respectively. $\bar{\Gamma}_0$ represents the mean net circulation obtained from simulation using integrated vorticity method, and the values $\Gamma^{\mathrm{K}}_{\mathrm{PVR}}$ (*Raptor*) and $\Gamma^{\mathrm{K}}_{\mathrm{SVR}}$ (*Raptor*) are computed for the circulation values obtained from simulations using Eq. 5.6 (Kelvin's model). Circulation values are given in units of m^2/s.

be noted that, as observed in previous work [72], the PB model overestimates the circulation by a factor of two or more. The extension of Samtaney and Zabusky [64] model for $A < 0$ has not been adapted to circular interfaces successfully, and comparison with this model is therefore omitted here.

5.3.2 Convergent-geometry shock-bubble interactions

Experimental results from convergent-geometry shock-bubble interactions are presented in Table 9, along with the predictions of the various analytical models, and the results computed from the *Raptor* simulations. We note that as we increase the Atwood number, the circulation associated with the vortex ring increases dramatically. For $M \approx 2.03$, the circulation increased seven times by increasing the value of A from 0.176 to 0.681. This difference can be attributed to the strong shock refraction in the case of higher Atwood number scenarios, which leads to a significant difference in the translational velocity of the bubble with respect to the post-shock flow speed. A transition from

Gases	M	A	Γ^{K} Exp.	Γ^{M} Exp.	$\bar{\Gamma}_0$ *Raptor*	Γ_{YKZ} Model	Γ_{PB} Model	Γ_{SZ} Model
Ar-N_2	1.33	0.176	-0.98	-0.98	-1.46	-1.45	-1.74	-1.65
Ar-N_2	2.03	0.176	-1.36	-1.36	—	-2.24	-3.84	-3.52
Ar-N_2	2.88	0.176	-2.02	-2.02	-3.19	-2.67	-4.88	-5.17
Ar-N_2	3.38	0.176	-2.05	-2.05	-3.51	-2.91	-6.23	-6.06
R22-N_2	2.03	0.516	-8.23	-8.34	—	-6.56	-13.57	-13.41
SF_6-N_2	2.07	0.681	-14.06	-14.65	—	-8.75	-20.15	-18.12
SF_6-N_2	2.94	0.681	-17.05	-18.20	—	-10.43	-30.15	-26.48

Table 9: Mean circulation extracted from experiments and *Raptor* simulations for $2tW_t/D > 10$, and predicted by analytical models for convergent-geometry shock-bubble interactions. Γ^{K} (Exp.) and Γ^{M} (Exp.) represent mean experimental values of the circulation calculated using Kelvin's (Eq. 5.6) and Moore's model (Eq. 5.7), respectively. $\bar{\Gamma}_0$ represents the mean net circulation obtained from simulation using integrated vorticity method. Circulation values are given in units of m^2/s.

large-scale coherent structures at low A to fine-scales complex structure at high A was observed in the experiments performed at fixed Mach number discussed in Chapter 4. With the limited data available for comparison, one can see that the *Raptor* simulations overpredict the experimental circulation values by a factor of approximately 1.5. The PB model overpredicts the experimental value by roughly 30% or more at high density contrasts, $A > 0.2$, but drastically overpredicts the circulation by a factor of two or more for $A < 0.2$. The YKZ model performs reliably for $A < 0.2$, with better comparison with increasing Mach number. The SZ model provides a reasonable estimates in general for $A > 0.2$, but it is unrealiable for $A < 0.2$. Overall, the results shown in Tables 8-9 suggest that a consistent and reliable predictive model for the shocked-bubble circulation does not yet exist.

To characterize the turbulence characteristics of the flow, the physical Reynolds number associated with the shock-bubble interactions can be estimated on the basis on

Gas	μ [Kg/m-s]
He	1.993×10^{-5}
N_2	1.768×10^{-5}
Air	1.857×10^{-5}
Ar	2.229×10^{-5}
R22	1.302×10^{-5}
SF_6	1.625×10^{-5}

Table 10: Dynamic viscosities for gases in the present study, obtained from JANAF data [18] at $P_1 = 0.098274$ MPa and $T_1 = 300$ K.

the circulation Γ, as

$$Re_\Gamma = \frac{\Gamma^*}{\nu^*}, \tag{5.8}$$

where Γ^* is a characteristic circulation for the flow, and ν^* is a characteristic kinematic viscosity. If we take Γ^* to be the circulation associated with the primary vortex ring (see Sec. 5.3), and take ν^* to be the weighted average of the two fluids' kinematic viscosities, $\nu^* = (\mu_1 + \mu_2)/(\rho_1 + \rho_2)$, then we obtain the physical Reynolds numbers for the shocked flow field. The dynamic viscosities used to calculate ν^* are shown in Table 10.

Vortex rings generated in the flow can be laminar or turbulent, and their behavior can be explained on the basis of the Reynolds number as shown in Table 11. The circulation-based Reynolds number (Re_Γ) in the experiment is nearly one order of magnitude greater than the mixing-transition Reynolds number identified by Dimotakis [15] as 2×10^4. Therefore, in all of the present scenarios, the flow field is turbulent at late-times. In the case of high-Atwood number high-Mach number experiment, we observed that the shocked bubble is effectively reduced to a small core of compressed fluid, which trails behind a plume-like structure indicative of a well-developed mixing region. Such

Gases	M	A	Γ^* [m^2/s]	ν^* [m^2/s]	Re_Γ	Behavior vortex ring
He-air	1.45	-0.757	4.83	2.809×10^{-5}	1.72×10^5	Turbulent
He-air	2.08	-0.757	10.01	2.809×10^{-5}	3.56×10^5	Turbulent
He-N_2	2.95	-0.750	10.64	5.091×10^{-5}	2.09×10^5	Turbulent
Ar-N_2	1.33	0.176	0.98	1.415×10^{-5}	6.93×10^4	Turbulent
Ar-N_2	2.03	0.176	1.36	1.415×10^{-5}	9.61×10^4	Turbulent
Ar-N_2	2.88	0.176	2.02	1.415×10^{-5}	1.43×10^5	Turbulent
Ar-N_2	3.38	0.176	2.05	1.415×10^{-5}	1.45×10^5	Turbulent
R22-N_2	2.03	0.516	8.34	0.638×10^{-5}	1.31×10^6	Turbulent
SF_6-N_2	2.07	0.681	14.65	0.464×10^{-5}	3.15×10^6	Turbulent
SF_6-N_2	2.94	0.681	18.20	0.464×10^{-5}	3.92×10^6	Turbulent

Table 11: Reynolds number for shock-bubble interaction evaluated using Eq. 5.8. The expected behavior of the vortex ring is characterized on the basis of the Reynolds number.

behavior is justified on the basis of the Reynolds number obtained in these scenarios ($Re_\Gamma > 1.0 \times 10^6$).

5.4 Comparison with Laser-Driven Experiments

Several shock-driven experiments for a spherical inhomogeneity have been carried out successfully at high Mach number ($M \sim 10$) using both the Omega laser at the Laboratory of Laser Energetics [60, 22] and the NOVA laser at LLNL [30, 31]. These experiments have been described briefly in sec. 2.7. Klein *et al.* [31] utilized the NOVA laser to generate a strong shock wave ($M = 10$) which traveled within a miniature beryllium shock tube, 750 μm in diameter, filled with a plastic of density 1.06 g cm^{-3}. Embedded in the plastic was a copper sphere 100 μm in diameter of density 8.9 g cm^{-3}. This corresponds to a convergent-geometry shock-bubble interaction for Atwood number, $A = 0.787$. The incident shock-wave speed is calculated from the paper (Fig.15) to be $W_i = 1.66 \times 10^4$ m/s. In Fig. 81 we show a comparison between the shock tube experiments and laser-driven experiment for the axial dimension of the bubble. The time is non-dimensionalized as as $\tau = t/t'$; where $t' = D/(2W_i A^{0.95})$. We see a remarkable agreement between the laser-driven experiment and the current experiment campaign. The rate of axial elongation in the case of the laser-driven experiments is $\alpha = 0.1423$.

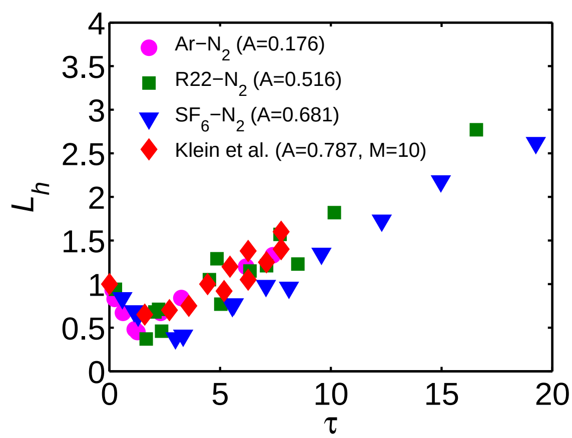

Figure 81: Comparison of the results of the laser-driven shock sphere experiment [31] and the shock tube experiments showing the temporal evolution of the axial dimension of the bubble. The time is non-dimensionalized as $\tau = t/t'$; where $t' = D/(2W_i A^{0.95})$

In 2007, Hansen *et al.* [22] took the Omega experiments a step further by replacing the area radiography technique used by Robey *et al.* [60] with a point-projection radiography technique, and this vastly increased the number of photons that illuminated the shock tube, resulting in a better signal to noise ratio. The images obtained with this technique allowed them to estimate the cloud mass as a function of time. In these experiments they also replaced the copper sphere used previously by other experimenters with an aluminium sphere, to study the faster hydrodynamic evolution, for the lighter material so distortion could be studied for a longer time. Hansen *et al.* [22] showed that the cloud mass as a function of time followed a model of turbulent-mass stripping, strongly suggesting that turbulence plays an important role in the development at late times. They also showed that the cloud distortion (see Fig. 82) compared quantitatively quite well with the shock tube experiments reported by Ranjan *et al.* [56] (the work described in Ranjan *et al.* [56] was performed as a part of this dissertation) for the scaled lengthwise growth of the bubble. The images shown in their paper closely resemble the experimental images obtained here for $A > 0.5$ cases. Since, the value of the incident shock wave speed is not clearly presented in the paper, we will restrict ourself from extending this comparison with the new timescale ($\tau = t/t'$, where $t' = D/(2W_i A^{0.95})$).

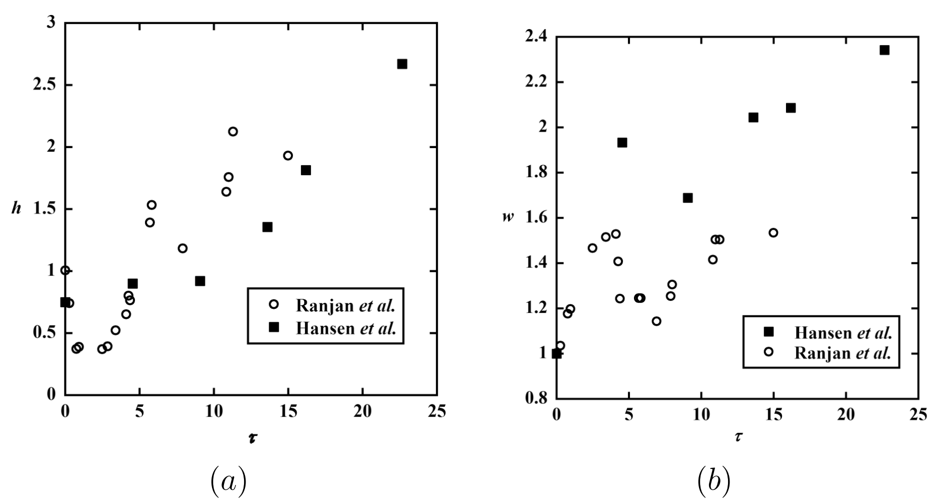

Figure 82: Comparison of the results of the laser-driven shock sphere experiment([22]) and the shock tube experiments showing the temporal evolution of : (a) the axial dimension of the bubble and (b) the lateral dimension of the bubble. The plots shown here are obtained from the published work of Hansen *et al.* [22]. The time is non-dimensionalized as $\tau = t/t'$; where $t' = D/u_1'$

This is still a very encouraging result, as it suggests that the results obtained from this experimental campaign can be extended to study very high- Mach- number experiments, which are beyond the capabilities of mechanical shock tubes.

Chapter 6

Conclusions and Future Work

The experimental study described in this dissertation represents a novel approach for characterizing the shock-bubble interaction problem where the bubble is in free-fall or free-rise before the shock wave arrival, since the flow remains unobstructed by a bubble holder or injector. Planar laser diagnostics have been utilized for the first time to study the evolving flow field, and this technique helped to characterize the vortex rings formed following the shock wave bubble interaction much more distinctly than in previous work obtained using integrated visualization techniques. The imaging system implemented here enabled the capturing of up to five shocked bubble images per run, enhancing the investigation of the evolution of the shocked bubble during a single experiment. For the first time, experiments have been conducted for a wide range of varying Atwood ($-0.8 < A < 0.7$) and Mach numbers ($1.3 < M < 3.5$). Previously, shock tubes have only been utilized to study these instability growth rates at lower shock strengths ($M < 1.5$) where $u_1' < c_1'$; this is the first study of its kind, which intends to connect the hydrodynamic shock instability growth measurements with those conducted in laser-driven shock tubes at higher shock strengths ($M > 10$) where $u_1' > c_1'$. The results have also been analyzed in greater detail to yield quantitative characterizations of the post-shock vortex ring velocity, trends in the streamwise and lateral dimensions of the bubble, and the circulation associated with the vortex rings.

6.1 Bubble Deformation

Qualitatively, the results presented in this dissertation indicate that shock-bubble interactions exhibit patterns of development at low $|A|$ that are fundamentally distinct from those seen at high $|A|$. Because the processes of shock refraction and vorticity generation are nonlinearly coupled via gradients in the density field, and density gradients persist to late times due to secondary shocks, differences in the initial value of A lead to vastly different end states in these flow. Despite the complex couplings, in almost every case in the experimental study, a distinguishable vortex ring core forms in the flow field by $2tW_t/D = 20$, or much sooner in some cases. Such a behavior is expected according to the standard description based on baroclinic vorticity deposition as described in Sec. 2.4.3. The results show that the important large-scale features observed in the flow field experimentally are captured with good accuracy in the three-dimensional numerical simulations performed using *Raptor*. The correspondence between experimental and numerical results improves with increased Mach number ($M > 2$) due to the decreased tracer particle size associated with larger energy deposition on the film layer.

6.1.1 Divergent shock-refraction geometry

In the case of $M > 2$, divergent shock-refraction geometry ($A < 0$) shock-bubble interaction problem, both experimental and numerical flow visualizations exhibit the development of secondary and, in some cases, tertiary vortex rings rotating oppositely to the primary vortex ring. However, the origin of these secondary vortex rings is closely linked to the generation of slip surfaces in the flow field during irregular shock refraction around the bubble at early times, and they appear in experiments and simulations only for incident shock wave Mach numbers $M > 2$. The primary and secondary vortex rings both persist stably to very late times in both experiments and simulations ($2tW_t/D > 100$ in some cases), and strongly contribute to the axial elongation of the shocked bubble in the post-shock flow. This indicates that in a divergent shock-refraction geometry, baroclinically-generated vortical features can be expected to remain an important feature of shock-accelerated inhomogeneous flows long after the passage of the initial shock wave. Inherently three-dimensional vortical features also appear in the simulated flowfields at late times. However, the regions where such features are significant is relatively small for these divergent-shock-refraction scenarios, and the late-time flowfield for these divergent shock-refraction scenarios is in general dominated by large-scale coherent vortical structures.

6.1.2 Convergent shock-refraction geometry: low A

In convergent geometry at low A (the case of Ar-N_2 experiments), a secondary vortex ring is observed at the apex of the bubble in all the four cases; however, it is more prominent in the case of high Mach number experiments ($M > 2.5$). Such a ring was predicted previously for strong shocks by Zabusky *et al.* in 1998 [74] but, until now, not confirmed experimentally. The formation of the secondary vortex ring is the result of the interaction of the internally-reflected shock wave with the upstream deformed bubble surface. The presence of excess film mass at the bottom extremity of the bubble leads to the formation of a secondary vertical jet at the apex of the bubble and enhances the geometry of the secondary vortex ring. At late-times, the induced velocity due to the primary vortex ring leads to the entrainment of this secondary vortex ring, suggesting that the flow field at this time is mostly dominated by the primary vortex ring. Simulations without film material have shown that shock diffraction, combined with a reflected rarefaction, leads to the development of weak secondary jet and vortex ring, but this effect becomes more intense with the presence of a film layer. In both experiment and simulation, we observed the breaking of axial symmetry at late times. The experimental bubble has inherent asymmetries in its initial condition due to perturbations imposed by the bubble inflation and release processes; while the simulated bubble has grid-seeded perturbations. At late-times, these lead to the growth of azimuthal variations in the flow field, by a Widnall- type bending mode instability [71]. Vortex rings develop bends and kinks, and vortical fluctuations grow, leading to chaotic, turbulent motion in some regions of the flow.

6.1.3 Convergent shock-refraction geometry: high A

In convergent geometry at high A, we have observed that shock diffraction and focusing leads to very intense, highly localized pressure discontinuities, leading to the subsequent formation of high speed axial jets. A complex field of secondary shock waves is generated between the shocked bubble and the incident shock wave after shock focusing. The secondary shock waves propagating in the lateral and upstream directions transverses the already deforming bubble and enhances the complexity of the evolving vorticity field. Due to the combined intensity of the shock focusing effects and the azimuthal transport of vorticity, the vortex rings become highly distorted and nearly indistinguishable in the case of high-Mach number experiments. The shocked bubble is effectively reduced to a small core of compressed fluid, which trails behind a plume-like structure indicative of a well-developed mixing region. These results show a good agreement with calculations performed by Niederhaus *et al.* [48], showing the distinct effects that arise due to shock focusing in the case of an R12 bubble ($A = 0.613$) accelerated by a $M = 5.0$ shock wave. Results presented in Sec. 4.2.2, showed that the primary vortex ring existed at very late times in the case of low Atwood number flow even at high Mach number, and suggested that the increased Mach number is not itself sufficient to induce the development of this plume feature. The growth of this turbulent plume is mostly due to the nonlinear acoustic effects which are associated with the density contrast between the bubble and the ambient gas.

6.2 Bubble Dimension, Vortex Velocity, Circulation and Timescaling Arguments

For each of the scenarios considered here, the axial bubble dimension showed a linear growth rate after the initial shock-induced compression. The minimum axial dimension reached by the bubble is slightly higher compared to the theoretical value for $M > 2.0$ in the case of convergent as well as divergent geometry shock-bubble interactions. In general, for $M > 2.0$, the minimum axial dimension reached by the bubble is $1.3(W_i - u'_1)/W_i$. The lateral growth of the bubble at late-times asymptotes to a constant value in most of the experimental scenarios.

Dimensional analysis of trends in various quantities measured for these flow fields indicates that there is no single fundamental characteristic time or velocity scale that encompasses the different aspects of the flow evolution together for the wide range of Atwood number considered here. In the case of the divergent shock-refraction geometry, trends in the streamwise dimension of the shocked bubble are found to yield the closest approach to a self-similar trend (for $\tau < 20$) under a timescaling based on the incident shock wave speed W_i, while trends in the lateral dimensions and the primary vortex ring velocity follow timescales based on post-shock ambient flow speed u_1'. Mass transfer from the body of the bubble to the primary vortex ring was also observed in the lateral dimension plot for divergent-shock refraction geometry. The rate of this mass transfer increases significantly with the increase in the Mach number.

In the convergent geometry at low A, none of the timescales displayed a collapse of the bubble dimension data to a single trend for all M. This may be considered a shortcoming of the dimensionless timescales discussed in this dissertation, or a lack of self similarity behavior over the Mach number regime considered here. The rate of axial elongation significantly increases for $M > 2.03$, which is suggestive of a transitional Mach number. It is thought that at Mach numbers large enough that the flow speed of the shocked ambient gas becomes supersonic (for a shock wave in nitrogen at atmospheric temperature this occurs at $M = 2.07$), there are compressibility effects that may alter the growth of the bubble. Although the data suggest this is most likely be the case, it is still premature to make a definite conclusion.

In the convergent geometry for a fixed M, much stronger axial growth is observed for higher Atwood numbers although, at early-times, the minimum axial dimension reached by the bubble was roughly the same for all the scenarios. This difference can be attributed to the complex field of secondary shock waves generated due to shock focusing in the case of high Atwood number flows. Regions of intense mixing develop in the flow field which significantly increase the axial growth of the bubble. For a fixed M, a timescale based on $t' = D/(2W_i A^{0.95})$, yields a self-similar trend in the axial growth of the bubble by collapsing the growth trends for all the Atwood numbers considered in this study.

For all the experimental scenarios, the circulation-based velocity model of Picone and Boris provides a reliable prediction for the experimentally measured vortex velocity. The difference between the model and the experimentally measured values was less than 2% for $A < 0.2$, while for $A > 0.2$, the model overestimated the vortex velocity by roughly 5% or more. The Rudinger-Somers model, on the other hand, drastically overestimates the vortex ring velocity in the case of the divergent geometry shock-bubble interaction. It provided a very good agreement with experimental data for convergent geometry low A scenarios, while it underestimated the experimental value by roughly 10% for high A scenarios.

Quantitative analysis of circulation data demonstrates very good agreement with the predictions of the Yang-Kubota-Zukoski (YKZ) model for the late-time circulation in the case of divergent geometry shock-bubble interaction. It can also be noted, as observed in previous work [72], that the Picone-Boris model overestimated the circulation by a factor or two or more. This was very surprising, as the circulation-based velocity model of Picone-Boris provided a very reliable prediction for the experimentally measured velocity (the difference was less than 2%).

In the case of the convergent geometry, we note that as we increase the Atwood number the circulation associated with the vortex ring increases dramatically. For $M \approx 2.03$, the circulation increased seven times by increasing the value of A from 0.176 to 0.681. This difference can be attributed to the strong shock refraction in the case of higher Atwood number scenarios, which leads to a significant difference in the translational velocity of the bubble with respect to the post-shock flow speed. The Yang-Kubota-Zukoski (YKZ) model performs reliably well for $A < 0.2$, with better comparison with increasing Mach number. The Samtaney-Zabusky (SZ) model provides a reasonable estimates in general for $A > 0.2$, but it is unreliable for $A < 0.2$. The estimated value of the Reynolds number on the basis of the circulation, suggested a transition to turbulent behavior at late-times in all the experimental scenarios which is supported by the experimental images. Therefore, it can be concluded, on the basis of circulation and estimated Reynolds numbers, that the late-time flow field is turbulent for all the experimental scenarios.

6.3 Limitations and Future Work

Before generalizing the results obtained from these experiments, it is important to underline the limitations of this study. The major drawback of this study remains with the flow visualization technique utilized here. In this study, the images represents the Mie-scattered light resulting from the laser interaction with the atomized soap film particle. Surprisingly, this has resulted in excellent visualization of the flow field for all considered experimental scenarios, however we do not exactly know which gas is being tracked by the atomized particles. Therefore, it is difficult to comment on the mixing rate between the two gases, and this probably represents the biggest shortcoming of this work.

Although this visualization technique has provided excellent images of the flow field even for very high Mach numbers at late-times, efforts should be made to seed one of the gases with a tracer particles, which can provide brighter signals compared to the atomized soap particles. One should avoid using acetone or biacetyl for this experiment, as both of them get absorbed in the soap film. It is also documented that acetone is prone to molecular dissociation at high temperatures which limits its applicability in the present study. Probably, the best technique would be to create a filmless bubble (see Sec. 3.4.3), similar to the gas-jet cylinder experiments.

In the future, an interesting extension of this work would be to perform the same set of experiments, but replace the ambient gas by bubble gas and vice versa. Such effort will provide useful insight on the effect of the Atwood number on the bubble deformation pattern. The jetting effect, which has been addressed very briefly in this dissertation, can be studied in detail to obtain a relationship between the mass of the secondary inhomogeneity and the dimensions of the observed jet. Also, it will be of great interest to the astrophysics community to study the interaction of a detonation front with a shock-induced deforming spherical bubble. This can be achieved by utilizing the shock-focusing effect seen in the case of the convergent geometry shock-bubble interaction, to ignite a pre-mixed combustible mixture contained inside the bubble.

Appendix A

Stationary Bubble: Air Bubble in Argon, M=2.13

Results are presented from the interaction of a planar shock wave with an an axisymmetric soap bubble which is at rest on an injector. In this set of experiments (scenario 4), the driver gas is nitrogen, the driven gas is argon and a soap bubble bubble filled with air (test gas) sits on a stationary (non-retracting) injector inside the test section, facing upwards due to buoyancy as shown in Fig. 83(a); a $M = 2.13$ shock wave impacts the bubble from above. The air is seeded with smoke (at about 0.5% mass loading). The time is non-dimensionalized as $\tau = t/t'$. The characteristic time $t' = D/(2W_t)$, is defined as the cloud crushing time, where D is initial diameter of the bubble and W_t is the transmitted shock wave velocity in the bubble. The initial stages of the shock interaction result in the compression of the bubble as shown in Fig. 83 (a)-(c). There is no visible mixing with the surrounding argon at this stage, therefore, the density of the shocked bubble can be calculated using shock refraction physics. These images also show very close agreement with the images obtained without seeding the flow discussed in Chapter 4. Figure 84 shows two separate post-shock images acquired on the same CCD frame. From such experimental images, the transmitted shock wave speed is calculated as $W_t = X_s/\Delta t$, where Δt is time difference between those images. The initial bubble velocity is calculated as $V_b = X_b/\Delta t$. The above experiment has been modeled numerically [58], and the results are in quite good agreement. No detailed quantitative analysis was done for this case, as at later post-shock times, the injector used to support the bubble significantly altered the flow field.

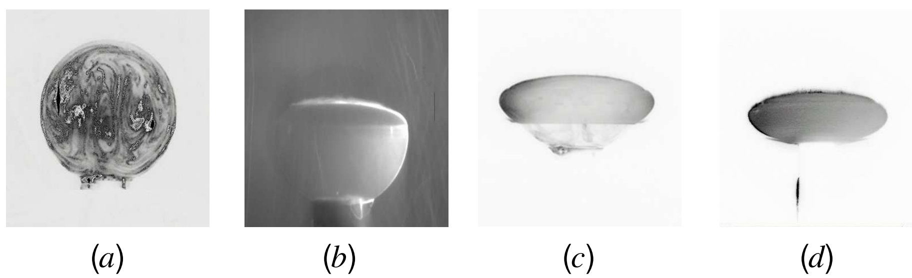

Figure 83: Experimental images for a $M = 2.13$ shock in Ar incident on a bubble of air seeded with smoke particles, times are given from when the shock is at the top of the bubble: (a) initial condition, just before the shock arrival, (b) $\tau = 0.73$, (c) $\tau = 1.57$, (d) $\tau = 2.0$.The time is non-dimensionalized as $\tau = t/\tau*$. The characteristic time $\tau* = D/(2W_t)$, is defined as the cloud crushing time, where D is initial diameter of the bubble and W_t is the transmitted shock wave velocity in the bubble.

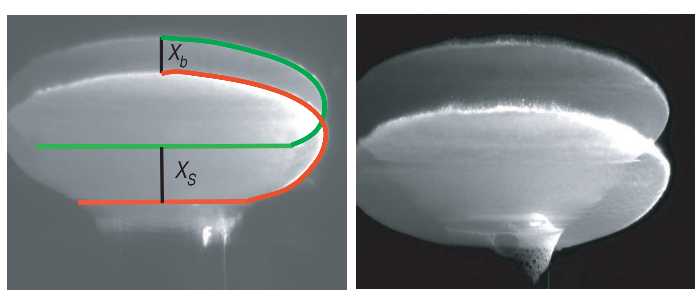

Figure 84: Experimental images for a $M = 2.13$ shock in Ar incident on bubble of air seeded with smoke particles. Two post shock images are shown on the same CCD array.

Appendix B

Uncertainties and Error Propagation

In Chapter 5 detailed analysis of quantitative measurements obtained from the experimental data included: a) translational velocities of the bubble and the associated vortex rings, b) circulation (deduced from the rings' velocity-defect), and c) different geometrical length scales (axial/lateral extents of the bubble and minor/major diameters of the vortex rings). The accuracy and precision of a measurement are always limited by the degree of refinement of the apparatus used, by the skill of the observer, and by the basic physics in the experiments. No measurement made is ever exact. In many cases, the quantity that we wish to determine is derived from several measured quantities. Therefore, it is necessary to estimate the uncertainty associated with the each measured quantity and systematically study the error propagation in the case of the derived quantities.

The general method of getting formulas for propagating errors involves the total differential of a function. Suppose that $F = f(x, y, z, ..)$ where the variables x, y, z, etc. are independent variables. The total differential is then given as

$$dF = \left(\frac{\partial f}{\partial x}\right) dx + \left(\frac{\partial f}{\partial y}\right) dy + \left(\frac{\partial f}{\partial z}\right) dz + ... \tag{B.1}$$

where $dx = \delta x$ is uncertainty in x, and likewise for the other differentials, dF, dy, dz, etc. The numerical values of the partial derivatives are evaluated by using the average values of the independent variables. The total error in F is then obtained using the method of standard deviation as:

$$\delta F = \sqrt{\left(\frac{\partial f}{\partial x}\right)^2 \delta x^2 + \left(\frac{\partial f}{\partial y}\right)^2 \delta y^2 + \left(\frac{\partial f}{\partial z}\right)^2 \delta z^2 + ...} \tag{B.2}$$

The translational velocity of the vortex ring was computed as $V_v = X/\Delta t$, where X is the displacement of the vortex measured over Δt. Therefore, using Eq. B.2, the error in velocity can be calculated as:

$$\frac{\delta V_v}{V_v} = \sqrt{\left(\frac{\delta X}{X}\right)^2 + \left(\frac{\delta \Delta t}{\Delta t}\right)^2}. \tag{B.3}$$

The second quantity of interest in the experiments were the various geometrical length scales of the bubble. In the experimental analysis, the length scales were non-dimensionalized by the initial bubble diameter for both heavy and light bubbles, *e.g.* $L_h = h/D$. The uncertainty in L_h, or any other geometrical length scale, can be calculated as:

$$\frac{\delta L_h}{L_h} = \sqrt{\left(\frac{\delta h}{h}\right)^2 + \left(\frac{\delta D}{D}\right)^2}. \tag{B.4}$$

Before we describe the uncertainty associated with circulation measurements, lets first calculated the uncertainty values for vortex velocity and the geometrical length scales of the bubble. To perform this analysis we will look at the experimental values for a $M = 2.07$ accelerated SF_6 bubble in N_2. In the experiments, the sampling frequency for the data acquisition system is 1 MHz, therefore the uncertainty associated with Δt is 1 μs. The values of various experimental parameters are:

$$X = 6.4 \text{ cm}, \; \delta\text{X} = 0.1 \text{ cm}, \; \Delta\text{t} = 220 \; \mu\text{s}, \; \delta\text{t} = 1 \; \mu\text{s}$$

$$h = 5.67 \text{ cm}, \; \delta\text{h} = 0.1 \text{ cm}, \; \text{D} = 3.28 \text{ cm}, \; \text{and } \delta\text{D} = 0.15 \text{ cm}.$$

Using these values, the uncertainty in vortex velocity and geometrical length scales are calculated to be 1.6 and 4.9% respectively. This uncertainty does not account for errors associated with gas purity or soap film contamination after break-up.

The circulation values in the experiments were deduced from the vortex velocity defect using the Kelvin's model shown below:

$$\Gamma^{\text{K}} = 2\pi D_v \left(V_v - u_1'\right) \left[\ln\left(\frac{8D_v}{d_v}\right) - \frac{1}{4}\right]^{-1}.$$

The following substitutions are made in the circulation equation to obtain a form which can be differentiated easily.

$$P_1 = D_v, \; P_2 = \left(V_v - u_1'\right), \; P_3 = d_v, \; \Gamma^{\text{K}}/2\pi = \Gamma.$$

Using this substitution and neglecting the constant term in the Kelvin's model, the equation is reduced to

$$\Gamma = P_1 P_2 \left[\ln \frac{P_1}{P_3}\right]^{-1}.$$

Now this equation can be differentiated easily to obtain the standard formulation of the uncertainty calculation.

$$\frac{\delta\Gamma}{\delta P_1} = P_2\left[\left(\ln\frac{P_1}{P_3}\right)^{-1} - \left(\ln\frac{P_1}{P_3}\right)^{-2}\right]$$
$$\frac{\delta\Gamma}{\delta P_2} = P_1\left[\ln\frac{P_1}{P_3}\right]^{-1}$$
$$\frac{\delta\Gamma}{\delta P_3} = \frac{P_1P_2}{P_3}\left[\ln\frac{P_1}{P_3}\right]^{-2}$$
$$\delta\Gamma = \sqrt{\left(\frac{\delta\Gamma}{\delta P_1}\delta P_1\right)^2 + \left(\frac{\delta\Gamma}{\delta P_2}\delta P_2\right)^2 + \left(\frac{\delta\Gamma}{\delta P_3}\delta P_1\right)^2}$$

With some more algebra we obtain the following form of circulation uncertainty

$$\frac{\delta\Gamma}{\Gamma} = \sqrt{\left[\left(\frac{\delta P_1}{P_1}\right)\left(1-\frac{1}{\ln\frac{P_1}{P_3}}\right)\right]^2 + \left[\left(\frac{\delta P_2}{P_2}\right)\right]^2 + \left[\left(\frac{\delta P_3}{P_3}\right)\frac{1}{\ln\frac{P_1}{P_3}}\right]^2}. \tag{B.5}$$

Now we can evaluate Eq. B.5 using the experimental parameters to calculate the uncertainty associated with the circulation measurements presented in this study. The experimental parameters are listed below:

$$\frac{\delta P_1}{P_1} = 0.049$$
$$\frac{\delta P_2}{P_2} = 0.019$$
$$\frac{\delta P_1}{P_1} = 0.049$$
$$\frac{P_1}{P_3} = 1.89$$

Using these values the uncertainty in circulation (Γ^{K}) is estimated to be 9.7%.

Bibliography

[1] J. D. Anderson, *Modern compressible flow with historical perspective*, 3rd ed., McGraw-Hill, New York, 2003.

[2] M. H. Anderson, B. P. Puranik, J. G. Oakley, P. W. Brooks, and R. Bonazza, *Shock tube investigation of hydrodynamic issues related to inertial confinement fusion*, Shock Waves **10** (2000), no. 5, 377.

[3] A. Bagabir and D. Drikakis, *Mach number effects on shock-bubble interaction*, Shock Waves **11** (2001), 209–218.

[4] G. J. Ball and R. A. East, *Shock and blast attenuation by aqueous foam barriers: influence of barrier geometry*, Shock Waves **9** (1999), 37–47.

[5] R. Bonazza and B. Sturtevant, *X-ray measurements of growth rates at a gas interface accelerated by shock waves*, Phys. Fluids **8** (1996), no. 9, 2496–2512.

[6] M. Brouillette, *The Richtmyer-Meshkov instablity*, Annu. Rev. Fluid Mech. **34** (2002), 445–468.

[7] M. Brouillette and B. Sturtevant, *Experiments on the Richtmyer-Meshkov instability:Small-scale perturbations on a plane interface*, Phys. Fluids **5** (1993), no. 4, 916–930.

[8] R. D. Cohen, *Shattering of a liquid drop due to impact*, Proc. R. Soc. Lond. A **435** (1991), 483–503.

[9] T. J. B. Collins, A. Poludnenko, A. Cunningham, and A. Frank, *Shock propagation in deuterium-tritium-saturated foam*, Phys. Plasmas **12** (2005), no. 062705.

[10] N. Cowperthwaite, *The interaction of a plane shock and a dense spherical inhomogeneity*, Physica D **37** (1989), 264–269.

[11] F. E. C. Culick, *Comments on a ruptured soap film*, J. Appl. Phys. **31** (1960), 1128.

[12] B. A. Davy and D. T. Blackstock, *Measurements of the refraction and diffraction of a short N wave by a gas-filled soap bubble*, J. Acoust. Soc. Am. **49** (1971), no. 3, 732–737.

[13] C. F. Delale, S. Nas, and G. Tryggvason, *Direct numerical simulations of shock propagation in bubbly liquids*, Phys. Fluids **17** (2005), no. 121705.

[14] M. Delius, F. Ueberle, and W. Eisenmenger, *Extracorporeal shock waves act by shock wave-gas bubble interaction*, Ultrasound in Med. and Biol. **24** (1998), no. 7, 1055–1059.

[15] P. E. Dimotakis, *The mixing transition in turbulent flows*, J. Fluid Mech. **409** (2000), 69–98.

[16] W. Eisenmenger, *The mechanisms of stone fragmentation in ESWL*, Ultrasound in Med. and Biol. **27** (2001), no. 5, 683–693.

[17] J. Giordano and Y. Burtschell, *Richtmyer-Meshkov instability induced by shock-bubble interaction: numerical and analytical studies with experimental validation*, Phys. Fluids **18** (2006), no. 036102.

[18] S. Gordon and B. J. McBride, *Computer program for computation of complex chemical equilibrium compositions, rocket performance, incident and reflected shocks, and Chapman-Jouguet detonations*, Spec. Publ. SP-273, Lewis Research Center, NASA, 1976.

[19] S. M. Gracewski, G. Dahake, Z. Ding, S. J. Burns, and E. C.Bach, *Internal stress wave measurements in solid subjected to lithotripter pulses*, J. Acoust. Soc. Am. **94** (1993), 652–661.

[20] J. A. Greenough and J. W. Jacobs, *A numerical study of shock-accelearation of a diffuse helium cylinder*, Proceedings of the Fifth International Workshop on Compressible Turbulent Mixing, World Scientific, 1996, pp. 338–345.

[21] J.-F. Haas and B. Sturtevant, *Interaction of weak shock waves with cylindrical and spherical inhomogeneities*, J. Fluid Mech. **181** (1987), 41–76.

[22] J. F. Hansen, H. F. Robey, R. I. Klein, and A. R. Miles, *Experiment on the mass-stripping of an interstellar cloud in a high Mach number post-shock flow*, Phys. Plasmas **14** (2007), no. 056505.

[23] L. F. Henderson, *On the refraction of shock waves*, J. Fluid Mech. **198** (1989), 365–386.

[24] L. F. Henderson, P. Colella, and E. G. Puckett, *On the refraction of shock waves at a slow-fast gas interface*, J. Fluid Mech. **224** (1991), 1–27.

[25] U. Hwang, K. A. Flanagan, and R. Petre, *CHANDRA X-ray observation of a mature cloud-shock interaction in the bright eastern knot region of Puppis A*, Ap. J. **635** (2005), 355–364.

[26] C. Isenberg, *The science of Soap films and Soap bubbles.*, Tieto Ltd., Avon, England, 1978.

[27] J. W. Jacobs, *Shock-induced mixing of a light-gas cylinder*, J. Fluid Mech. **234** (1992), 629–649.

[28] ______, *The dynamics of shock accelerated light and heavy gas cylinders*, Phys. Fluids A **5** (1993), 2239–2247.

[29] M.A. Jones and J.W. Jacobs, *A membraneless experiment for the study of Richtmyer-Meshkov instability of a shock-accelerated gas interface*, Phys. Fluids **9** (1997), no. 10.

[30] R. I. Klein, K. S. Budil, T. S. Perry, and D. R. Bach, *Interaction of supernova remnants with interstellar clouds: from the NOVA laser to the galaxy*, Ap. J. S. **127** (2000), 379–383.

[31] ______, *The interaction of supernova remnants with interstellar clouds: experiments on the NOVA laser*, Ap. J. **583** (2003), 245–259.

[32] R. I. Klein, C. F. McKee, and P. Colella, *On the hydrodynamic interaction of shock waves with interstellar clouds. I. Nonradiative shocks in small clouds*, Ap. J. **420** (1994), 213–236.

[33] S. Kumar, G. Orlicz, C. Tomkins, C. Goodenough, K. Prestridge, P. Vorobieff, and R. Benjamin, *Stretching of material lines in shock-accelerated gaseous flows*, Phys. Fluids **17** (2005), no. 082107.

[34] H. Lamb, *Hydrodynamics*, Dover, New York, 1945.

[35] G. Layes, G. Jourdan, and L. Houas, *Distortion of a spherical gaseous interface accelerated by a plane shock wave*, Phys. Rev. Lett. **91** (2003), no. 17.

[36] ———, *Experimental investigation of the shock wave interaction with a spherical gas inhomogeneity*, Phys. Fluids **17** (2005), no. 028103.

[37] G. Layes and O. LeMétayer, *Quantitative numerical and experimental studies of the shock accelerated heterogeneous bubbles motion*, Phys. Fluids **19** (2007), no. 042105.

[38] K. Levy, O. Sadot, A. Rikanati, D. Kartoon, Y. Srebro, A. Yosef-Hai, G. Ben-Dor, and D. Shvarts, *Scaling in the shock-bubble interaction*, Laser and Particle Beams **21** (2003), 335–339.

[39] J. Lindl, *Development of the indirect-drive approach to inertial confinement fusion and the target physics basis for ignition and gain*, Phys. Plasmas **2** (1995), no. 11, 3933–4024.

[40] F. E. Marble, E. E. Zukoski, J. Jacobs, G. Hendricks, and I. Waitz, *Shock enhancement and control of hypersonic mixing and combustion*, 26th AIAA, SAE, ASME, and ASEE Joint Propulsion Conference, Orlando, FL, July 16-18, 1990.

[41] G. H. Markstein, *Flow disturbances induced near a slightly wavy contact surface, or flame front, traversed by a shock wave*, J. Aero. Sci. **24** (1957), 238–239.

[42] ———, *A shock tube study of the flame front-pressure wave interaction*, 6th Symposium (International) on Combustion, New York: Reinhold, 1957, pp. 387–398.

[43] A. Marquina and P. Mulet, *A flux-split algorithm applied to conservative models for multicomponent compressible flows*, J. Comput. Phys. **185** (2003), 120–138.

[44] Ye. Ye. Meshkov, *Instability of a shock wave accelerated interface between two gases*, NASA Technical Translation **NASA TT F-13,074** (1970).

[45] B. Motl, J. Niederhaus, J. G. Oakley, D. Ranjan, M. H. Anderson, R. Bonazza, and J. Greenough, *Shock accelerated two-dimensional interface*, Proceedings of the Tenth International Workshop on Compressible Turbulent Mixing, 2006.

[46] K. J. Mysels, K. Shinoda, and S. Frankel, *Soap films: Studies of their thinning and a Bibliography*, Pergamaon Press, New York, 1959.

[47] J. H. J. Niederhaus, *A computational parameter study for three-dimensional shock-bubble interactions*, Ph.D. thesis, University of Wisconsin-Madison, 2007.

[48] J. H. J. Niederhaus, J. A. Greenough, J. G. Oakley, D. Ranjan, M. H. Anderson, and R. Bonazza, *A computational parameter study for the three-dimensional shock-bubble interaction*, J. Fluid Mech. **594** (2008), 85–124.

[49] J. G. Oakley, *Experimental study of shocked gas interfaces with visualized initial conditions*, Ph.D. thesis, University of Wisconsin-Madison, 2001.

[50] A. B. Pandit and J. F. Davidson, *Hydrodynamics of the rupture of thin liquid films*, J. Fluid Mech. **212** (1990), 11–24.

[51] J. M. Picone and J. P. Boris, *Vorticity generation by shock propagation through bubbles in a gas*, J. Fluid Mech. **189** (1988), 23–51.

[52] J. M. Picone, E. S. Oran, J. P. Boris, and T. R. Young Jr., *Theory of voriticty generation by shock wave and flame interactions*, Dynamics of Shock Waves, Explosions, and Detonations (J. R. Bowen, N. Manson, A. K. Oppenheim, and R. I.

Soloukhin, eds.), Progress in Astronautics and Aeronautics, vol. 94, AIAA, New York, NY, 1984, pp. 429–448.

[53] K. Prestridge, P. Vorobieff, P. M. Rightley, and R. F. Benjamin, *Validation of an instability growth model using particle image velocimetry measurements*, Phys. Rev. Lett. **84** (2001), no. 19, 4353–4356.

[54] P. B. Puranik, J. G. Oakley, M. H. Anderson, and R. Bonazza, *Experimental study of the Richtmyer-Meshkov instability induced by a Mach 3 shock wave*, Shock Waves **13** (2004), no. 6, 413.

[55] J. J. Quirk and S. Karni, *On the dynamics of a shock-bubble interaction*, J. Fluid Mech. **318** (1996), 129–163.

[56] D. Ranjan, M. H. Anderson, J. G. Oakley, and R. Bonazza, *Experimental investigation of a strongly shocked gas bubble*, Phys. Rev. Lett. **94** (2005), no. 184507.

[57] D. Ranjan, J. Niederhaus, B. Motl, M. Anderson, J. Oakley, and R. Bonazza, *Experimental investigation of primary and secondary features in high-Mach-number shock-bubble interaction*, Phys. Rev. Lett. **98** (2007), no. 024502.

[58] D. Ranjan, J. Niederhaus, J. Oakley, M. H. Anderson, J. Greenough, and R. Bonazza, *Measurements of mixing induced at a gas interface by the richtmyer-meshkov instability*, Proceedings of the twenty-fourth International Symposium on Shock Waves, Shock Waves, 2004.

[59] R. D. Richtmyer, *Taylor instability in shock accleration of compressible fluids*, Commun. Pure Appl. Math. **13** (1960), 297–319.

[60] H. F. Robey, T. S. Perry, R. I. Klein, J. O. Kane, J. A. Greenough, and T. R. Boehly, *Experimental investigation of the three-dimensional interaction of a strong shock with a spherical density inhomogeneity*, Phys. Rev. Lett. **89** (2002), no. 8.

[61] G. Rudinger, *Shock wave and flame interactions*, Combustion and Propulsion, Third AGARD Coll., London: Pergamon, 1958, pp. 153–182.

[62] G. Rudinger and L. M. Somers, *Behavior of small regions of different gases carried in accelerated gas flows*, J. Fluid Mech. **7** (1960), 161–176.

[63] P. G. Saffman, *Vortex dynamics*, Cambridge University Press, Cambridge, 1991.

[64] R. Samtaney and N. J. Zabusky, *Circulation deposition on shock-accelerated planar and curved density-stratified interfaces: models and scaling laws*, J. Fluid Mech. **269** (1994), 45–78.

[65] J. W. Strutt, *Scientific Papers*, Cambridge Uuniversity Press, Cambridge.

[66] G. I. Taylor, *The instability of liquid surfaces when accelerated in a direction perpendicular to their planes*, I. Proc. R. Soc. **A** (1950), no. 201.

[67] ———, *Formation of a vortex ring by giving an impulse to a circular disk and then dissolving it away*, J. Appl. Phys. **24** (1953), no. 1.

[68] ———, *The dynamics of thin sheets of fluid III. Disintegration of fluid sheets*, Proc. R. Soc. Lond. A **253** (1959), 313–321.

[69] P. A. Thompson, *Compressible-Fluid Dynamics*, McGraw-Hill, New York, NY, 1984.

[70] C. Tomkins, K. Prestridge, P. Rightley, M. Marr-Lyon, P. Vorobieff, and R. Benjamin, *A quantitative study of the interaction of two Richtmyer-Meshkov-unstable gas cylinders*, Phys. Fluids **15** (2003), no. 4, 986.

[71] S. E. Widnall, D. B. Bliss, and C. Y. Tsai, *The instability of short waves on a vortex ring*, J. Fluid Mech. **66** (1974), 35.

[72] J. Yang, T. Kubota, and E. E. Zukoski, *A model for characterization of a vortex pair formed by shock passage over a light-gas inhomogeneity*, J. Fluid Mech. **258** (1994), 217–244.

[73] N. J. Zabusky, *Vortex paradigm for accelerated inhomogeneous flows: visiometrics for the Rayleigh-Taylor and Richtmyer-Meshkov environments*, Ann. Rev. Fluid Mech. **31** (1999), 495–56.

[74] N. J. Zabusky and S. M. Zeng, *Shock cavity implosion morphologies and vortical projectile generation in axisymmetric shock- spherical fast/slow bubble interactions*, J. Fluid Mech. **362** (1998), 327–346.

[75] C. Zoldi, *A numerical and experimental study of a shock-accelerated heavy gas cylinder*, Ph.D. thesis, State University of New York at Stony Brook, 2002.